TITLE

B cell and antibody targeting of transplant alloantigen epitopes is supported by both self and allo-recognition

AUTHORS

John T. Killian, Jr.,[1,†] R. Glenn King,[2,†] James L. Kizziah,[2] Christopher F. Fucile,[3] Ruben Diaz-Avalos,[4] Shihong Qiu,[2] Aaron Silva-Sanchez,[5] Betty J. Mousseau,[2] Kevin J. Macon,[2] Amanda R. Callahan,[2] Guang Yang,[2] M. Emon Hossain,[5] Jobaida Akther,[5] Daryl B. Good,[6] Susan Kelso,[6] Julie A. Houp,[1] Frida Rosenblum,[7] Paige M. Porrett,[1] Song C. Ong,[8] Vineeta Kumar,[8] Erica Ollmann Saphire,[4] John F. Kearney,[2] Troy D. Randall,[5] Alexander F. Rosenberg,[2,3] Todd J. Green,[2,#] Frances E. Lund[2,9,#,*]

AUTHOR AFFILIATIONS

[1]Department of Surgery, University of Alabama at Birmingham Heersink School of Medicine, Birmingham, AL 35294, USA

[2]Department of Microbiology, University of Alabama at Birmingham Heersink School of Medicine, Birmingham, AL 35294, USA

[3]Informatics Institute, The University of Alabama at Birmingham, Birmingham, AL 35294, USA

[4]Center for Infectious Disease and Vaccine Discovery, La Jolla Institute for Immunology, La Jolla, CA 92037, USA

[5]Department of Medicine, Division of Clinical Immunology and Rheumatology, University of Alabama at Birmingham Heersink School of Medicine, Birmingham, AL 35294, USA

[6]Nicoya, Kitchener-Waterloo, Ontario, Canada

[7]Department of Pathology, University of Alabama at Birmingham Heersink School of Medicine, Birmingham, AL 35294, USA

[8]Department of Medicine, Division of Nephrology, University of Alabama at Birmingham Heersink School of Medicine, Birmingham, AL 35294, USA

[9]Lead contact

*Correspondence: flund@uab.edu (F.E.L.)

[†]These authors contributed equally

[#]Co-corresponding authors

KEYWORDS

B lymphocytes; Antibodies; Alloimmunity; Transplantation; Self-recognition; Tolerance; Epitopes

ABSTRACT

Donor-specific antibody (DSA) responses against human leukocyte antigen (HLA) proteins mismatched between kidney transplant donors and recipients cause allograft loss. Using single-cell, molecular, structural, and proteomic techniques, we profiled the HLA-specific (alloreactive) B cell response in kidney and blood of a transplant recipient with antibody-mediated rejection (AMR). We identified 14 distinct alloreactive B cell lineages, which spanned the rejected organ and blood and expressed high-affinity anti-donor HLA-specific B cell receptors – many of which were clonally linked to circulating DSA. The alloreactive B cell response was focused on exposed, solvent-accessible mismatched HLA residues, while also demonstrating extensive contacts with self-HLA residues. Consistent with structural evidence of self-recognition, measurable self-reactivity by donor-specific B cells was common and positively correlated with anti-donor affinity maturation. Thus, allo- and self-reactive signatures appeared to converge, suggesting that during AMR, the recognition of non-self and breaches of tolerance conspire to produce a pathogenic donor-specific adaptive response.

INTRODUCTION

Antibodies (Abs) against mismatched human leukocyte antigens (HLA) are a leading cause of injury and graft loss in kidney transplantation.[1-3] Up to 25% of kidney transplant recipients will develop a new donor-specific anti-HLA antibody (HLA-Ab) following transplant,[4] and these patients suffer a 40% absolute decline in 10-year graft survival.[5] Ultimately, graft loss and the re-initiation of dialysis is associated with significant increases in mortality for these patients.[6] In addition to antibody-secreting cells (ASCs), which produce injurious donor-specific Abs (DSA), the presence of donor HLA-specific (alloreactive) circulating memory B cells (Bmems) also correlates with poor outcomes.[7-9] Thus, both arms of the humoral immune response appear to work in concert to drive rejection.[10] Unfortunately, current therapies aimed at managing antibody-mediated rejection (AMR) and depleting ASCs and Bmems are largely ineffective in transplant rejection, indicating the unmet need to both prevent and treat these alloresponses.[11]

To produce high-affinity Abs against a target antigen, the B cell response relies on the competitive environment of the germinal center (GC) within secondary lymphoid tissues where the processes of somatic hypermutation (SHM) and clonal selection result in the development of expanded, affinity-matured lineages of long-lived ASCs and Bmems.[12] Studies of infection and vaccination show that the quality of lymphoid tissue GC-driven responses is regulated by the assistance of other immune cells,[13] particularly T follicular helper cells (T_{FH} cells), and antigen.[13] B cell responses to antigen are influenced by the mode of antigen exposure, the persistence of antigen and the physical characteristics of the antigen.[14] Individual B cells respond to protein antigens by recognizing exposed epitopes.[15] In many cases, B cells can target multiple distinct epitopes within a single antigen, resulting in a diverse polyclonal repertoire of Bmems and ASCs – all of which are specific for the same antigen.[16] For other antigens, the B cell response may be more tightly focused on a limited number of immunogenic epitopes at the expense of other epitopic sites. This focused “immunodominant” B cell response, which is often seen in the setting of anti-viral immunity, is regulated by precursor frequency, prior antigen history (memory), affinity, antigen topography, antigen kinetics, and T cell help.[17,18] In addition, single polymorphic residues may contribute to immune focusing and immunodominance across B cell and ASC compartments.[19,20]

Although HLA residues that are mismatched between donor and recipient are necessary to generate alloimmunity[21] and clearly lead to the production of HLA-Abs, AMR, and graft loss,[22] the relative immunogenicity of individual polymorphic residues and the rules governing immune responses to HLA antigens remain largely unknown.[23-25] This lack of knowledge is compounded by the fact that alloreactive B cell responses are difficult to sample[26] as organ-infiltrating alloreactive B cells[27] and tertiary lymphoid structures can develop in transplanted organs.[28,29] Moreover, alloreactive B cell responses are focused on an antigen, HLA, that is persistent, abundant, and quite similar at a structural and molecular level to self-HLA. Indeed, even the most highly mismatched HLA proteins are still >87% identical at the amino acid (AA) level.[30] Thus, in many ways, the B cell response to HLA antigens may be most analogous to an altered-self response, similar to those seen in cancer[31] and autoimmune

disease.[32] Interestingly, breaches in self-tolerance may not be uncommon in transplant recipients as multiple studies report that these individuals can develop autoAbs specific for monomorphic (i.e., non-HLA) autoantigens.[33-35] However, unlike a typical monomorphic autoantigen response, the anti-HLA alloresponse demands that the immune system not only recognize altered-self HLA but must also enforce tolerance against both self-alleles at a given HLA locus. One widely used model for interpreting studies of HLA-Ab responses and understanding what mismatches constitute “self” vs. “non-self,” posits that small (3.5 Å-radius) patches of mismatched polymorphic residues within the larger HLA epitope, so called *eplets*, are the critical determinants of the anti-HLA B cell response.[36] However, there are no structural data to support this model. In fact, the only reported HLA-Ab/HLA complex structure[37] features an Ab that was isolated using phage display, rather than an Ab that was generated during an ongoing alloimmune response.

Given this knowledge gap, the United States Kidney Allocation system currently prioritizes only perfect whole-antigen matches between donor and recipient,[38] an approach which converts the matching problem into an “all-or-nothing” proposition. However, given the evidence showing that increasing numbers of AA mismatches between donor and self HLA correspond with poor transplant outcomes,[22,39-41] there is considerable interest in matching donors and recipients at the residue level.[23,42-45] In order to take this approach, it is important to first understand the rules governing allorecognition by B cells. In this manuscript, we used single cell, molecular, structural, and proteomic techniques to assess the alloimmune response in a kidney transplant recipient with clinical features of anti-HLA DSA, AMR, and graft loss. We showed that the alloreactive B cells undergo clonal selection and affinity maturation during organ rejection. This high affinity alloreactive B cell response not only spanned B cells and ASCs in the rejected allograft and the peripheral blood, but also included lineages of Bmems and ASCs that were clonally linked to circulating DSA in the patient. Profiling the B cell response against a mismatched donor HLA protein at the single cell level revealed multiple alloreactive HLA-specific B cell lineages but also clearly showed epitopic focusing and immunodominance of the B cell immune response. We solved the structure of three Ab/HLA complexes and revealed the structural basis of these immunodominant HLA epitopes. While mismatched residues between donor-HLA and self-HLA appeared critical for the fine specificity of the B cells, we also identified extensive interactions between the alloreactive Abs and self-HLA residues. Moreover, we observed measurable self-HLA reactivity by many donor-specific B cells and found that self-reactivity was strongly associated with the acquisition of high-affinity donor-specific responses. Thus, breaches of tolerance appeared to play an important role in licensing the donor-specific response, suggesting that the rules governing alloreactive B cell responses and altered self-responses are likely to be similar.

RESULTS

B cells and ASCs from kidney and blood show features of antigen-driven selection.

ASCs that produce DSA directed against HLA molecules that are mismatched between the transplanted donor organ and the recipient are clearly important drivers of chronic organ rejection,[1-3] yet we know remarkably little about the structural epitopes in the mismatched HLA molecules that are specifically targeted by the humoral immune response.[25,37] Likewise, the relationship between the alloreactive B cells, which recirculate or are resident in the transplanted organ, and the donor HLA-specific ASCs is not well-characterized.[27] To test the contribution of alloreactive B cells to allograft rejection, we examined the donor HLA-specific B cell response in a kidney transplant recipient who presented with high levels of circulating DSA directed against the mismatched HLA allele and histopathologic allograft injury consistent with AMR.

To assess whether the allograft exhibited microanatomic structures and phenotypic features that would support local adaptive immune responses, we performed immunohistologic analysis on tissue sections from the allograft. It is known that B cells can accumulate in the graft during kidney transplant rejection and that intragraft B cells can be localized with T follicular helper (T_{FH}) cells in germinal center (GC)-like structures[28] or can be found independently of T_{FH} cells.[29] Although we identified clusters of T and B cells (Figure 1A), proliferating B cells (Figure 1B), and ASCs (Figure 1C) within the allograft, we did not observe tertiary lymphoid structures (TLS) containing T and B cell clusters with follicular dendritic cell (FDC) networks.[28] To confirm these histologic findings, we performed flow cytometric analysis on the kidney-infiltrating immune cells and identified $IgD^{neg}CD27^{+}$ memory B cells (Bmem), $IgD^{neg}CD27^{neg}$ (double negative, DN) B cells, and $CD27^{hi}CD38^{hi}$ ASCs (Figure 1D). A large fraction of the intragraft B cells expressed CD71 (Figure 1E), suggesting that the cells were activated in response to antigen.[46] Thus, the allograft contained ASCs and antigen-experienced B cells that displayed features of activated, proliferating cells.

Whether in secondary[47] or tertiary lymphoid structures[48], B cells can undergo antigen-driven clonal expansion and diversification of their immunoglobulin (Ig) gene encoded B cell receptors (BCRs) through T cell-dependent somatic hypermutation (SHM). These processes ultimately culminate in selection of high affinity B cell clones.[29] To evaluate whether the B cells found in the allograft and peripheral blood showed immunogenetic evidence of antigen-driven expansion or selection, we sort-purified bulk populations of ASCs and antigen-experienced B cell subsets from the rejected kidney and blood (Figure S1A-B) and sequenced the BCR Ig heavy (IgH) chain variable domain (IgV_H) of these cells. We next assigned the IgV_H sequences to clonal lineages, which we defined as sharing *IGHV* and *IGHJ* gene segments, having identical IgH chain complementarity determining region 3 (HCDR3) lengths, and exhibiting >85% nucleotide identity across the HCDR3.[49] Then, we analyzed clonal relationships between the B cells and ASCs found in circulation and the allograft. We observed clonal expansion within the allograft, with rich connections between the $CD27^{+}CD38^{+}$ ASC, $CD27^{+}CD38^{neg}$ Bmem, and $IgD^{neg}CD27^{neg}$ DN B cell subsets (Figure 1F). We found numerous shared lineages between the B cells in the

graft and in the blood (Figure 1G). In contrast to lower clonal sharing between blood and tissues isolated from a control non-transplant recipient (Figure S1C), the BCR repertoire in both the rejected kidney and peripheral blood of the transplant patient was highly shared (Figure 1G, Figure S1C). Since we observed substantial sharing of expanded B cell lineages in the blood and kidney, we asked whether the largest clones in kidney were also found in blood. We observed that the vast majority, and all expanded lineages that constituted at least 1% of the IgV_H sequences in the kidney, were also found in circulation (Figure 1H). Thus, the B cells in kidney and blood of the transplant patient were expanded, clonally restricted and shared.

To determine whether these expanded and shared clones exhibited properties of ongoing antigenic selection, we assessed the isotype and SHM profile of the BCRs expressed by the kidney and blood B cells. Not surprisingly, most B cells in both sites were class-switched, primarily to the IgG isotype (Figure S1D). Moreover, and consistent with an active immune response, the B cells from both sites had undergone extensive SHM (Figure S1E). The B cells and ASCs across kidney and blood possessed similar median numbers of V-region nucleotide mutations (Figure S1E) and the intragraft DN B cells had similar numbers of mutations to intragraft Bmems and ASCs (25 vs. 27 and 28 median mutations, respectively) (Figure S1E). Thus, the B cells in the rejected kidney and blood of a transplant patient with AMR and graft loss were isotype-switched, clonally expanded, shared and mutated – all consistent with an ongoing robust adaptive immune response that spanned both the rejected kidney and blood.

Class-switched and somatically mutated HLA-A alloreactive B cells accumulate in the rejected graft and peripheral blood.

Clonally expanded B cells in kidney allografts[50] and intragraft B cell infiltrates[51,52] correlate with poor transplant outcomes. However, the selecting antigens and mechanisms by which the intragraft B cells contribute to these poor outcomes remain largely undefined. We hypothesized that a portion of allograft-infiltrating and circulating B cells would be specific for the mismatched donor HLA alleles and would display evidence of affinity maturation and clonal expansion. To test this hypothesis, we analyzed B cells specific for the mismatched donor HLA allele, HLA A*01:01, as anti-A*01:01 DSA was easily detected in the patient's blood using standard clinical lab assays (Figure 1I). We used fluorochrome-labeled tetramers of recombinant HLA A*01:01 to sort-purify single HLA-reactive B cells from the allograft and the peripheral blood (Figure 1J, Figure S2A). From these single A*01:01-specific B cells, we cloned and sequenced the BCR IgH and Ig light (IgL) chain genes and then expressed these genes as recombinant human IgG1 monoclonal Abs (rmAbs). We confirmed the specificity of the rmAbs by assessing binding to A*01:01-coated microbeads (Figure 1K). Of the 50 A*01:01-specific rmAbs, 47 were derived from peripheral blood, and 3 were from the allograft. The majority were cloned from Bmems (43/50, 86.0%), with the remainder coming from DN B cells (7/50, 14.0%). The A*01:01-specific B cells had an antigen-experienced phenotype ($IgD^{neg}CD71^{+}$) and some expressed CD11c (Figure S2B), similar to Bmems that are associated with AMR and are poised to differentiate into donor-specific Ab-producing ASCs.[27]

We then immunogenetically mapped the A*01:01-specific rmAbs to lineages in the bulk kidney and blood IgV_H-Seq dataset. If an A*01:01-specific rmAb and a lineage found in the bulk IgV_H-Seq dataset shared *IGHV* and *IGHJ* gene segments, identical HCDR3 lengths, and >85% nucleotide identity across the HCDR3, we assigned the rmAb and any clonally related rmAbs to this lineage and classified the lineage as A*01:01-specific. Using this approach, we assigned the rmAbs and the clonally related IgV_H sequences (n=4142), which were derived from both blood and kidney B cells and ASCs, to 14 distinct A*01:01-specific lineages. Comparison of the mutation frequencies between the A*01:01-specific lineages (Figure 1L) and the total IgV_H-Seq dataset (Figure S1E) indicated that the median V-region mutations were similar (within 2 nucleotides) for most cell subsets. However, we noted that the kidney ASCs and blood Bmems in the A*01:01-specific lineages had (Figure 1L), on average, fewer mutations compared to the bulk kidney ASCs and blood Bmem (Figure S1E). We also found an increased median number of mutations (35 vs. 25) in the A*01:01-specific kidney DN cells (Figure 1L) compared to the total IgV_H-Seq repertoire (Figure S1E). This finding could be attributed to two expanded A*01:01-specific lineages (Lin2 and Lin12), which included large numbers of highly mutated kidney DN cells (Figure S2C-D). Finally, while the total blood IgV_H-Seq repertoire included many IgA sequences (Figure S1D, up to 45% of sequences per subset), this was not seen in the A*01:01-specific lineages, which showed almost exclusive IgG utilization across all subsets in both blood and kidney (Figure 1M). Thus, the blood and rejected kidney contained multiple lineages of IgG-switched and highly somatically mutated B cells specific for the donor A*01:01 protein.

Affinity-matured alloreactive B cells span the kidney and blood.

As expanded clonal lineages of B cells reflect the immunogenetic record of SHM and antigen selection,[53,54] we used the SHM profile of the A*01:01-specific B cells to better understand the evolution of the alloresponse to donor HLA. We identified many examples of lineages that contained multiple B cell subsets (Figure 2A-C), which spanned the kidney and blood and exhibited increasing numbers of mutations within the clonal lineage tree (Figure 2A-B). Eight of these lineages represented at least 2.5% of the entire A*01:01-specific IgV_H-Seq repertoire (Figure 2D), and at least two types of B cells were found in 10/14 lineages (Figure 2E), with the most represented subsets including kidney ASC (11/14 lineages) and kidney Bmem (8/14 lineages, Figure 2E). We next used localized surface plasmon resonance (L-SPR) to evaluate affinity maturation at the single BCR level by determining the binding properties of the different rmAbs against A*01:01 (Figure 2). Consistent with our hypothesis that the A*01:01-specific B cell response had undergone affinity maturation, the median K_D of binding by the 50 rmAbs to A*01:01 was 2.1 nM (Figure 2G). To confirm that this response was due to the accumulation of mutations and was not germline-encoded, we synthesized rmAbs encoding the inferred unmutated common ancestors (UCAs) of A*01:01-reactive lineages and assayed anti-A*01:01 binding using cytometric bead array and L-SPR. As shown in Figure 2H, the K_Ds of two mutated rmAbs derived from Lin4 and Lin12 were between 100-1000 fold lower (i.e. higher affinity) than the K_Ds derived from the inferred UCAs for those two lineages. Similarly, we observed significant increases in anti-A*01:01 affinity for all the rmAbs (n=36) found in these 9 different lineages when compared to the UCA for each of these lineages (Figure 2I, $p<0.0001$). When we compared the K_D of a lineage UCA to the K_D of the highest affinity rmAb in that lineage, we observed a median

2174-fold increase in affinity (Figure 2J). Moreover, the UCA from 5/9 lineages showed no detectable binding to A*01:01 by L-SPR (Figure 2J). Collectively, these data supported the idea that the A*01:01-specific lineages had undergone affinity maturation against mismatched donor HLA.

Donor-specific ASCs link the cellular and serologic alloreactive repertoires.

Circulating DSA are believed to be the most critical effectors of B cell-related allograft pathology.[2,4] While our data showed extensive clonal relatedness between the alloreactive B cell and ASC compartments in kidney and blood, prior vaccination and infection studies indicate that the serologic (secreted Ab) and B cell repertoires can differ.[55,56] To assess this relationship in the setting of alloimmunity, we compared the proteome of the secreted circulating A*01:01-specific polyclonal Ab to the repertoire of the kidney and blood A*01:01-specific B cells. We affinity-purified the circulating polyclonal plasma Abs (appAbs) derived from the kidney transplant recipient on a recombinant HLA A*01:01 column. Following enzymatic digestion, the peptides derived from the A*01:01-specific appAbs were analyzed using liquid chromatography tandem mass spectrometry (LC-MS/MS) and then aligned to AA sequences generated from the A*01:01-specific IgV_H-Seq and A*01:01-specific rmAb datasets. From this analysis, we identified overlapping A*01:01-specific appAb peptides that matched the sequences of the A*01:01-specific B cells and ASCs found in kidney and blood. Importantly, this overlap included matched identical sequences across the hypervariable HCDR3s of the appAbs. For example, IgV_H AA sequences that were identical to rmAbs (D01 and G22) found in Lin4, which spanned both the kidney and blood and was dominated by ASCs (Figure 3A), were recovered from the A*01:01-specific appAbs (Figure 3B-C). This finding was not limited to Lin4 as we identified many circulating appAb peptide sequences that could be mapped to A*01:01-specific B cells (Figure 3D-E), which were derived from 4 different A*01:01-specific lineages (Figure 3F). Consistent with this result, the A*01:01-specific lineages that contained the most ASC sequences within the IgV_H-Seq dataset (Figure 3F, Lin4, Lin14, Lin3) were all detected within the circulating appAb compartment. Thus, the circulating DSA appeared to be clonally related to the ongoing donor-specific B cell response that spanned kidney and blood in the patient.

Immune focusing and dominant reactivity patterns within the alloreactive repertoire.

Although mismatched HLA residues are necessary to generate alloimmunity,[21] the relative contributions and immunogenicity of these polymorphic residues remain unknown.[23-25] As polymorphic residues in antigens may contribute to immune focusing and immunodominance across B cell and ASC compartments,[19,20] we used the anti-A*01:01, donor-specific rmAb response of the transplant recipient to assess whether specific polymorphic residues could drive immune-focusing of the alloimmune response. We first clustered the 50 A*01:01-specific rmAbs based upon patterns of reactivity against a panel of 21 HLA-A locus proteins (Figure 4A, Figure S3A). For these reactivity patterns, we defined positive reactivity to an HLA protein if the rmAb bound to HLA-coated beads at a net geometric mean fluorescence intensity (net gMFI) of at least 40,000 (see *Methods* for additional detail). As expected, the majority of the HLA Class I proteins were not recognized by the 50 rmAbs (Figure 4A, Figure S3B), however we observed that the rmAbs displayed multiple distinct HLA-A reactivity patterns (Figure

4A, Figure S3B). When we compared the reactivity profiles of the 50 rmAbs to the reactivity profile of the circulating A*01:01-specific affinity-purified appAbs, we found that the reactivity patterns were strikingly similar – with the rmAbs and the appAbs showing the highest reactivity towards A*01:01, A*36:01 and A*80:01 (Figure 4B). This result indicated that the HLA reactivity of the collection of 50 rmAbs was very representative of the circulating appAb response. Thus, the repertoire of circulating plasma DSA overlapped with the A*01:01-specific B cell compartment in blood and kidney.

While the 50 rmAbs collectively mirrored the reactivity of the serum DSA response, each rmAb exhibited a specific pattern of reactivity (Figure 4A-B, Figure S3B). Given that there were seven residues (Figure S3C) with at least 50 $Å^2$ of solvent-accessible surface area[15] that were double-mismatched between the donor's typing (A*01:01) and both of the recipient's HLA-A locus alleles (A*24:02 / A*30:01), we hypothesized that we might find 7 different patterns of reactivity within the rmAb repertoire and that each pattern would be responsible for $1/7^{th}$ (or 14.2%) of the anti-A*01:01 B cell response. Compared to this null hypothesis, the A*01:01-monospecific reactivity pattern (referred to as $A1^+$) was significantly more represented in the collection of rmAbs, with 17/50 (34.0%) rmAbs binding to A*01:01 alone (Figure 4C, Figure S3B). Within the rmAb repertoire, a total of eight distinct lineages contained 17 rmAbs with an $A1^+$ monospecificity (Figure S4A). The second most common pattern of reactivity, specific for only $A*01:01^+A*29:02^+A*36:01^+A*80:01^+$, (referred to as $A1^+A29^+A36^+A80^+$) featured 5/50 (10.0%) rmAbs spread across two lineages (Figure 4C, Figure S4B). A third lineage containing the largest number of rmAbs (Lin1, n=10 rmAbs) displayed multiple patterns of reactivity among its members; however, 9/10 members each bound at least six consensus alleles: $A*01:01^+A*03:01^+A*11:01^+A*24:02^+A*36:01^+A*80:01^+$ (Figure S4C). In all, we identified 22 unique patterns of reactivity within the rmAb repertoire (Figure S3B) – a number that was far greater than the number of double mismatched residues between donor and host HLA.

Next, we investigated whether particular patterns of reactivity were associated with the largest lineages in the A*01:01-specific IgV_H-seq repertoire. The highest percentage of sequences linked to an A*01:01-specific rmAb was Lin4, which represented 20.0% of the sequences in the A*01:01 specific IgV_H-seq repertoire. The rmAbs in Lin4 displayed $A1^+A29^+A36^+A80^+$ reactivity (Figure 4D, S4B). Lin12, which also displayed $A1^+A29^+A36^+A80^+$ reactivity, comprised 19.0% of A*01:01-specific IgV_H sequences (Figure 4D). Thus, $A1^+A29^+A36^+A80^+$ rmAbs were linked to two lineages that constituted 39.0% of all A*01:01-specific IgV_H sequences. $A1^+$ monospecificity was also heavily represented in the A*01:01-restricted IgV_H-Seq repertoire, with 7 distinct lineages that together comprised 36.9% of the A*01:01-specific IgV_H repertoire (Figure 4D). Thus, despite appreciable diversity in the HLA-reactivity patterns within the HLA A*01:01-specific B cell response, two patterns of HLA reactivity, which encompassed 75.9% of all A*01:01-specific IgV_H sequences, dominated the A*01:01-specific IgV_H-Seq repertoire.

HLA epitope recognition by immunodominant alloreactive B cells.

Although the number of HLA residue mismatches between self and non-self positively correlates with formation of DSA responses,[22] the relative immunogenicity of individual polymorphic residues is unknown. We hypothesized that the most solvent-accessible, most self-dissimilar polymorphic residues would drive immune focusing of the alloreactive response. To test this hypothesis and gain a better understanding of the epitopic and structural basis of HLA immunogenicity in the context of transplant rejection, we employed X-ray crystallography and cryo-electron microscopy (cryoEM) to determine the structures of 3 rmAb/HLA A*01:01 complexes. These included the E07 rmAb, which exhibited the immunodominant $A1^+$ monospecific pattern of reactivity and was derived from a kidney A*01:01-specific Bmem (Figure 4E) and the L02 rmAb, which exhibited the immunodominant $A1^+A29^+A36^+A80^+$ pattern of reactivity and was also derived from a kidney Bmem (Figure 4F). In addition, we examined the kidney Bmem-derived rmAb M07 (Figure 4G), which was part of the expanded Lin1 that comprised 20.0% (10/50) of the rmAb repertoire (Figure S4C).

For each of these Ab/HLA complexes, we used the same analytic approach to examine the structural basis of HLA recognition by the BCR. First, we determined the structural epitope(s) in HLA A*01:01 that were recognized by the different rmAbs. An epitope was defined as encompassing all AA residues (i) with solvent-accessible surface area (SASA) that was at least partially buried by the binding of the rmAb and/or (ii) that formed close (≤5 Å) contacts between a heavy atom in HLA and a heavy atom in the rmAb. We found that the footprints of the HLA epitopes bound by the three rmAbs were consistent with the size of typical protein epitopes[15] and buried 912 $Å^2$ (rmAb E07), 582 $Å^2$ (L02 rmAb), and 775 $Å^2$ (M07 rmAb) of solvent-accessible surface area on HLA A*01:01 α-chain (Figure 4E-G). The number of AA residues (n=20-22 A*01:01 α-chain residues) present in each of the HLA epitopes (Figure 4E-G) was also consistent with other previously described protein epitopes.[15,57] Consistent with the differences in the HLA reactivity patterns of each of the A*01:01-specific rmAbs, the rmAbs appeared to bind three distinct epitopes on the A*01:01 surface, with only a small amount of overlap in their epitopic footprints (Figure 4H). Indeed, the two rmAbs derived from the two immunodominant alloreactive lineages, E07 (Lin2) and L02 (Lin12), showed no overlap in their epitopes (Figure 4H). Thus, the three rmAbs, which were representative of immunodominant expanded A*01:01-specific B cell lineages, recognized unique epitopes on the donor HLA. These data therefore suggested that distinct residues on the surface of the HLA molecule were likely to drive the specificity, reactivity profile and affinity of these alloreactive rmAbs.

Focused HLA recognition by alloreactive B cells.

Consistent with the data showing that the epitopes on HLA A*01:01 recognized by the three rmAbs were largely non-overlapping, the rmAbs exhibited starkly different reactivity patterns to HLA proteins across a 2000-fold concentration range (Figure 5A-C). In addition, we observed that the binding of each rmAb to the different HLA-A alleles differed greatly, as exemplified by the binding of L02 to A*01:01 (net gMFI=611,885) vs. A*26:01 (net gMFI=28,108) or A*29:02 (net gMFI=274,452) (Figure 5B). Given these results, we hypothesized that the binding and affinity of the rmAbs for the different HLA proteins would be dictated by distinct residues across the surface of the HLA molecule. As a limited number of critical residues have the potential to make outsized contributions

to the binding energy of the Ab/antigen interactions,[58] we predicted that the different reactivity patterns of the rmAbs could be explained by the presence of one or more double-mismatched residues within the epitope of each rmAb. Therefore, we next examined the role that polymorphic residues across the three epitopes played in the HLA-A reactivity patterns of the rmAbs, which included binding of the rmAb to the donor allele A*01:01 and fine specificity (binding to other HLA-A alleles). To define the mismatched residues, we compared A*01:01 (donor) residues to A*24:02 and A*30:01 (self) residues and classified a residue that differed from both self-alleles as a double mismatch (2MM), a residue that differed from only one self-allele as a single-mismatch (1MM), and a residue that was identical to both self-alleles as a zero mismatch (0MM). In agreement with our hypothesis, the $A1^+$ monospecific binding pattern of E07 (Figure 5A) could be potentially explained by two 2MM residues, V158 and R163 (Figure 5D), which were each present in the epitope recognized by E07. These two 2MM residues (V158+R163) were expressed together only on A*01:01 and were not found in the other class I HLA alleles that were tested for reactivity (Figure 5D). Similarly, the epitope recognized by rmAb L02 encompassed a 2MM residue at position 76 (Figure 5E). Consistent with the $A1^+A29^+A36^+A80^+$ reactivity pattern of L02 (Figure 5B), the 2MM A76 residue was expressed by A*01:01, A*29:02, A*36:01 and A*80:01 (Figure 5E). The 2MM residue V150 (Figure 5E) appeared important for the fine specificity, as alleles with the A150 polymorphism (A*80:01, A*29:02) demonstrated lower net gMFIs compared to A*01:01 and A*36:01, which expressed V150. In addition, the 0MM residue A149 (Figure 5E) also appeared to contribute to the fine specificity, as A*26:01 and A*43:01, two alleles that did express A76 but were not appreciably bound by L02 (net gMFI <40,000), both expressed T149. Thus, for L02, two 2MM residues and one 0MM residue appeared to generate the binding and fine specificity of this rmAb. Finally, the epitope of M07 contained one 2MM residue, V150 (Figure 5F). However, this residue did not appear responsible for the binding of M07 to A*01:01 (Figure 5C). Instead, K144, which was a 1MM residue between donor A*01:01 and recipient A*30:01, appeared critical for binding of M07 to A*01:01 (Figure 5F). In addition, residues 127 and 145 appeared important for the fine specificity of M07 as mutations at N127 (1MM) or R145 (0MM) were associated with lower gMFI values for binding of M07 to A*24:02 and A*02:01 alleles (Figure 5F, net gMFI = 134,572 and net gMFI = 19,885, respectively). Thus, the data from these 3 rmAbs strongly suggested that epitopic polymorphisms, including mismatched (2MM and 1MM) residues and residues identical to the recipient's self HLA alleles (0MM), may all contribute to the binding and fine specificity of the HLA-specific B cell response.

Our structural data suggested the polymorphic mismatched (1MM and 2MM) residues within the epitope recognized by the rmAbs might explain the distinct reactivity patterns of each of the rmAbs. As antigenic residues contacted by an Ab must be solvent accessible, we excluded buried, inaccessible residues in our comparisons and focused on mismatched residues with at least 50 $Å^2$ of solvent accessible surface area.[15] We asked whether methods previously employed to classify the immunogenicity of HLA residues,[59-61] including protrusion index, hydrophilicity, isoelectric point, and structural similarity, could be used to identify the mismatched polymorphic residues that were present in the epitope recognized by each rmAb. Interestingly, all these methods failed to discriminate between the residue mismatches that were encompassed within the epitope (epitopic) relative to

the mismatched residues that were located outside of the HLA epitopes (non-epitopic) recognized by the rmAbs (Figure S5A-B).

Since the topography of an antigen may affect immunogenicity and immune focusing to certain subregions,[62] we next assessed the position of the three epitopes recognized by the 3 rmAbs within the quaternary structure of HLA-A*01:01. We found that all three rmAbs made multiple contacts with the α-helices that frame the HLA peptide-binding groove (PBG)[63] (Figure 5G), and that all four of the 2MM residues (A76 [L02], V150 [L02 and M07], V158 [E07], and R163 [E07]) within these epitopes were located within the α-helices that frame the PBG (Figure 5H). Consistent with this conclusion, the 2MM and 1MM epitope residues were located significantly closer to the center of the PBG than the non-epitopic 2MM and 1MM residues (Figure 5I). Therefore, the two criteria of (i) proximity within 16 Å of the PBG center and (ii) at least 60 $Å^2$ of solvent-accessible surface area were sufficient to distinguish the four epitopic 2MM residues from the other 9 2MM residues that were not targeted by the immunodominant alloreactive B cell responses (Figure 5J). Considering the proximity of these residues to the PBG-presented peptide, it was not unexpected to find that portions of the PBG-presented peptide were buried by the rmAbs E07 (1 residue) and L02 (4 residues). Although we did not directly test the magnitude of the peptide contribution to rmAb binding, all three rmAbs bound human A*01:01-typed T cells (Figure S5C), which can present a variety of endogenous peptides. Thus, the peptide itself appeared unlikely to control the binding interaction of E07 or L02. Together, these data suggested that both the location and solvent accessibility of 1MM and 2MM residues may coordinate to render certain residues more immunogenic in the context of allorecognition.

Finally, while the 1MM and 2MM epitopic polymorphic residues appeared to explain much of the HLA reactivity pattern of the A*01:01-specific alloreactive B cells, the affinity of Ab/antigen interactions is influenced by the overall binding interface of the Ab with antigen and associated noncovalent interactions between Ab and antigen.[64] We therefore examined all the AA residues within each of the 3 HLA epitopes to assess whether these residues might also contribute to the strength and reactivity of the A*01:01-specific rmAbs. We observed that the number of hydrogen bonds within the Ab/HLA interface (Figure 5K-M) ranged from 5 (E07), to 6 (L02), to 7 (M07). Of note, 66% of the hydrogen bonds targeted self-identical (0MM) residues, with 3 (E07), 3 (L02), and 6 (M07) hydrogen bonds between the rmAb and a self-HLA residue (Figure 5K-M). Moreover, only a small proportion of the buried surface area of the A*01:01 α-chain epitope was contributed by 2MM residues, ranging from 19.7% for E07 to 1.1% of M07 (Figure 5N). In fact, 0MM residues (identical to both self-alleles) comprised 70.4% of the epitope for E07, 59.3% for L02, and 83% for M07 (Figure S5D). Taken together, these structures revealed that while mismatched residues almost certainly contributed to the binding and fine specificity of anti-HLA Abs, the overall interface between the alloreactive rmAb and the donor HLA-A*01:01 relied on extensive noncovalent interactions with HLA-A self-residues.

The geometry of HLA epitopes.

Given our current understanding that polymorphic HLA residues are targeted by the anti-HLA Ab response,[21,36,65] multiple approaches have been developed to describe the reactivity patterns of anti-HLA Abs. One such approach revolves around "eplets,"[36] which are defined as closely spaced patches of polymorphic residues within 3.5 Å of each other. The eplet model comes from prior studies of mouse Abs showing that the Ab HCDR3 contributes greatly to the specificity of binding interactions.[66] In the setting of alloimmunity, it was hypothesized that the human anti-HLA response would be similarly reliant on the HCDR3 region of the alloreactive Ab, and since the HCDR3 represents only a small portion of the paratope or Ab binding surface, small eplets rather than epitopes would be the key determinants of the anti-HLA B cell response.[36] However, this model has not been examined using structural approaches.[25]

Using our structural data, we first tested the eplet model assumption that the HCDR3 of the A*01:01-specific rmAbs would interact with the critical, reactivity-determining residues.[36] We found that this assumption was incorrect for all three rmAbs. For E07, the light chain LCDR2 domain formed a hydrogen bond with R163 (2MM) (Figure 6A), which contributes to binding of E07 to A*01:01. For L02, the light chain LFR3 domain formed a hydrogen bond with A76 (2MM), which controls binding to A*01:01, and the light LFR3 domain formed a close contact with A149 (0MM), which contributes to the fine specificity of L02 (Figure 6B). Finally, for M07, K144 (1MM), which controls binding to A*01:01, was contacted by both the heavy chain HCDR3 and the light chain LFR2, while R145 (0MM) and N127 (1MM), which contribute to the fine specificity of M07, were contacted by the heavy chain HCDR1, HCDR3, and HFR1 (R145) or the light chain LFR2 (N127) (Figure 6C). We then evaluated the inter-residue distance assumption of the eplet model by calculating the distance between the α-carbons of mismatched residues that contribute to the HLA-A reactivity pattern of each of the rmAbs, including residues that contribute to both the binding and fine specificity of these rmAbs. For E07, the inter-residue distance between the two key binding residues (V158 and R163) was 7.8 Å (Figure 6D). For L02, the inter-residue distance between the key binding residue (A76) and the fine specificity determining residue (A149) was 20 Å (Figure 6E). Finally, for M07, the inter-residue distance between the key binding residue (K144) and one of the two fine specificity determining residues (N127) was 11.8 Å. Thus, the residues responsible for the reactivity profile (binding and fine specificity) of each of these 3 rmAbs were >3.5 Å apart. These data therefore argued that a key core assumption of the eplet model, which argues that the reactivity determining residues of alloreactive Abs must be closely spaced,[36] was not supported by the structural data for these 3 rmAbs.

Many groups have used eplets and their putative patterns of reactivity to surmise the epitope of a given Ab.[22,24,40,61,65,67] However, these inferred epitopes have not been verified by structural methods. We first asked whether the patterns of reactivity assigned to eplets in the HLA eplet registry could be matched to the reactivity patterns of the 50 alloreactive rmAbs. Upon examination of the full HLA-A reactivity patterns of the 50 rmAbs, we observed that 22 (44%) of these rmAbs, including those from the immunodominant Lin12, which contained the structurally defined L02 rmAb, could not be matched to the reactivity pattern of any putative eplet (Figure S6A-B). Second, we asked whether eplets could be used to predict the critical binding- and fine-specificity-

defining residues within the structurally defined epitopes of E07 and M02. The HLA eplet registry identifies the eplet R163+G167 as the only possible set of residues that might explain the A1$^+$ monospecific pattern of reactivity of E07, as A*01:01 is the only HLA allele to express both of these two closely localized (<3.5 Å apart) residues (Figure 6G). However, the structurally-defined epitope of E07 showed that the G167 residue of the putative R163+G167 eplet was not contained within the E07 epitope, as G167 formed no close interatomic contacts with E07 and had 0 Å^2 of surface area buried by the binding of E07 (Figure 6H). The pair of 2MM epitopic residues (V158+R163), which appeared critical for the E07 pattern of reactivity (Figure 5A, 5D), was not a predicted eplet as the V158+R163 inter-residue distance is >3.5 Å (Figure 6D). Although we did not solve the structures of the additional 16 A1$^+$ monospecific rmAbs (Figure S6C), 6 of these rmAbs were clonally related to E07 (Lin2, Figure S4A), suggesting that at a minimum, 7/50 rmAbs in the rmAb repertoire might utilize this specific epitope containing V158+R163 rather than the predicted R163+G167 eplet.[68]

Next, we examined M07, which exhibited the A1$^+$A3$^+$A11$^+$A24$^+$A36$^+$A80$^+$ reactivity pattern that was linked to the 10-member Lin1 (Figure S4C). The HLA eplet registry identifies the eplet K144+R145 (Figure 6I) as the only set of closely localized residues that might explain this A1$^+$A3$^+$A11$^+$A24$^+$A36$^+$A80$^+$ pattern of reactivity. While K144+R145 was contained within the epitope of M07 (Figure 6C,F), the reactivity pattern of M07 was characterized by large differences in the relative fine-specificity for the 6 different HLA-A alleles (Figure 5C). This was particularly evident when binding of M07 to A*24:02 was considered. Since only two residues in the M07 epitope differed between A*01:01 and A*24:02 (N127 vs. K127 and V150 vs. A150, Figure 5F) and the A150 polymorphism did not affect binding of M07 to A*03:01 or A*11:01 (Figure 5C,F), we concluded that K127 of A*24:02 was likely responsible for the observed differences in binding of M07 to A*01:01 versus A*24:02. To test the importance of residue 127 in the binding profile of M07, we examined the affinity of M07 for A*01:01 and A*24:02. We found that the binding affinity of M07 for A*24:02 was 1000-fold lower than that seen for A*01:01 (2.9 μM vs. 2.9 nM, Figure 6J). These data therefore suggested that even among alleles that shared a common putative eplet (K144+R145), additional residues that were remote to the putative eplet appeared to contribute to both the fine-specificity of the rmAbs and to the large differences in affinity of the rmAbs for the different HLA-A alleles. Thus, each of the 3 immunodominant rmAbs highlighted limitations of the eplet model. First, as exemplified by E07, the putative eplet pattern of reactivity failed to predict key specificity-determining residues that were located outside of the 3.5 Å eplet footprint. Second, as shown by M07, even when an eplet's putative pattern of reactivity did correctly identify epitopic residues, additional non-eplet epitopic residues contributed greatly to the affinity profile of the rmAbs. Finally, almost half of all rmAbs, including the immunodominant L02 rmAb, could not be assigned to any putative eplet.

Convergence of alloreactivity and self-recognition in the donor-specific response.

Our structural data indicated that the HLA epitopes recognized by each of the 3 alloreactive rmAbs contained many self-HLA residues and that the rmAbs formed extensive noncovalent interactions, including hydrogen bonds, with multiple self-HLA residues. Given the clear evidence for self-recognition at the structural level, we

re-examined the serologic and monoclonal B cell repertoires for self-reactivity. Not surprisingly, there was no detectable binding of the patient's plasma polyclonal Abs against either of the HLA-A self-alleles (A*24:02 or A*30:01) when measured with a clinically-utilized, multiplexed class I HLA cytometric bead array (Figure 7A). However, we noted that many of the A*01:01-specific rmAbs, which were derived from kidney and blood Bmem and DN B cells, exhibited self-reactivity by binding to self-HLA A*24:02 in the multiplexed cytometric bead array (Figure 7B). Given that these rmAbs were tested at relatively high concentrations (10 μg/mL), we next used L-SPR to compare the affinity of these Abs for both donor-HLA (A*01:01) and recipient self-HLA (A*24:02). We found that 25/50 (50%) rmAbs exhibited measurable self-HLA reactivity by L-SPR (K_D < 4.3 μM), with K_Ds for A*24:02 binding ranging from 0.53 nM to 2.9 μM (Figure 7C). Among the 25 rmAbs with measurable K_Ds for both A*01:01 and A*24:02, 94.7% showed stronger affinities for the donor-HLA allele (A*01:01) than for the self-HLA allele (A*24:02), with a median 24-fold higher affinity for A*01:01 as compared to A*24:02 (Figure 7C).

To better understand how self-recognition might have evolved in the context of the alloresponse, we first analyzed the rmAbs in the lineage containing M07 (Lin1) (Figure 7D) as M07, when complexed with A*01:01, exhibited extensive contacts with self-residues (0MM, Figure S5D). Within Lin1, self-recognition and alloreactivity were strongly and significantly correlated (Figure 7E, r=0.802, p=0.007), suggesting that affinity maturation towards the donor HLA concomitantly supported the development of self-reactivity. Consistent with this conclusion, the K_D of binding to A*24:02 was approximately 100-fold weaker for the Lin1 UCA relative to that observed for the highly mutated members of Lin1 (Figure 7F). In total, we identified 8 distinct lineages that each included somatically mutated A*01:01-specific rmAbs that exhibited increased self-reactivity as compared to the inferred UCA for each of these lineages (Figure 7G). Interestingly, one of these lineages, Lin3, which gained self-reactivity through affinity maturation (Figure 7H) and was dominated by ASCs (Figure 7I), was clonally related to circulating A*01:01-specific appAbs (Figure 7J). This result indicated that self-reactive HLA-specific Abs were present within the alloreactive appAb compartment and that the development of self-HLA reactivity may have occurred concurrently with the affinity maturation of the ongoing alloreactive response. Taken together, these findings showed that breaches of tolerance may be important for licensing the donor-specific alloresponse and suggest that donor-specific Ab responses may result from the convergence of alloreactive and self-reactive B cell responses to a small number of mismatched immunogenic HLA residues and a large number of self-HLA residues. The implication of these findings for potentially improving organ matching and a path to better understanding how the immune system discriminates self from non-self are discussed.

DISCUSSION

Despite the fact that anti-HLA donor-specific Abs[2,4] and HLA-reactive B cells[7-9] are clearly associated with increased risk of organ transplant rejection,[9] the rules governing the recognition of HLA alloantigens by human B cells are still largely unknown. While extensive analyses of the HLA alloreactivity patterns generated by polyclonal DSA present in transplant patient sera have been performed, these patterns cannot be easily deconvoluted to understand the specific reactivity profile of individual allospecific B cells or individual alloreactive Ab molecules.[65] Therefore, to understand the fine specificity of the anti-HLA alloreactive human B cell response and to test the conceptual framework for interpreting HLA-Ab reactivity patterns,[36] the HLA-alloreactive human B cell response needs to be studied at the single cell level with a focus on the structural basis for B cell allorecognition. However, to date, only a single structure containing HLA and an anti-HLA Ab, that latter of which was generated via phage-display, has been solved.[37] Likewise, single cell BCR repertoire and specificity analyses of HLA-specific human B cells have been limited to small numbers of rmAbs.[26,69] Here, we cloned and expressed 50 allospecific BCRs derived from single alloreactive B cells isolated from a transplant patient undergoing AMR. Using these allospecific rmAbs, we showed that the anti-HLA B cell response was affinity-matured, positively selected, shared across kidney and blood, and clonally linked to the clinically important circulating DSA. We identified three clonal lineages of allospecific B cells that collectively contributed to over 70% of the alloreactive repertoire and used representative rmAbs from each of these immunodominant lineages to assess the structural basis for B cell allorecognition. We found that allorecognition focused on solvent-accessible, topographically exposed, mismatched HLA residues present in the HLA epitope. In addition, allorecognition relied on extensive contacts with monomorphic, or self-HLA residues that could contribute to over 90% of a given HLA epitope. Consistent with the structural data derived from the representative alloreactive rmAbs, almost 50% of the collection of affinity-matured alloreactive rmAbs showed detectable binding to self-HLA. By contrast, the majority of the inferred germline (UCA) versions of these Abs (7/9) exhibited no binding to the self-allele. Taken altogether, these findings argued that acquisition of high affinity alloreactivity was supported by a concurrent breach of tolerance to self-HLA. Thus, our data provide a repertoire-based structural framework that can now be used to more comprehensively probe the mechanism(s) by which immunogenicity and self-recognition converge to support the cellular and serologic B cell response during transplant rejection.

Using the 50 donor HLA A*01:01-specific rmAbs, we identified 14 distinct clonal lineages of alloreactive B cells and ASCs. These alloreactive lineages spanned the kidney and blood and were directly linked to circulating DSA. In fact, the rmAb/HLA complex structures evaluated in this manuscript were all generated using rmAbs that were cloned from single alloreactive kidney memory B cells, which were clonally related to other ASCs and B cells found in blood and kidney. This result was consistent with prior studies using mouse models of transplantation[70] as well as a recent human study from Louis and colleagues[27] that demonstrated clonal connections between B cells from the blood and allograft in patients with AMR. In that study, the authors showed that a $CD27^{+}CD21^{neg}$ active Bmem subset was enriched for alloreactive B cells that appeared to be clonally

expanded based on IgV_H gene usage. While we did not specifically examine CD21 expression by Bmems found in kidney and blood, we did identify $CD71^+$ and $CD11c^+$ activated $CD27^+$ Bmem cells as well as $CD27^{neg}IgD^{neg}$ DN B cells within the allospecific B cell repertoire in both kidney and blood. Moreover, all the allospecific B cell populations in kidney and blood as well as the rmAbs generated from the kidney and blood B cells were class-switched, extensively mutated and showed clear evidence of affinity maturation relative to the inferred germline UCAs. Thus, while we cannot say whether the allospecific B cells found in the allograft were generated *in situ* or migrated to the tissue following affinity maturation in secondary lymphoid tissues, we argue that the allograft can serve as a reservoir for multiple diverse clones of alloreactive B cells and ASCs.

Other published studies report that B cells within the allograft are either of low-affinity and polyreactive[71,72] or are autoreactive towards renal-specific or inflammation-specific autoantigens.[33] Indeed, autoAbs to tissue-specific, inflammatory, and endothelial antigens have been observed in multiple solid organ transplantation studies.[33-35] In our analyses, we identified B cells expressing extensively somatically mutated BCRs that recognized self-HLA Class I, one of the most ubiquitously expressed cell surface proteins in the human body. Given the overall homology between self and non-self HLA – in this study, only 13 of 274 (4.7%) HLA-A residues were double-mismatched (2MM) – it is perhaps not surprising that a large portion of the three HLA epitopes recognized by the allospecific rmAbs was comprised of self-identical residues. HLA self-recognition was also seen in the single published structural study[37], which examined the complex of an HLA Class I protein and an HLA-reactive Ab that was isolated from a phage display library. This prior study reported that 30% of the total binding interface between the HLA-specific Ab and HLA class I was through interactions between the monomorphic β2m chain of HLA and the phage display-derived Ab. In our studies, which examined the binding of three representative rmAbs derived from immunodominant HLA-specific B cells selected in an ongoing immune response, we observed no β2m reactivity. Rather, we found that the HLA epitopes recognized by these rmAbs included large swaths of self-residues within the polymorphic HLA α-chain. While many of these self-contacts between the rmAbs and HLA involved important noncovalent interactions, including hydrogen bonds, only one of the three rmAbs demonstrated detectable binding against a self-HLA allele. However, when we examined the entire collection of 50 allospecific A*01:01 binding rmAbs, up to 50% of all the rmAbs, which were found in 8/14 distinct IgV_H lineages, exhibited measurable binding and affinity for the self-HLA allele. In contrast, the inferred UCAs of these rmAbs displayed no or minimal detectable affinity for the self-A*24:02 protein. This was unlike what was reported for B cell responses to tumor antigens, which showed that germline-encoded Abs could exhibit strong self-reactivity to these altered-self tumor antigens.[73] Instead, we observed that self-recognition was associated with ongoing affinity-maturation of the alloimmune response. In fact, the emerging self-reactivity to the self-allele, A*24:02, correlated strongly with the strength of the allo-HLA A*01:01 response in rmAbs derived from Lin1 – a lineage that included 20% of all the A*01:01-specific rmAbs isolated in this study.

Collectively, our data support the conclusion that traditional peripheral B cell tolerance mechanisms appeared to fail in a significant fraction of B cell allo-responses. If so, then we might have predicted that we and others should

detect self-HLA reactive Abs in the serum of transplant patients undergoing rejection. Indeed, when we affinity-purified the polyclonal Ab in plasma we did identify peptides derived from rmAb C16, which we showed exhibits binding to both donor HLA and self-HLA allele. However, the affinity of these dual-reactive Abs for the allo-HLA-A protein was at least 100x better than the affinity of the Abs for the self-HLA protein. This large difference in affinity would likely mean that the dual-reactive Abs would preferentially bind allo-HLA on the allograft rather than self-HLA. However, we suspect that dual-reactive Abs that were not bound to the allograft would then be absorbed by the liver[74] or would be bound in a diffuse fashion by the billions of HLA-A expressing cells in the body – leaving such a low concentration of unbound circulating dual-reactive Abs that they would likely not be detected by standard assays but might be detected via affinity-purification and mass spectrometry. Finally, while we cannot prove why tolerance to self-HLA was breached, we speculate that alloimmune responses to HLA can be initiated and sustained by uncoupling linked recognition between the allo-epitope-specific CD4 T helper cells and the allopeptide-presenting B cells that recognize larger structural determinants containing many self-residues. Thus, analysis of B cell alloresponses to “foreign” polymorphic HLA proteins that are structurally nearly identical to self-proteins may provide us with a window to view how the immune system discriminates between self and altered-self, processes that are also important in the settings of autoimmunity, vaccinology, and cancer immunotherapy.

Although donor-specific HLA-Abs and AMR driven by mismatched HLA proteins[75] remain major causes of graft loss in kidney transplantation, the rules governing the immunogenicity of HLA mismatches are unknown.[24] One framework for understanding HLA mismatches, in which mismatched residues are grouped into small, 3.5 Å-radius patches of mismatched residues called eplets, has been widely used to analyze the reactivity of anti-HLA rmAbs[26,36,65,67,76] and the formation of anti-HLA Abs at the cohort level.[22,40,77-79] However, we found that almost half (44%) of the allospecific rmAbs cloned from the blood and kidney of a transplant patient undergoing AMR could not be matched to any eplet-based putative pattern of reactivity. Our structural data also revealed disconnects between predicted eplets and the actual physical interactions between alloAbs and HLA. Indeed, the eplet model predicted that the pattern of HLA reactivity displayed by the immunodominant E07 rmAb should be due to binding of E07 to the R163+G167 eplet displayed by A*01:01, yet E07 did not interact with G167, which was not solvent accessible, and instead interacted with AV158+R163 – residues that were not classified as a potential eplet. Finally, two core assumptions that underlie the geometric foundation of the eplet model were not met by the three HLA/Ab structures we solved. First, in each structure the Ig heavy and light chains each provided critical contacts with the HLA residues that contribute to HLA binding and fine specificity. This was in opposition to the eplet model that argues that binding of HCDR3 is sufficient to confer HLA reactivity. Second, we found that the key specificity and reactivity-conferring HLA residues within the epitope recognized by the allospecific rmAbs could be considerably farther apart than 3.5 Å. These findings, while in opposition to the eplet model, were entirely consistent with our broad understanding of B cell epitopes, as studies of hundreds of Ab/antigen structures have shown that most epitopes are approximately 1100 $Å^2$ and that the HCDR3 is not the only Ab subdomain that is important for the fine specificity of a given Ab.[15,57,80] Thus, our data strongly suggests

that HLA mismatched residues found outside of the eplet radius, but within the broader framework of a typical Ab footprint, should also be considered as potential key contributors to the binding and fine specificity of alloreactive Abs.

In the context of antiviral responses, AA polymorphisms contribute to immune focusing and immunodominance.[19] In our analysis of a B cell alloimmune response, we observed that two of the allospecific rmAbs displayed reactivity patterns that could be linked to over 70% of A*01:01-specific B cell IgV_H sequences. This suggested that certain HLA residue mismatches may be more immunogenic than others and that particular "immunodominant" mismatched HLA amino acid residues may be responsible for driving B cell alloimmune responses. Although various methods have been used to explain why certain HLA mismatches may be immunogenic, including hydrophilicity,[81] protrusion,[61] and other physicochemical features,[59,60,79] these approaches have all generally lacked discriminatory power. For two structures (E07/A*01:01 and L02/A*01:01), we found that double-mismatched (2MM) residues with considerable solvent-accessible surface area provided binding and fine-specificity contacts for the anti-HLA Ab. In addition, we found that in all three structures, these double-mismatched (2MM), solvent accessible residues were positioned on the highly exposed α-helices framing the HLA peptide-binding groove. Given that this topographically exposed domain serves as the binding site for other immune receptors, including the T cell[82] and NK cell receptors,[83] it is tempting to speculate that the exposed face of HLA also supports recognition and binding by BCRs that can recognize solvent accessible mismatched residues. If this immunogenicity hypothesis is supported by additional structures of HLA/alloAb complexes, then one could imagine using these data to better define the rules governing immunodominance and immunogenicity in alloimmunity – which in the future might be used to optimize organ matching.

In conclusion, this work provides a framework for understanding the structural and molecular basis of B cell epitope targeting in organ transplant rejection. It highlights the anatomy of this B cell alloresponse as it spans tissue and blood and results in the generation of a high-affinity donor HLA-specific response that can be detected in the circulating DSA compartment. Although non-self-HLA recognition appears critical for the generation of an alloimmune B cell response, self-recognition and a possible failure of peripheral linked-recognition appear to conspire to generate self-HLA recognition within the alloreactive response. These findings suggest a path forward for understanding immunogenicity of donor HLA in the context of transplantation as well as the opportunity to use anti-HLA responses to better understand more fundamental questions of tolerance and immunity.

Limitations of the study

This study was conducted with samples from a single patient, thus additional studies will be needed to assess the generalizability of these findings to other transplant patients. However, it is important to note that despite the samples being derived from a single patient, the depth of sampling within the monoclonal compartment was approximately 25-fold greater than any previous study,[26] and the thousands of A*01:01-reactive IgV_H sequences,

14 distinct A*01:01-reactive lineages, and three dominant specificities suggest that we examined a robust yet diverse alloimmune response in this individual. Although this patient did have systemic lupus erythematosus (SLE), there was no evidence of lupus nephritis within the allograft by histologic assessment, and there is no evidence using high-resolution HLA typing and clinically relevant MFI thresholds to suggest that patients develop anti-HLA autoantibodies in SLE.[84] Instead, our structural and biomolecular interaction data support the conclusion that a subset of the rmAbs generated in our study are specific for donor HLA and can also recognize self-HLA. Importantly, these alloreactive Abs are not polyreactive, as is often observed in autoreactive Abs found in SLE patients.[85] Rather, the allospecific rmAbs from this individual recognized HLA epitopes that were of the expected dimensions with the expected number of epitopic residues that included mismatched and self-HLA residues. Most importantly, we found that self-recognition was correlated strongly with improved affinity for the alloantigen, suggesting that the reactivity to self-HLA came “along for the ride” rather than serving as the instigator of the immune selection process. Finally, it will be important to not only investigate B cell alloimmune responses in other individuals but to include patients with different rejection pathologies involving a variety of mismatched HLA proteins, including HLA class II, which is commonly targeted by the alloreactive B cells in late transplant rejection.[4] While it is possible that there will be differences in the immune response to mismatched HLA based upon the class or locus of the mismatched HLA, we speculate that the immunogenicity “rules” will be similar given the structural similarities between class I and class II,[86] particularly in the face framing the peptide binding groove.

ACKNOWLEDGMENTS

We would like to acknowledge the NIH Tetramer Core facility for HLA-A*01:01, HLA-A*02:02, and HLA-A*24:02 tetramers, monomers, and expression plasmids. We thank Vidyasagar Hanumanthu, director of the UAB Flow Core Facility, and Dr. Michael Crowley, director of the UAB Heflin Genomics core, for their assistance with these studies. We thank the CryoEM facility of La Jolla Institute for Immunology, as well as philanthropic support of this facility.

AUTHOR CONTRIBUTIONS

F.E.L. and J.T.K. conceived the study. F.E.L. secured funding, oversaw project administration, participated in the original drafting of the manuscript and its revisions, and provided direct supervision. J.T.K. conducted experiments, performed formal analyses, curated data, visualized data, wrote the original draft of the manuscript and participated in its revisions. R.G.K. conducted experiments, provided methodologic expertise, validated key reagents, conducted formal analyses, curated data, assisted with proteomic visualization, and provided supervision. T.J.G. provided methodologic expertise, conducted experiments and formal analyses, curated data, and provided supervision. J.L.K conducted formal analyses of structural data. C.F.F. provided methodologic expertise, conducted formal analyses, and generated visualizations of repertoire data. A.F.R provided methodologic expertise and supervision. R.D.A, S.Q., A.S.S., and B.J.M. conducted experiments. K.J.M., A.R.C., G.Y., M.E.H., and J.A. provided key reagents. D.B.G., S.K., S.C.O., V.K., J.A.H., and F.D.R assisted with formal analyses. J.F.K. and T.D.R supervised and facilitated project administration. E.O.S supervised, facilitated project administration, and provided critical resources. P.M.P. reviewed and edited the manuscript. All authors reviewed and approved the final version of the manuscript.

DECLARATION OF INTERESTS

The authors have no conflicts of interest to declare.

FUNDING

Research reported in this manuscript was supported by grants from the National Institutes of Health (NIH): NIDDK T32 DK007545 to J.T.K., NIAID T32 AI007051 to J.T.K., and NIAID U19 AI142737 (F.E.L., J.F.K., T.D.R. and A.F.R.) The UAB CryoEM Facility is supported by an NIH Office of the Director S10 OD024978 award. The UAB CryoEM and X-ray Diffraction Facilities are supported by the UAB Institutional Research Core Program and the O'Neal Comprehensive Cancer Center with funding from National Cancer Institute (NCI) P30 CA013148 and NIH Office of the Director S10 OD024978. The UAB Flow Cytometry and Single Cell services Core is supported by NIH grants to the O'Neal Comprehensive Cancer Center (P30 CA013148) and the Center for AIDS Research (P30 AI027767). The UAB Mass Spectrometry / Proteomics Core is supported by the O'Neal Comprehensive Cancer Center with funding from NCI P30 CA013148. Data were collected at Southeast Regional Collaborative Access Team (SER-CAT) 22-ID beamline at the Advanced Photon Source, Argonne National Laboratory. SER-CAT is supported by its member institutions, and equipment grants (S10_RR25528, S10_RR028976 and

S10_OD027000) from the National Institutes of Health. Use of the Advanced Photon Source was supported by the U.S. Department of Energy, Office of Science, Office of Basic Energy Sciences, under Contract No. W-31-109-Eng-38. The content is solely the responsibility of the authors and does not necessarily represent the official views of the National Institutes of Health.

MAIN FIGURE LEGENDS

Figure 1. Intragraft and circulating B cells and antibody-secreting cells show features of antigen-driven selection against donor HLA.

(A-C) Immunofluorescent histology of the rejected kidney showing $CD4^+$ T (red) and $CD19^+$ (green) B cells **(A)**, proliferating $Ki67^+$ (green) $CD19^+$ (red) B cells **(B)**, and $CD19^+$ (red), $CD38^+$ (blue), intracellular IgH^+ (green) antibody-secreting cells (ASCs) **(C)**. DAPI nuclear staining shown as blue in panels **(A)** and **(B)** and gray in panel **(C)**.

(D-E) Multiparameter flow cytometry analysis of rejected kidney using CD27, CD38 and IgD to define indicated B lineage subsets (**D**) and CD71 (**E**) to identify activated B lineage cells.

(F) Alluvial plots showing lineage relatedness between $CD19^+IgD^{neg}$ ASCs ($CD27^+CD38^+$), double negative (DN) B cells ($IgD^{neg}CD27^{neg}$) and Bmem (MEM, $CD27^+$ nonASCs) isolated from a rejected transplanted kidney (KD). Shared lineages (ribbons) ranked by size in each B cell subset with lineages shared between all subsets (orange) or between two subsets (green). Numbers of sorted cells and non-singleton lineages for each subset are provided. %D50 defined as: (# lineages in top 50% of subset A / # of lineages in the top 50% of subset B) x 100. See *Methods* for details.

(G) Circos plots showing connections between lineages of B cell subsets isolated from rejected KD and peripheral blood (PBL). Size-ranked lineages representing the top 20% of size-ranked sequences within a given subset are colorized. See *Methods* for details.

(H) Scatterplot comparing the size of specific B cell lineages in KD (x-axis) and PBL (y-axis). Lineage size represented as % sequences of that lineage within kidney or blood. Lineages not detected in a tissue reported as 0%.

(I) Trajectory of anti-HLA-A*01:01 DSA response in kidney transplant patient based upon clinical HLA-Ab testing. Clinical index diagnosis of antibody-mediated rejection (AMR) and timing of transplant nephrectomy indicated.

(J) Binding of antigen-experienced $CD19^+IgD^{neg}$ transplant kidney nephrectomy and peripheral blood B cells to fluorochrome-labeled recombinant HLA-A*01:01 tetramers. Dual tetramer-stained cells index-sorted for single cell recombinant monoclonal antibody (rmAb) production.

(K) Binding of rmAbs (n=50), generated from single-cell sorted HLA-A*01:01-specific B cells (see **J**), or negative control (NC) human rmAbs to HLA-A*01:01-coated microbeads. Data reported as geometric mean fluorescent intensity (gMFIs).

(L-M) Mutation frequencies (**L**) and isotype distribution (**M**) in kidney and blood B cell IgV_H sequences assigned to A*01:01-specific B cell lineages. Violin plots (**L**) showing IgV_H-region nucleotide (NT) mutation frequency distributions with median number of mutations in each bulk subset and rmAb subset shown.

See Supplemental Figures for: schematic of experimental design (Figure S1); analyses of bulk B cell subsets (Figure S1); analyses of HLA-A*01:01-specific B cells and A*01:01-specific rmAbs (Figure S2).

Figure 2. Alloreactive B cells undergo clonal expansion and affinity maturation.

(A-C) Phylogenetic trees showing 3 representative IgV_H lineages of A*01:01-specific B cells and ASCs. Tree edges trace IgV_H mutations from the inferred unmutated common ancestor (UCA, black node) through inferred mutation nodes (gray nodes) and observed nodes. Observed node color denotes B cell subset(s) assigned to each node. Node shape indicates tissue of origin for cells represented in each node. Nodes containing IgV_H sequences from A*01:01-specific rmAbs indicated in cyan. Orange line indicates V_H-region nucleotide (NT) mutation accumulation.

(D) Analysis of the A*01:01-specific IgV_H-Seq repertoire (n=4142 sequences) from kidney and blood B cell subsets. Percentages of sequences assigned to different A*01:01-specific expanded lineages provided. Individual lineages that represent at least 2.5% of the A*01:01-specific IgV_H sequence repertoire shown.

(E) Distribution of different B cell subsets within A*01:01-specific B cell lineages.

(F) Binding kinetics of A*01:01-specific rmAbs E07 and L02 to recombinant HLA-A*01:01. Binding reported as a function of increasing rmAb concentration, fit as 1:1 Langmuir curves by localized surface plasmon resonance (L-SPR). Affinity of binding reported as equilibrium constants (K_D).

(G) Affinity (K_D) of A*01:01-specific rmAbs (n=50) for A*01:01. Dotted line indicates limit of detection (K_D 4.3 μM).

(H) Binding to A*01:01 by representative Lin4 and Lin12 A*01:01-specific rmAbs and rmAbs encoding the inferred Lin4 and Lin12 UCAs. Data shown as increasing concentrations of the rmAbs (x-axis) and gMFI of binding to A*01:01 cytometric beads (y-axis). K_D values for rmAbs indicated.

(I) Paired comparison of mutated A*01:01-specific rmAbs to rmAbs encoding the inferred UCA for each somatically mutated rmAb (n=36 pairs). Affinity (K_D) for binding to A*01:01 reported.

(J) Paired comparison of somatically mutated A*01:01-specific rmAbs to rmAbs encoding the predicted UCA for each mutated rmAb (n=9 pairs representing 9 A*01:01-specific B cell lineages). Data, showing the rmAb with the highest affinity in each lineage, reported as affinity (K_D) for binding to A*01:01.

Statistical analyses in **(I-J)** performed using the Wilcoxon matched-pairs signed rank test.

Figure 3. Donor-specific ASCs link the cellular and serologic alloreactive repertoires.

(A) Lin4 phylogenetic tree showing A*01:01-specific B cells and ASCs. Tree edges trace IgV_H mutations from an inferred unmutated common ancestor (UCA, black node) through inferred mutation nodes (gray nodes) and observed nodes. Observed node color denotes the B cell subset(s) assigned to each node and node shape indicates tissue of origin for cells represented in each node. Nodes containing IgV_H sequences from A*01:01-specific rmAbs indicated in cyan.

(B-E) Alignment of plasma proteomics data to A*01:01-specific rmAb sequences. Peptide sequences derived from LC-MS/MS analysis of A*01:01 affinity-purified plasma Abs (appAbs) were aligned against A*01:01-specific rmAb sequences. Exact peptide matches are plotted by position within the rmAb VDJ amino acid (AA) sequence. Peptide sequences overlapping the rmAb heavy chain CDR3 (HCDR3) are shown. Affinity (K_D) of the rmAb for A*01:01 is indicated.

(F) Column plot showing number of IgV_H sequences derived from bulk sorted blood and kidney ASCs in each A*01:01-specific lineage. A*01:01-specific lineages detected in the appAb proteome are colored.

Figure 4. Immune focusing and dominant reactivity patterns within the alloreactive B cell repertoire.

(A) Binding of rmAbs (n=50) to 21 individual HLA-A alleles displayed on microbeads. Data reported as net gMFI following normalization against a panel of negative (influenza-specific) control human rmAbs. Data clustered using Euclidean distance.

(B) Comparison between HLA reactivity profiles of A*01:01-specific rmAbs (n=50) and circulating A*01:01-affinity purified plasma Ab (appAb). Upper plot shows number of rmAbs that bound (net gMFI ≥40,000) each HLA-A protein. Bottom plot shows the net gMFI for appAb, diluted 2-fold from 5 µg/mL to 2 ng/mL.

(C) Pie chart depicting the most common HLA reactivity patterns for A*01:01-specific rmAbs (n=50). rmAb HLA reactivity patterns were clustered by converting net gMFI of each allele into binary variables (net gMFI ≥40,000 = positive or net gMFI <40,000 = negative). Lin1 rmAbs (n=10, 20%), which demonstrated multiple reactivity patterns, are indicated in orange. See Figure S3 for clustering and reactivity pattern counts, and Figure S4 for the Lin1 consensus pattern of reactivity.

(D) Pie chart depicting the most common HLA reactivity patterns for A*01:01-specific IgV_H lineages (n=4142 sequences). For each lineage, a dominant pattern of anti-HLA reactivity (See Figure S4) was assigned by identifying the specific reactivity pattern bound by least 50% of the rmAbs in the lineage.

(E-G) Structures showing IgH and IgL chains of A*01:01-specific rmAbs E07 (**E**), L02 (**F**) and M07 (**G**) bound to HLA A*01:01. HLA-A*01:01 α-chain (coral), β2-microglobulin (dark khaki), and peptide (slate gray). Number of A*01:01 α-chain residues contained within each epitope and the A*01:01 α-chain surface area buried by the binding of the rmAb are indicated.

(H) Merged, simulated structure showing binding of rmAbs E07, L02, and M07 to HLA A*01:01.

Statistical analysis in **(C)** tested a null hypothesis that there would be 7 different patterns of reactivity corresponding to the 7 solvent accessible and double-mismatched residues expressed by donor A*01:01 relative to recipient HLA A*24:02 and A*30:01. Data analyzed using a binomial test with an expected frequency for an A*01:01-monospecific pattern of 14.3%. The confidence interval of the proportion was calculated using the Wilson/Brown method. An A*01:01 monospecific pattern of reactivity was observed significantly more often than expected (34.0% vs. 14.3%, p=0.0004).

See Supplemental Figures for: cytometric bead data (Figure S3, Figure S4)

Figure 5. The structural basis of alloreactivity.

(A-C) HLA-A reactivity profiles showing binding of rmAbs (E07 (**A**), L02 (**B**) and M07 (**C**)) to 21 HLA-A alleles displayed on microbeads. Data reported as net gMFI of the average of 2 technical replicates of rmAbs that were diluted from 10 µg/mL to 5 ng/mL. Donor allele ("d") and self-alleles ("s") indicated. HLA proteins bound by rmAbs (10 µg/mL) with net gMFI ≥40,000 indicted in bold.

(D-F) Identification of amino acid (AA) residues in HLA A*01:01 that contribute to the binding and fine specificity of rmAbs E07 (**D**), L02 (**E**) and M07 (**F**). AA residues in each structurally defined HLA A*01:01 epitope (epitopic residues) are indicated by position (AA 1-274). The epitopic AA residues in HLA A*01:01 shown in alignment with other HLA-A alleles, including self-alleles A*24:02 and A*30:01. AA are colored based on chemical properties (yellow=aromatic, red=acidic, blue=basic, aliphatic=orange, polar=green). Residues identical to the A*01:01 donor allele are shown as dots (“.”). Residues mismatched against the A*01:01 donor allele are indicated with the one letter AA code. Selected residues double-mismatched against both self-alleles (2MM, red), single-mismatched (1MM) against one self-allele (A*24:02, orange or A*30:01, yellow), or identical to both self-alleles (0MM, black) indicated. Alleles with binding of net gMFI ≥40,000 at 10 µg/mL bolded.

(G) Depiction of the three epitopic footprints of E07, L02, and M07. Regions of overlap between epitopes indicated.

(H) Location of the four double-mismatched (2MM) residues (A76, V150, V158, R163) within the A*01:01 epitopes bound by rmAbs E07, L02, or M07. Peptide (grey), 2MM residues (red), α-helices adjacent to HLA A*01:01 peptide-binding groove (PBG, teal).

(I) Distance of solvent accessible 2MM residues (left, n=7) or 1MM or 2MM residues (right, n=14) from the center of the PBG in A*01:01 (see Figure S3C for all 2MM residues between the two self-HLA alleles and A*01:01). Residues contained in the HLA epitopes bound by E07, L02, or M07 (red) and residues outside of the HLA epitopes (black).

(J) Scatterplot comparing the solvent-accessible surface area (x-axis, in $Å^2$) of all 2MM epitopic residues (n=4, in red, blue, orange or green), 2MM non-epitopic residues (n=9, in yellow) and all 0MM or 1MM residues (n=261, in grey) to the distance of each residue from the center of the PBG (y-axis, in Å).

(K-M) Heatmaps depicting the physicochemical and interfacial features of the epitopic residues in A*01:01 α-chain bound by E07 (**K**, n=20 residues), L02 (**L**, n=21 residues), and M07 (**M**, n=22 residues). Shown are residues involved in hydrogen bonds (left), 0MM, 1MM or 2MM residues (middle) and amount of solvent-accessible area in A*01:01 buried by the bound rmAb (right).

(N) Mapping the contribution of 2MM residues to the HLA A*01:01 α-chain epitopes bound by E07 (left), L02 (middle) and M07 (right) showing 2MM epitopic residues (firebrick red) and all other epitopic residues (black). Contribution of 2MM epitopic residues to the total surface area of A*01:01 α-chain buried by the bound rmAb indicated as % of buried surface area within the epitope.

Statistical analysis **(I)** performed using an unpaired t-test. All distributions passed normality (Shapiro-Wilk test).

See Supporting Figures for: additional A*01:01 epitope structure data (Figure S5).

Figure 6. The geometry of HLA epitopes.

(A-C) Depiction of selected noncovalent interactions between E07 **(A)**, L02 **(B)**, and M07 **(C)** mAbs and A*01:01 epitopic residues identified (see Figure 5D-F) as contributors to the binding and fine-specificity of each rmAb. HLA A*01:01 (coral), peptide (gray), 2MM epitopic residues (firebrick red), all other epitopic residues (black or highlighted yellow or gold).

(D-F) Distance between residues in the HLA A*01:01 epitope footprints that contribute to the binding and fine specificity of E07 (**D**), L02 (**E**), and M07 (**F**). Reported as distance (in Å) between the Cα in each residue and colorized as in panels A-C.

(**G**) Alignment of 21 HLA-A alleles (rows) with the putative R163+G167 eplet found in A*01:01, compared to the V158+R163 pair of 2MM residues contained in the structurally-defined E07 epitope. The AA at positions 158, 163 and 167 are colored based on chemical properties of the residue (yellow=aromatic, red=acidic, blue=basic, aliphatic=orange, polar=green). Residues identical to the A*01:01 reference donor allele shown as dots (“.”). Residues that mismatched against the A*01:01 donor allele shown as the one letter AA code.

(H) Comparison between the structurally-defined E07 epitope with the 2MM residues (V158, R163 in firebrick red) that contribute to binding and fine-specificity and the putative eplet for E07 (R163+G167 eplet, G167 in cyan).

(**I**) Alignment of 21 HLA-A alleles (rows) with the putative K144+R145 eplet found in A*01:01. The AA at positions 144 and 145 colored as described for panel C. Residues identical to the A*01:01 reference allele shown as dots (“.”). Residues mismatched against the A*01:01 reference allele shown as the one letter AA code.

(J) Comparison between binding of rmAb M07 (Lin1) to A*01:01 and A*24:02. Data shown as increasing concentrations of the rmAb (x-axis) and gMFI of binding to A*01:01 (black) and A*24:02 (blue) arrayed microbeads (y-axis). Affinity (K_D) of binding to each HLA-A reported.

Figure 7. Convergence of allo- and self-reactivity in donor-specific B cell responses.

(A) Heatmap depicting the HLA-A reactivity pattern of diluted (1/500 to 1/320,000) recipient plasma. Data reported as net gMFI (average of 3 replicates/dilution) for binding to 21 HLA-A alleles. Donor (“d”) and self (“s”) alleles indicated.

(B) Binding of A*01:01-specific rmAbs (n=50) or negative control (NC) human rmAbs to self-HLA A*24:02-coated microbeads. Reported as net gMFI.

(C) Comparison of rmAb (n=50) affinity (K_D) for alloantigen A*01:01 and self-antigen A*24:02. Dotted line indicates limit of K_D determination (4.3 μM).

(D) Lin1 phylogenetic tree showing A*01:01-specific rmAbs, including the self-reactive rmAb M07. Tree edges trace IgV_H mutations from the inferred unmutated common ancestor (UCA, black node) through inferred mutation nodes (gray nodes) and observed nodes. Observed node color denotes the B cell subset(s) assigned to each node and node shape indicates tissue of origin for cells represented in each node. Nodes containing IgV_H sequences from A*01:01-specific rmAbs indicated in cyan.

(E) Correlation analysis comparing the affinity (K_D) of each Lin1 rmAb for alloantigen A*01:01 and self-antigen A*24:02.

(F) Comparison between the A*24:02 binding properties of three representative Lin1 rmAbs (H02, M13 and M07) and rmAb encoding the inferred Lin1 UCA. Data shown as increasing concentrations of rmAbs (x-axis) and gMFI of binding to A*24:02 cytometric beads (y-axis). L-SPR calculated K_D values for rmAbs indicated.

(G) Scatter plot showing fold-change (FC) in affinities (K_D) of inferred UCAs for somatically mutated rmAbs over the rmAbs (n=36). Data displayed as FC in affinity for self-HLA (A*24:02, y-axis) and donor allo-HLA (A*01:01, y-axis) for each rmAb/UCA pair, with lineage assignments for each pair indicated.

(H) Comparison between the A*24:02 binding properties of a representative Lin3 rmAb (C16) and a rmAb encoding the inferred Lin3 UCA. Data shown as increasing concentrations of the rmAbs (x-axis) and gMFI of binding to A*24:02 cytometric beads (y-axis). K_D values indicated.

(I) Lin3 phylogenetic tree, which contains the allo+self-reactive rmAb C16 (see panel H). Description of phylogenetic trees provided in panel C.

(J) Linkage of allo+self-reactive Lin3 rmAb C16 to A*01:01-specific affinity-purified polyclonal plasma Ab (appAb). Peptide sequences derived from LC-MS/MS analysis of A*01:01 affinity-purified plasma Abs (appAbs) were aligned against the C16 rmAb VDJ AA sequence. Peptide sequences overlapping the rmAb heavy chain CDR3 (HCDR3) are displayed. Affinity (K_D) of C16 binding to A*01:01 and A*24:02 indicated.

Statistical analysis **(E)** performed using a nonparametric Spearman correlation with a two-tailed P value.

SUPPLEMENTAL FIGURE LEGENDS

Figure S1. Experimental overview and IgV_H-Seq analyses of kidney and blood B cells and ASCs, related to Figure 1.

(A) Sample acquisition and experimental design. B cells and antibody-secreting cells (ASCs), isolated from a rejected transplanted kidney (KD) and peripheral blood (PBL) of a kidney transplant patient were sort-purified for bulk BCR IgV_H sequencing and generation of single HLA-reactive recombinant monoclonal antibodies (rmAbs). rmAbs were sequenced (IgV_H and IgV_L), tested for specificity, reactivity and affinity, and used in structural studies to identify binding sites (epitopes) on HLA-A*01:01. LC-MS/MS was used to analyze affinity-purified A*01:01-binding Abs (appAbs).

(B) Flow cytometric analysis of B cells from rejected kidney showing gating and sort strategy for bulk B cell subsets and ASC IgV_H-Seq repertoire analysis. ASCs ($CD27^+CD38^+$), double negative (DN) B cells ($IgD^{neg}CD27^{neg}$), Bmem (MEM, $CD27^+$ nonASCs), and naïve (NAV, IgD^+CD27^{neg} nonASCs).

(C) Alluvial plots depicting connections between lineages of memory B cells (MEM, $CD27^+$ nonASCs) isolated from the lung and PBL (left panel) or small intestine (SI) and blood (middle panel) from a non-transplant recipient, brain dead organ donor, or the rejected KD and PBL of the transplant patient (right panel). Lineages defined as having an identical *IGHV* and *IGHJ* gene segment annotation, identical HCDR3 length, and HCDR3 nucleotide sequence identity of >85%. Shared lineages, represented as ribbons with individual lineages ranked by size in each subset. Numbers of sorted cells for IgV_H sequencing, numbers of unique non-singleton lineages and %D50 are indicated. %D50 = (# lineages in top 50% of subset A / # of lineages in the top 50% of subset B) x 100.

(D) Isotype distribution as determined by IgV_H-Seq for KD and PBL bulk $CD19^+IgD^{neg}$ B cell and ASC subsets as defined in panel B.

(E) Comparison of IgV_H mutation frequencies in bulk-sorted $CD19^+IgD^{neg}$ kidney and blood B cells and ASCs as defined in panel B.

Figure S2. Characterization of A*01:01-specific B cells and ASCs, related to Figure 1.

(A) Flow cytometric analysis of B cells from rejected kidney, showing gating to identify A*01:01-specific B cells.

(B) Phenotype of rmAbs (n=50) generated from single index-sorted A*01:01-specific kidney and blood B cells.

(C) Dot plot depicting relative number of sequences and number of V-region nucleotide (NT) mutations for the eight largest A*01:01-specific lineages in the IgV_H-Seq repertoire (n=3851 sequences), divided by tissue and cell subset. Subsets defined as in Figure S1B.

(D) Violin plots showing IgV_H-region NT mutation frequency distributions for the eight largest A*01:01-specific lineages (n=3851 sequences) with median number of NT mutations per lineage indicated.

Figure S3. rmAb binding to HLA cytometric bead arrays, related to Figure 4.

(A) Binding of A*01:01-specific rmAbs (n=50) to microbeads arrayed with 21 distinct HLA-A proteins. Comparison of anti-HLA geometric mean fluorescent intensities (gMFIs) compared to negative control (NC, n=16) human anti-influenza IgG1 influenza-specific rmAbs.[87]

(B) Heatmap indicating the most common patterns of HLA-A reactivity for A*01:01-specific rmAbs (n=50). HLA reactivity patterns for individual rmAbs were determined by converting net gMFI of binding into positive (net gMFI ≥40,000, black squares) or negative (net gMFI <40,000, white squares) binary variables. Net gMFI values were calculated by subtracting the mean negative control gMFI from the allele-specific gMFI of the rmAb.

(C) Amino acid (AA) sequence alignment of donor (A*01:01) and recipient (A*24:02 and A*30:01) alleles, showing double mismatched (2MM) residues (n=13) between donor and recipient. Residues with ≥50 $Å^2$ of solvent-accessible surface area (red arrows), and residues with <50 $Å^2$ of solvent-accessible surface area (black arrows) indicated.

Figure S4. Lineage-specific patterns of HLA-A reactivity, related to Figure 4.

Binding of A*01:01-specific rmAbs to 21 distinct HLA-A proteins displayed on microbeads. Binding to each HLA-A protein reported as net gMFI. Rows annotated with lineage IDs and rmAb names. In **(A)**, for 8 distinct lineages, at least 50% of lineage-specific rmAbs displayed an A*01:01-monospecific pattern of reactivity ($A1^+$ pattern). In **(B)**, for 2 distinct lineages, at least 50% of lineage-specific rmAbs displayed the $A*01:01^+A*29:02^+A36:01^+A*80:01^+$ pattern of reactivity ($A1^+A29^+A36^+A80^+$ pattern). **(C)** Lin1, a lineage with n=10 rmAb members, displayed multiple reactivity patterns. Although we did not identify a single pattern bound by at least 50% of rmAbs, 9/10 rmAbs bound (≥40,000 net gMFI) the same six alleles: $A*01:01^+A*03:01^+A*11:01^+A*24:02^+A*36:01^+A*80:01^+$, forming a consensus pattern of reactivity ($A1^+A3^+A11^+A24^+A36^+A80^+$ pattern).

Figure S5. Physicochemical, structural, and topographic features of HLA epitopes, related to Figure 5.

(A-B) Physiochemical analyses of solvent-accessible (solvent-accessible surface area ≥50 $Å^2$) amino acid (AA) residues that were mismatched (1MM or 2MM) between donor and recipient. In **(A)**, residues that were 1MM or 2MM were grouped together based on whether residues were located within (epitopic, red, n=9 residues) or were not present in (non-epitopic, black, n=5 residues) the epitope footprint recognized by E07, L02, and/or M07. In **(B)**, residues that were 2MM were grouped together based on whether residues were located within (epitopic, red, n=4 residues) or were not present in (non-epitopic, black, n=3 residues) the epitope footprint recognized by E07, L02, and/or M07. Measurements of protrusion index, hydrophilicity, isoelectric point, hydrophobic mismatch, isoelectric point mismatch and dissimilarity are shown for 14 1MM or 2MM residues (**A**) and 7 2MM residues (**B**). For hydrophobicity mismatch, isoelectric point mismatch, and dissimilarity, the absolute difference of those physicochemical parameters was used to calculate a mismatch score for each residue. See *Methods* for details.

(C) Binding of E07, L02, and M07 rmAbs to human $CD3^+$ T cells typed as A*01:01-homozygous at the HLA-A locus. Data reported as gMFI of rmAb binding to T cells (y-axis) as a function of increasing rmAb concentration (x-axis).

(D-F) The amount of the HLA A*01:01 α-chain epitopic surface area that was buried by the binding of rmAb E07 (D), L02 (E) and M07 (F). For each buried surface, the percentage of the surface comprised by residues mismatched against donor A*24:02 (left), mismatched against donor A*30:01 (middle), and identical to both donor A*24:02 and donor A*30:01 (right), are shown.

Data (**A-B**) analyzed using unpaired t-test (normal distribution) or Mann-Whitney test (non-normal distribution) Normality testing performed using Shapiro-Wilk test.

Figure S6. HLA eplets and patterns of reactivity, related to Figure 6.

(A) Patterns of HLA-A reactivity by A*01:01-specific rmAbs that do not correspond to any putative eplets. Data reported as binding of individual rmAbs (n=22, rows) to individual HLA-A alleles (n=21, columns). HLA reactivity patterns for individual rmAbs were determined by converting net gMFI of binding into positive (net gMFI ≥40,000, black squares) or negative (net gMFI <40,000, white squares) binary variables.

(B) HLA Eplet Registry list of eplets (n=35) expressed by A*01:01. The patterns shown indicate whether a predicted eplet (n=35, rows, where the row title lists the polymorphic residues contained in the putative eplet) is expressed by a given HLA-A allele (n=21, columns). Squares showing alleles expressing (garnet) or not expressing (beige) the eplet residue(s).

(C) Patterns of HLA-A reactivity by A*01:01-specific rmAbs that are A*01:01-monospecific. Data reported as binding of individual rmAbs (n=17, rows, Lin2 Abs in green) to individual HLA-A alleles (n=21, columns). HLA reactivity patterns for individual rmAbs were determined by converting net gMFI of binding into positive (net gMFI ≥40,000, black squares) or negative (net gMFI <40,000, white squares) binary variables. At the bottom of the plot, the rmAb reactivity patterns were compared to a putative eplet (R163+G167) and the structurally-verified pair of 2MM epitopic residues in the E07 epitope (V158+R163). Squares showing alleles expressing (garnet) or not expressing (beige) the putative eplet R163+G167 residues. Squares showing alleles expressing (fuchsia) or not expressing (beige) the structurally-verified V158+R163 epitopic residues.

Figure S7. CryoEM structure of L02/M07/HLA-A*01:01 complex, related to Methods.

(A) Representative cryoEM image of L02/M07/HLA-A*01:01 complex.

(B) Fourier shell correlation (FSC) curves of half map FSCs calculated in cryoSPARC and model-map FSC calculated in Phenix. The 0.143 FSC cutoff is indicated by a dashed line.

(C) Reconstruction colored by local resolution.

(D) Representative fit of segments of the atomic model to the reconstructed density map.

METHODS

Subjects. A single kidney transplant recipient with a history of allograft rejection and graft loss who was undergoing transplant nephrectomy was enrolled in this study at the University of Alabama at Birmingham (UAB) in 2021. This study was approved by the Institutional Review Board at UAB (protocol # IRB-300004168), and informed consent was provided by the study subject. Biologic samples from a single deceased organ donor, deemed non-human subjects research by the UAB IRB, were also used.

Multi-color flow cytometry and sorting. The allograft nephrectomy specimen was mechanically and enzymatically digested to yield a single cell suspension. Mononuclear cells were isolated from peripheral blood using density-gradient centrifugation. The cell suspensions were stained with the following anti-human antibody reagents: CD19::V500 (BD, clone HIB19), CD71::BV605 (BD, clone M-A712), CXCR4::BV650 (BD, clone 12G5), FcRL5::BV711 (BD, clone 509F6), CD38::BV786 (BD, clone HIT2), IgD::FITC (BD), CD21::PerCP-Cy5.5 (Biolegend, clone Bu32), CD11c::PE (Biolegend, clone Bu15), CD27::PE-CF594 (BD, clone M-T271), 7-AAD (BD), CD3::PE-Cy5 (Biolegend, clone HIT3a), CD14::PE-Cy5 (Invitrogen, clone 61D3), CD16::PE-Cy5 (BD, clone 3G8), CD56::PE-Cy5 (BD, clone B159), FcRL4::PE-Cy7 (Biolegend, clone 413D12), CXCR5::AF700 (Biolegend, clone J252D5), IgG::APC-H7 (BD, clone G18-145). Cells were also stained with fluorescently labeled tetramers of recombinant HLA-A*01:01 (NIH tetramer core, loaded with peptide VTEHDTLLY, in BV421 and AF647). Cells were sorted on a FACSAria (BD Biosciences) in the UAB Comprehensive Flow Cytometry Core as single cells for recombinant monoclonal expression and in bulk populations for next generation IgV_H sequencing. Data were analyzed in FlowJo v10.8.1 (BD).

Next generation sequencing of the IgV_H repertoire (IgV_H-Seq). IgV_H sequencing was performed as previously described.[87] After sorting B cells subsets directly into lysis buffer (Norgen Single Cell RNA Purification Kit) with 1% mercaptoethanol, lysates were snap frozen on dry ice and stored at -80°C. Total cellular RNA was extracted from bulk sorted B cell and ASC subsets according to the manufacturer's protocol. cDNA preparation was performed (BioRad iScript) per manufacturer's instructions, and DNA amplicon products where generated using Ig-specific variable and constant gene primers.[87] Samples were indexed (Nextera Index Kit, Illumina), purified, quantitated (KAPPA Library Quantitation Kit, Roche) and pooled into libraries. Following generation, libraries were denatured per manufacturer instructions (Illumina) and loaded onto a 600-cycle V3 MiSEQ cartridge (Illumina) for sequencing in the UAB Heflin Sequencing Core.[49]

Bioinformatics and Phylogenetic analyses of IgV_H-Seq data. IgV_H sequencing data were processed and analyzed as described previously.[49] Joined paired-end reads were assembled and quality filtered using FastQC scores. Using IMGT/HighV-QUEST,[88] sequences were annotated, and productive sequences were utilized for downstream analyses. Sequences were clustered into lineages based upon *IGHV* and *IGHJ* gene identity, identical HCDR3 length, and HCDR3 nucleotide identity >85%. Downstream analyses were performed in Matlab

(R2020a, The Mathworks Inc.) or in R (R core team). The outer numbering of Circos plots shows sequence counts for a given tissue-phenotype cell subset. The outer ring is colored (non-gray) for lineages contained in the top 20% of size-ranked lineages in a given tissue-phenotype cell subset. Links connect lineages shared between tissue-phenotype subsets; links are colored (non-gray) if the lineage is contained in the top 20% of size-ranked lineages in at least one tissue-phenotype cell subset. Alluvial plots depict connectivity of shared lineages, with the individual lineages ranked by size in each subset along the y-axis. Shared lineages are represented as ribbons with individual lineages ranked by size in each subset. The numbers of sorted cells for IgV_H sequencing, numbers of unique non-singleton lineages and %D50 are indicated. %D50 = (# lineages in top 50% of subset A / # of lineages in the top 50% of subset B) x 100. Phylogenetic trees were constructed using Phylip's DNA parsimony (dnapars) tool (v3.695; adjusting settings 1, 4, 5, 6 and O setting the germline sequence as the outgroup.[89] Phylogenetic trees were visualized using Cytoscape v3.8.2.[90]

Single cell rmAb cloning, sequencing, and expression. Recombinant monoclonal Abs (rmAbs) were generated as previously described.[87] Briefly, cDNA was generated from mRNA isolated from single non-naïve ($CD19^+IgD^{neg}$) dual HLA-A*01:01 tetramer-binding B cells that were index-sorted into hypotonic lysis buffer in 384-well plates and stored at -80°C. PCR IgV_H and $IgV_{K/L}$ amplicons, generated from the single cell cDNA, were cloned into expression vectors containing the constant regions of human IgG1, IgK, or IgL.[87] Plasmids were sequenced by Sanger sequencing at the Genetic Resources Core Facility (RRID SCR_018669, Johns Hopkins University Department of Genetic Medicine, Baltimore, MD). IgH and IgL plasmids were co-transfected using polyethyleneimine into 293FreeStyle cells (Invitrogen). Supernatants were screened for anti-HLA reactivity using HLA cytometric bead arrays described below. rmAbs were purified using Sepharose G Fast Flow (Cytiva) and rmAb concentrations were determined by UV spectrophotometry (Nanodrop, Thermo Fisher). For structural analysis by x-ray crystallography and cryo-electron microscopy, the VDJ and VJ gene segments from three rmAbs (JTK191B_E07, JTK191B_L02, and JTK191B_M07) were subcloned and expressed as antigen-binding fragments (Fabs). Fabs were purified using CaptureSelect IgG-CH1 Affinity Matrix (Thermo Scientific).

Immunogenetic analysis of rmAbs. IgH and IgK/L sequences were submitted to IMGT/HighV-Quest. IgV_H sequences derived from bulk blood and kidney ASCs and B cells were used for clonal lineage assignment with lineages defined as sequences sharing the same V_H, D_H, J_H, gene assignments, identical HCDR3 and LCDR3 lengths, and >85% NT identity across the HCDR3. rmAbs were grouped into rmAb clusters based on identical V_H, D_H, J_H, $V_{K/L}$, $J_{K/L}$ gene assignments and identical HCDR3 and LCDR3 lengths. rmAbs were then assigned to lineages from the bulk-sorted B cell/ASC subsets (IgV_H-Seq database of blood and kidney Bmem, DN and ASCs), provided the IgV_H sequences shared the same V_H, D_H, J_H, gene assignments, identical HCDR3 length, and >85% NT identity across the HCDR3. If two distinct rmAb clusters were immunogenetically similar to a bulk-sorted IgV_H lineage, but the rmAb clusters utilized two different IgK/L genes (indicating that the rmAb clusters were not clonally related), we assigned only the rmAb cluster with the greater number of rmAbs to the bulk-

sorted IgV_H lineage. Following this assignment process, we identified 14 unique A*01:01-specific IgV_H sequence-based lineages.

Generation of UCA for rmAbs. UCAs for each rmAb were generated by taking the reference sequence of the gene segment alleles (V_H, D_H, J_H, $V_{K/L}$, $J_{K/L}$) as annotated by IMGT/HighV-QUEST and reverting all mutated residues to the reference, or germline, configuration. Nontemplated nucleotides (N-additions) were not modified. Recombinant human IgG1 mAbs were synthesized (Sino Biological) using the AA sequences derived from the predicted UCA nucleotide sequences.

Plasma immunoglobulin proteomics. Plasma Ig proteins from the kidney transplant recipient were affinity-purified on an HLA-A*01:01 column, yielding a polyclonal mixture of affinity-purified plasma Abs (appAbs). appAbs were eluted, buffer-exchanged into PBS, concentrated, and stored at 4ºC. appAbs were reduced with DTT, denatured at 70°C for 10 minutes (min) and separated on a 10% Bis-Tris Protein gel. IgH and IgL bands were visualized with colloidal Coomassie, excised from the gel, equilibrated in 100 mM ammonium bicarbonate (AmBc), and digested overnight with Trypsin Gold, Mass Spectrometry Grade (Promega) or endoproteinase AspN (New England BioLabs) following manufacturer's instructions. Peptide digests were reconstituted in 0.1% Formic Acid/ddH_2O at 0.1 µg/µL and then injected (8 µL each) onto a 1260 Infinity nHPLC stack (Agilent Technologies) and separated using a 75 µm I.D. x 15 cm pulled tip C-18 column (Jupiter C-18 300 Å, 5 µm, Phenomenex). This system runs in-line with a Thermo Q Exactive HFx mass spectrometer, equipped with a Nanospray FlexTM ion source (Thermo Fisher Scientific). Data were collected by the UAB Mass Spectrometry / Proteomics Core in CID mode. The nHPLC was configured with binary mobile phases that includes solvent A (0.1% FA in ddH2O), and solvent B (0.1% FA in 15% ddH2O / 85% ACN), programmed as follows: 10 min at 5% solvent B (2 µL/min, load), 90 min at 5%-40% solvent B (linear: 0.5 nL/min, analyze), 5 min at 70% solvent B (2 µL/min, wash), 10 min at 0% solvent B (2 µL/ min, equilibrate). Following each parent ion scan (300-1200m/z at 60k resolution), fragmentation data (MS2) was collected on the top-most intense 10 ions at 7.5k resolution. For data dependent scans, charge state screening and dynamic exclusion was enabled with a repeat count of 2, repeat duration of 30 seconds (s), and exclusion duration of 90 s. Following this liquid chromatography tandem mass spectrometry (LC-MS/MS), the data were processed, searched, filtered, grouped, and quantified, as previously reported.[91] LC-MS/MS-derived peptide AA sequences were used to probe an AA sequence database including all IgV_H sequences derived from the kidney, blood and rmAb IgV_H libraries. Exact peptide matches to lineage sequences were determined and members of the lineages were ranked by % AA matched of total. Peptide sequences were plotted by position within the IgV_H sequence. The mass spectrometry proteomics data have been deposited to the ProteomeXchange Consortium via the PRIDE[92] partner repository with the dataset identifier PXD043144 and 10.6019/PXD043144.

HLA cytometric bead arrays. HLA-coated microbeads (OneLambda, ThermoFisher or produced in house (see below)) were incubated for 15 minutes (min) with single IgG1 rmAbs, patient plasma, or appAbs diluted in PBS.

Following incubation and washing, beads were incubated with anti-IgG::PE or anti-IgG::AF488 (2.5 µg/mL, Southern Biotech) in PBS with 1% BSA for 15 min. Beads were washed, resuspended in PBS and analyzed on a Cytoflex flow cytometer (Beckman Coulter Life Sciences). Data were analyzed in FlowJo v10.8.1 (BD) and geometric mean fluorescence intensities (gMFI) of binding by each rmAb to each HLA allele-specific microbead were calculated. Anti-influenza human IgG1 rmAbs[87] were used as negative controls. The mean negative control gMFI was subtracted from each allele-specific gMFI to obtain gMFI minus background (net gMFI). We compared the net gMFI of rmAbs against three representative HLA alleles (A*01:01, A*02:01, and A*24:02) to the allele-specific affinity of these rmAbs determined by L-SPR (n=50 rmAbs, n=10 rmAbs, and n=50 rmAbs, respectively). As 100% of tested rmAbs with an allele-specific net gMFI ≥40,000 had demonstrable allele-specific binding (K_D < 4.3 µM) by L-SPR, we used a net gMFI =40,000 as the threshold in reactivity pattern analyses.

Clinical anti-HLA Ab testing. HLA-Ab testing for the recipient was performed by the UAB Histocompatibility Laboratory using its standard clinical assay. The full history of clinical anti-HLA Ab testing data was obtained from the electronic medical record. Briefly, patient sera were pre-treated using a Melon IgG spin column and analyzed neat according to manufacturer instructions (OneLambda, ThermoFisher) as previously described.[93] Proprietary software was used for calculation of mean fluorescent intensity (MFI). This method was used for the clinical data shown in Figure 1I. All other HLA-Ab cytometric bead array data utilized methods described above.

High-throughput localized surface plasmon resonance. Localized surface plasmon resonance (L-SPR) data were collected using a 1:1 referencing system on the Nicoya Alto HT-SPR instrument according to manufacturer's recommendations and as described.[94] Briefly, biotinylated recombinant HLA-A*01:01 (500 µg/mL) or HLA-A*24:02 (200 µg/mL) was resuspended in PBS containing 0.05% Tween-20 and immobilized on an EDC/NHS-activated carboxyl sensor (Nicoya) for 20 min. The rmAbs (analytes) were diluted to 1.3 µM in PBS containing 0.05% Tween-20. Single-cycle kinetic analyses were performed at 25°C with five threefold analyte dilutions, with maximum concentrations of 433 nM. Kinetic fitting was performed using a 1:1 Langmuir model within the Nicoya user portal. For datasets that poorly fit with a 1:1 Langmuir model, an affinity fit model was used (TraceDrawer, Ridgeview Instruments). The limit of detection for the equilibrium constant (K_D) was estimated to be 4.3 µM, or 10 times the highest concentration of analyte tested (433 nM). Recombinant mAbs with responses below 50 plasmon resonance response units or without monotonic increases across increasing concentrations were judged to not have measurable binding by L-SPR. For visualization and for calculations of fold-change in affinity, if a rmAb had no detectable binding by L-SPR (K_D >4.3 µM), a K_D of 5 µM was used.

Recombinant protein synthesis. For cytometric bead arrays and L-SPR experiments, biotinylated HLA-A*01:01, HLA-A*02:01, and HLA-A*24:02 were obtained from the NIH Tetramer Core Facility. For structural studies, recombinant, unbiotinylated HLA-A*01:01 was synthesized as previously described.[95-97] Briefly, A BL21 (DE3) *E. Coli* chemically competent cells were transfected with either *01:01 α-chain (pTCF5) or β2m (pTCF158) plasmids (NIH Tetramer Core Facility). Expressed recombinant proteins were extracted from inclusion bodies,

refolded with a suitable peptide (VTEHDTLLY, Biosynth Gardner, MA)[98] at 4°C, purified by ion exchange chromatography (DEAE-C) and size-exclusion chromatography, buffer exchanged into PBS, concentrated, and stored at 4ºC.

Generation of HLA-coated microbeads. Custom cytometric bead arrays were generated as previously described[87] using 4 µm and 5 µm carboxy functionalized array kits (Spherotech, PAK-4067-8K and PAK-5067-10K). Streptavidin (SA, Southern Biotech) was buffer-exchanged using PD-10 columns (Cytiva) into PBS and diluted to 2 mg/mL. To conjugate SA to the beads, $1x10^8$ Spherotech beads were resuspended in 0.5 mL SA and 0.5 mL of 6 mM 1-Ethyl-3-(3-dimethylaminopropyl)carbodiimide (EDC) in 0.05 M MES buffer pH 5.0 (Pierce). The reaction mixture was rotated at room temperature overnight and then quenched with 0.1 mL of 1 M tris pH 8.0. The beads were washed twice in 1 mL PBS and resuspended in PBS with 1% BSA and 0.005% NaN_3 and stored at 4ºC until HLA conjugation. Recombinant, biotinylated HLA (see above) was incubated with SA conjugated beads at 1 mg/mL / $1x10^8$ microbeads overnight at 4ºC. Following HLA conjugation, the beads were washed twice in 1 mL PBS and resuspended in PBS with 1% BSA and 0.005% NaN_3 and stored at 4ºC until used.

X-ray crystallography and CryoEM sample preparation. HLA/Fab complexes were generated by mixing recombinant, unbiotinylated HLA-A*01:01 (see above) with either one Fab (1:1 molar ratio for E07/A*01:01, on ice) or with two Fabs (1:1:1 for L02/M07/A*01:01). Complexes were purified using size-exclusion chromatography on a Superdex S200 column in PBS. Complexes were concentrated and prepared for subsequent structural studies.

X-ray crystallization, data collection, structure determination, and refinement. Purified E07/A*01:01 complexes were concentrated to 9.8 mg/mL and screened for crystallization conditions against commercially available kits using a Mosquito liquid handling robot (SPT Labtech). Crystallization conditions were optimized, and diffraction quality crystals were grown in 1.015 M sodium citrate tribasic dihydrate, 0.1 M sodium cacodylate pH 6.5 at a 1:1 ratio of protein to precipitating agent. Crystals were cryo-protected in crystallization solution supplemented with 20% (v/v) ethylene glycol and frozen. Diffraction data was collected at SER-CAT beamline 22-ID and processed with HKL2000.[99] Data analysis was performed at UAB. Crystals exhibited a pseudo-cubic symmetry but had true C2 symmetry. Initial phases were solved by molecular replacement with PHASER [100] using prior models of HLA (PDB ID: 6AT9),[101] antibody domains: VH (PDB ID: 6PZH),[102] VL (PDB ID: 4HK0),[103] CH1 (PDB ID: 6AZZ).[104] After identifying a trimeric assembly of HLA-Fab complexes, the assembly was used to find three additional copies of the assembly, yielding an asymmetric unit that contained 12 copies of HLA and 12 copies of the Fab. Models were iteratively rebuilt with COOT[105] and refined with phenix.refine.[106] Data collection and refinement statistics are provided. Though 12 copies of each protein could be identified in the asymmetric unit, domain α3 for some HLA and β2m had degenerate density following refinement due to high B-factors, likely a result of crystal packing, and were thus removed from the final model. After removal, electron

density from Fo-Fc difference maps showed density for the additional domains, confirming their presence in the lattice. The final model contains six copies of the complete HLA-Fab complex, six additional copies of the Fab, three copies of the HLA domain with α3 removed, and two copies of β2m. Structure factors and final refined coordinates were deposited in the PDB (8T7R).

CryoEM grid preparation and data collection. The L02/M07/A*01:01 complex was concentrated to 3.04 mg/mL in PBS. Grids for electron cryo-microscopy were prepared by placing 3mL of solution on a 2/1-3T C-flat grid (R2/1 thick carbon, 300 mesh, Protochips), which was plunged into liquid ethane with a Mark IV Vitrobot. The grids were clipped and transferred to a G3 FEI-Krios electron microscope (La Jolla Institute for Immunology), which is equipped with a Gatan Bio-quantum energy filter with a 20eV slit. Images were detected on a K3 camera in counting mode (not super-resolution). The electron beam intensity was ~15e^-/pixel*s and 50 fractions were collected for every image, giving the specimen 1e/A*A*frame. The beam size was 900nm, which allowed for collection of 6 images per hole in the sample.

CryoEM data processing, model building and refinement. CryoEM data processing was performed by the UAB CryoEM Facility. The images were pre-processed with Warp,[107] where the images were corrected for movement, CTF parameters were estimated, and an initial set of particles was picked. CryoSPARC v4 was used for data processing.[108] Pre-processing was repeated using patch motion correction and CTF estimation. From 14,572 exposures, blob picking and 2D classification yielded 93,263 preliminary particles for Topaz training (Figure S6A).[109] Topaz autopicked 804,662 particles, which were initially downsampled to 2.64Å/pix and cleaned via 2D classification. The remaining particles were classified into four classes using ab-initio 3D reconstruction. This was done in quadruplicate for three iterations, keeping any particles that contributed to a good class. Finally, 252,746 particles from 3D classes corresponding to the L02/M07/A*01:01 complex were kept. After reverting to the original 0.66 Å/pix particles, these were refined using non-uniform refinement to a resolution of 3.14Å (Figure S6B-C).[110] To initiate atomic model building, AA sequences were input to ColabFold via ChimeraX to generate AlphaFold predicted models.[111-113] M07 and L02 were differentiated based on AAs with bulky side chains present in either, but not both, which could be clearly identified in the reconstruction. AlphaFold initial models were rigid-body fitted to the reconstruction using ChimeraX and refined in real space using *Coot* (Figure S6D).[105] Phenix was used for global real-space refinement and model validation.[114]

Structural analyses. Properties of Fab/HLA binding interfaces were analyzed using UCSF ChimeraX.[112] Interacting residues at the Fab:HLA interface were identified using a heavy-atom (non-hydrogen atom) distance cutoff of ≤5 Å.[57] Epitopic residues were defined as those with an interatomic distance between a heavy atom in the Fab and a heavy atom in the HLA complex ≤5 Å or any residues in the HLA complex with solvent accessible surface area that was buried in the interface between the Fab and HLA-A*01:01. Hydrogen bonds were identified using UCSF ChimeraX hbond command with default criteria.[112]

Immunofluorescent histology of allograft specimens. After obtaining the transplant nephrectomy specimen, sections were embedded in Tissue-Tek O.C.T. Compound (Sakura) and frozen in liquid nitrogen. Tissue sectioning (6 µm) was performed on a cryostat (Leica CM1860), and sections were stained with three different panels of anti-human secondary antibodies, including CD21::FITC (Biolegend, clone Bu32), CD19::APC (BD, clone HIB19), CD21::FITC (Biolegend, clone Bu32), CD4::AF488 (Biolegend, clone OKT4), CD19::PE (Biolegend, clone HIB19), Ki67::APC (Biolegend, clone Ki-67), anti-Ig::AF488 (Southern Biotech, polyclonal), CD38::APC (Biolegend, clone HIT2), and DAPI. Images were acquired on a Nikon Eclipse Ti microscope with the eyepiece at 10x, mirror at 1x, and objective of 20x (for total 200x) or 40x (for total 400x). Images were exported at 300dpi as *.TIFF files. Originals are saved as *.ND2 files including metadata and exposure times. For Figures 1A-C, exposure times (in milliseconds) for each channel (DAPI, FITC, PE, APC) are listed: Figure 1A (500, 3000, 6000, 10000), Figure 1B (2000, 3000, 8000, 10000), Figure 1C left (60, 70, 1000, 600), Figure 1C right (250, 70, 1400, 800). The tonal range of RGB was reduced in Adobe Photoshop (Adobe Inc., San Jose, CA) to increase brightness and contrast, with settings uniformly applied across all images utilizing the same staining panel.

Clinical HLA typing by next-generation sequencing. HLA typing of both donor and recipient were performed by the UAB Histocompatibility Laboratory using its standard clinical assay for next-generation sequencing. Genomic DNA was extracted from peripheral blood samples using the Qiagen EZ1 DNA blood kit via the Buffy coat protocol. Library construction and enrichment were performed per manufacturer's protocols for the CareDx AlloSeq Tx 17 assay and libraries were run on the Illumina MiSeq. Propietary CareDx software, AlloSeq Assign, v1.0.3 (CareDX, Stockholm, Sweden) utilized references from the Immuno Polymorphism Database-ImMunoGeneTics project/HLA Database (IPD-IMGT/HLA database) v3.47.0.0 to make allele assignments for all HLA Class I and Class II loci.

Analysis of HLA residue properties. For consistency across structural models, a previously reported structure of HLA A*01:01 (PDB: 3BO8)[115] was used for calculations of HLA A*01:01 residue solvent accessibility in the unbound state by PISA[116] and Ellipro scores for residue protrusion.[117] Physicochemical mismatches were compared as previously described[118] for hydrophilicity and electrostatic mismatch, and AA substitution similarity scores were used for dissimilarity calculation.[119] To calculate residue distances from the center of the peptide-binding groove (PBG), the previously reported HLA A*01:01 (PDB: 3BO8)[115] structure was used and the center of the PBG was defined as the α-carbon of the 5th residue (T5) in the peptide nonamer (EADPTGHSY) presented within the PBG. Distances were then calculated between the peptide T5 residue α-carbon and the α-carbon of each AA in A*01:01 using UCSF ChimeraX.[112]

A*01:01-typed T cell binding assays. Purified, cryopreserved human CD3+ T cells that were HLA-typed as A*01:01 / A*01:01 homozygous were obtained from StemCell (Kent, WA). T cells were thawed and aliquoted to 5,000 cells/well and incubated for 15 min with the single IgG1 A*01:01 rmAbs (E07, L02, M07), W6/32 (anti-HLA

positive control, ThermoFisher) or purified human polyclonal Abs (SouthernBiotech) diluted in PBS. Following incubation and washing, cells were incubated with anti-IgG::AF488 in PBS with 1% BSA for 15 min. Cells were washed, resuspended in PBS and analyzed on a Cytoflex flow cytometer (Beckman Coulter Life Sciences). Data were analyzed in FlowJo v10.8.1 (BD) and the gMFI of binding by the anti-HLA Abs to the T cells was calculated.

Statistical analyses. All statistical comparisons were performed in Prism (GraphPad Software). Comparisons of an observed distribution with the expected distribution were performed using the binomial test and the confidence interval of the proportion was calculated using the hybrid Wilson/Brown method in Prism. Following confirmation of distribution normality by the Shapiro-Wilk test, comparisons of group means was made using an unpaired t-test. If distributions were assessed to be non-normal, group ranks were compared via the Mann-Whitney test. Spearman correlations were used to assess association between two nonparametric variables.

Statistical analyses. Hierarchical clustering, heatmap plots, and other visualizations were created using R v4.2.0 (R Core Team 2022),[120] Matlab (R2020a, The Mathworks Inc., Natick, MA), UCSF ChimeraX v1.5,[112] Cytoscape v3.8.2,[90] FlowJo v10.8.1 (BD, Franklin Lakes, NJ), Prism v9.5.1 (GraphPad Software, LLC., Boston, MA), or Biorender.com (Toronto, Canada).

Data and Code Availability. IgV_H sequencing data has been deposited on GEO (GSE235533). CryoEM data has been deposited in PDB, EMDB, and EMPIAR (8T6M, EMD-41072, EMPIAR-11591). X-ray crystallography data has been deposited in PDB (8T7R). Proteomics data is deposited in ProteomXchange (PXD043144). Original code for the plasma proteomics analysis is deposited on Zenodo (10.5281/zenodo.8039145).

REFERENCES

1. Sellares, J., de Freitas, D.G., Mengel, M., Reeve, J., Einecke, G., Sis, B., Hidalgo, L.G., Famulski, K., Matas, A., and Halloran, P.F. (2012). Understanding the causes of kidney transplant failure: the dominant role of antibody-mediated rejection and nonadherence. Am J Transplant *12*, 388-399. 10.1111/j.1600-6143.2011.03840.x.
2. Gaston, R.S., Cecka, J.M., Kasiske, B.L., Fieberg, A.M., Leduc, R., Cosio, F.C., Gourishankar, S., Grande, J., Halloran, P., Hunsicker, L., et al. (2010). Evidence for antibody-mediated injury as a major determinant of late kidney allograft failure. Transplantation *90*, 68-74. 10.1097/TP.0b013e3181e065de.
3. Einecke, G., Sis, B., Reeve, J., Mengel, M., Campbell, P.M., Hidalgo, L.G., Kaplan, B., and Halloran, P.F. (2009). Antibody-mediated microcirculation injury is the major cause of late kidney transplant failure. Am J Transplant *9*, 2520-2531. 10.1111/j.1600-6143.2009.02799.x.
4. Everly, M.J., Rebellato, L.M., Haisch, C.E., Ozawa, M., Parker, K., Briley, K.P., Catrou, P.G., Bolin, P., Kendrick, W.T., Kendrick, S.A., et al. (2013). Incidence and impact of de novo donor-specific alloantibody in primary renal allografts. Transplantation *95*, 410-417. 10.1097/TP.0b013e31827d62e3.
5. Wiebe, C., Gibson, I.W., Blydt-Hansen, T.D., Karpinski, M., Ho, J., Storsley, L.J., Goldberg, A., Birk, P.E., Rush, D.N., and Nickerson, P.W. (2012). Evolution and clinical pathologic correlations of de novo donor-specific HLA antibody post kidney transplant. Am J Transplant *12*, 1157-1167. 10.1111/j.1600-6143.2012.04013.x.
6. Rao, P.S., Schaubel, D.E., Jia, X., Li, S., Port, F.K., and Saran, R. (2007). Survival on dialysis post-kidney transplant failure: results from the Scientific Registry of Transplant Recipients. Am J Kidney Dis *49*, 294-300. 10.1053/j.ajkd.2006.11.022.
7. Wehmeier, C., Karahan, G.E., Krop, J., de Vaal, Y., Langerak-Langerak, J., Binet, I., Schaub, S., Roelen, D.L., Claas, F.H.J., Heidt, S., and and the Swiss Transplant Cohort, S. (2019). Donor-specific B cell memory in alloimmunized kidney transplant recipients - first clinical application of a novel method. Transplantation. 10.1097/TP.0000000000002909.
8. Lucia, M., Luque, S., Crespo, E., Melilli, E., Cruzado, J.M., Martorell, J., Jarque, M., Gil-Vernet, S., Manonelles, A., Grinyo, J.M., and Bestard, O. (2015). Preformed circulating HLA-specific memory B cells predict high risk of humoral rejection in kidney transplantation. Kidney Int *88*, 874-887. 10.1038/ki.2015.205.
9. Luque, S., Lucia, M., Melilli, E., Lefaucheur, C., Crespo, M., Loupy, A., Bernal-Casas, D., Goma, M., Jarque, M., Crespo, E., et al. (2019). Value of monitoring circulating donor-reactive memory B cells to characterize antibody-mediated rejection after kidney transplantation. Am J Transplant *19*, 368-380. 10.1111/ajt.15055.
10. Zeng, Q., Ng, Y.H., Singh, T., Jiang, K., Sheriff, K.A., Ippolito, R., Zahalka, S., Li, Q., Randhawa, P., Hoffman, R.A., et al. (2014). B cells mediate chronic allograft rejection independently of antibody production. J Clin Invest *124*, 1052-1056. 10.1172/JCI70084.
11. Schinstock, C.A., Mannon, R.B., Budde, K., Chong, A.S., Haas, M., Knechtle, S., Lefaucheur, C., Montgomery, R.A., Nickerson, P., Tullius, S.G., et al. (2020). Recommended Treatment for Antibody-mediated Rejection After Kidney Transplantation: The 2019 Expert Consensus From the Transplantion Society Working Group. Transplantation *104*, 911-922. 10.1097/TP.0000000000003095.
12. Mesin, L., Ersching, J., and Victora, G.D. (2016). Germinal Center B Cell Dynamics. Immunity *45*, 471-482. 10.1016/j.immuni.2016.09.001.
13. Gitlin, A.D., Shulman, Z., and Nussenzweig, M.C. (2014). Clonal selection in the germinal centre by regulated proliferation and hypermutation. Nature *509*, 637-640. 10.1038/nature13300.
14. Matz, H.C., McIntire, K.M., and Ellebedy, A.H. (2023). Persistent germinal center responses: slow-growing trees bear the best fruits. Curr Opin Immunol *83*, 102332. 10.1016/j.coi.2023.102332.
15. Ramaraj, T., Angel, T., Dratz, E.A., Jesaitis, A.J., and Mumey, B. (2012). Antigen-antibody interface properties: composition, residue interactions, and features of 53 non-redundant structures. Biochim Biophys Acta *1824*, 520-532. 10.1016/j.bbapap.2011.12.007.
16. Han, J., Schmitz, A.J., Richey, S.T., Dai, Y.N., Turner, H.L., Mohammed, B.M., Fremont, D.H., Ellebedy, A.H., and Ward, A.B. (2021). Polyclonal epitope mapping reveals temporal dynamics and diversity of human antibody responses to H5N1 vaccination. Cell Rep *34*, 108682. 10.1016/j.celrep.2020.108682.

17. Abbott, R.K., and Crotty, S. (2020). Factors in B cell competition and immunodominance. Immunol Rev *296*, 120-131. 10.1111/imr.12861.
18. Veneziano, R., Moyer, T.J., Stone, M.B., Wamhoff, E.C., Read, B.J., Mukherjee, S., Shepherd, T.R., Das, J., Schief, W.R., Irvine, D.J., and Bathe, M. (2020). Role of nanoscale antigen organization on B-cell activation probed using DNA origami. Nat Nanotechnol *15*, 716-723. 10.1038/s41565-020-0719-0.
19. Lu, S., Xie, X.X., Zhao, L., Wang, B., Zhu, J., Yang, T.R., Yang, G.W., Ji, M., Lv, C.P., Xue, J., et al. (2021). The immunodominant and neutralization linear epitopes for SARS-CoV-2. Cell Rep *34*, 108666. 10.1016/j.celrep.2020.108666.
20. Angeletti, D., Gibbs, J.S., Angel, M., Kosik, I., Hickman, H.D., Frank, G.M., Das, S.R., Wheatley, A.K., Prabhakaran, M., Leggat, D.J., et al. (2017). Defining B cell immunodominance to viruses. Nat Immunol *18*, 456-463. 10.1038/ni.3680.
21. Merrill, J.P., Murray, J.E., Harrison, J.H., and Guild, W.R. (1956). Successful homotransplantation of the human kidney between identical twins. J Am Med Assoc *160*, 277-282. 10.1001/jama.1956.02960390027008.
22. Senev, A., Coemans, M., Lerut, E., Van Sandt, V., Kerkhofs, J., Daniels, L., Driessche, M.V., Compernolle, V., Sprangers, B., Van Loon, E., et al. (2020). Eplet Mismatch Load and De Novo Occurrence of Donor-Specific Anti-HLA Antibodies, Rejection, and Graft Failure after Kidney Transplantation: An Observational Cohort Study. J Am Soc Nephrol *31*, 2193-2204. 10.1681/ASN.2020010019.
23. Bezstarosti, S., Kramer, C.S.M., Claas, F.H.J., de Fijter, J.W., Reinders, M.E.J., and Heidt, S. (2022). Implementation of molecular matching in transplantation requires further characterization of both immunogenicity and antigenicity of individual HLA epitopes. Hum Immunol *83*, 256-263. 10.1016/j.humimm.2021.12.002.
24. Honger, G., Niemann, M., Schawalder, L., Jones, J., van Heck, M.R., van de Pasch, L.A.L., Vendelbosch, S., Rozemuller, E.H., Hosli, I., Blumel, S., and Schaub, S. (2020). Toward defining the immunogenicity of HLA epitopes: Impact of HLA class I eplets on antibody formation during pregnancy. HLA. 10.1111/tan.14054.
25. Tambur, A.R., and Das, R. (2022). Can We Use Eplets (or Molecular) Mismatch Load Analysis to Improve Organ Allocation? The Hope and the Hype. Transplantation. 10.1097/TP.0000000000004307.
26. Kramer, C.S.M., Franke-van Dijk, M.E.I., Bakker, K.H., Uyar-Mercankaya, M., Karahan, G.E., Roelen, D.L., Claas, F.H.J., and Heidt, S. (2020). Generation and reactivity analysis of human recombinant monoclonal antibodies directed against epitopes on HLA-DR. Am J Transplant *20*, 3341-3353. 10.1111/ajt.15950.
27. Louis, K., Bailly, E., Macedo, C., Lau, L., Ramaswami, B., Chang, A., Chandran, U., Landsittel, D., Gu, X., Chalasani, G., et al. (2021). T-bet+CD27+CD21- B cells poised for plasma cell differentiation during antibody-mediated rejection of kidney transplants. JCI Insight *6*. 10.1172/jci.insight.148881.
28. Lee, Y.H., Sato, Y., Saito, M., Fukuma, S., Saito, M., Yamamoto, S., Komatsuda, A., Fujiyama, N., Satoh, S., Lee, S.H., et al. (2022). Advanced Tertiary Lymphoid Tissues in Protocol Biopsies are Associated with Progressive Graft Dysfunction in Kidney Transplant Recipients. J Am Soc Nephrol *33*, 186-200. 10.1681/ASN.2021050715.
29. Liarski, V.M., Kaverina, N., Chang, A., Brandt, D., Yanez, D., Talasnik, L., Carlesso, G., Herbst, R., Utset, T.O., Labno, C., et al. (2014). Cell distance mapping identifies functional T follicular helper cells in inflamed human renal tissue. Sci Transl Med *6*, 230ra246. 10.1126/scitranslmed.3008146.
30. Maccari, G., Robinson, J., Ballingall, K., Guethlein, L.A., Grimholt, U., Kaufman, J., Ho, C.S., de Groot, N.G., Flicek, P., Bontrop, R.E., et al. (2017). IPD-MHC 2.0: an improved inter-species database for the study of the major histocompatibility complex. Nucleic Acids Res *45*, D860-D864. 10.1093/nar/gkw1050.
31. Houghton, A.N. (1994). Cancer antigens: immune recognition of self and altered self. J Exp Med *180*, 1-4. 10.1084/jem.180.1.1.
32. Karlsen, A.E., and Dyrberg, T. (1998). Molecular mimicry between non-self, modified self and self in autoimmunity. Semin Immunol *10*, 25-34. 10.1006/smim.1997.0102.
33. Asano, Y., Daccache, J., Jain, D., Ko, K., Kinloch, A., Veselits, M., Wolfgeher, D., Chang, A., Josephson, M., Cunningham, P., et al. (2021). Innate-like self-reactive B cells infiltrate human renal allografts during transplant rejection. Nat Commun *12*, 4372. 10.1038/s41467-021-24615-6.

34. Clotet-Freixas, S., Kotlyar, M., McEvoy, C.M., Pastrello, C., Rodriguez-Ramirez, S., Farkona, S., Cardinal, H., Dieude, M., Hebert, M.J., Li, Y., et al. (2021). Increased Autoantibodies Against Ro/SS-A, CENP-B, and La/SS-B in Patients With Kidney Allograft Antibody-mediated Rejection. Transplant Direct *7*, e768. 10.1097/TXD.0000000000001215.
35. Saini, D., Weber, J., Ramachandran, S., Phelan, D., Tiriveedhi, V., Liu, M., Steward, N., Aloush, A., Hachem, R., Trulock, E., et al. (2011). Alloimmunity-induced autoimmunity as a potential mechanism in the pathogenesis of chronic rejection of human lung allografts. J Heart Lung Transplant *30*, 624-631. 10.1016/j.healun.2011.01.708.
36. Duquesnoy, R.J. (2006). A structurally based approach to determine HLA compatibility at the humoral immune level. Hum Immunol *67*, 847-862. 10.1016/j.humimm.2006.08.001.
37. Gu, Y., Wong, Y.H., Liew, C.W., Chan, C.E.Z., Murali, T.M., Yap, J., Too, C.T., Purushotorman, K., Hamidinia, M., El Sahili, A., et al. (2019). Defining the structural basis for human alloantibody binding to human leukocyte antigen allele HLA-A*11:01. Nat Commun *10*, 893. 10.1038/s41467-019-08790-1.
38. Organ Procurement and Transplantation Network (2023). OPTN Policies. https://optn.transplant.hrsa.gov/media/eavh5bf3/optn_policies.pdf.
39. Senev, A., Lerut, E., Coemans, M., Callemeyn, J., Copley, H.C., Claas, F., Koshy, P., Kosmoliaptsis, V., Kuypers, D., Sprangers, B., et al. (2022). Association of HLA Mismatches and Histology Suggestive of Antibody-Mediated Injury in the Absence of Donor-Specific Anti-HLA Antibodies. Clin J Am Soc Nephrol *17*, 1204-1215. 10.2215/CJN.00570122.
40. Do Nguyen, H.T., Wong, G., Chapman, J.R., McDonald, S.P., Coates, P.T., Watson, N., Russ, G.R., D'Orsogna, L., and Lim, W.H. (2016). The Association Between Broad Antigen HLA Mismatches, Eplet HLA Mismatches and Acute Rejection After Kidney Transplantation. Transplant Direct *2*, e120. 10.1097/TXD.0000000000000632.
41. Snanoudj, R., Kamar, N., Cassuto, E., Caillard, S., Metzger, M., Merville, P., Thierry, A., Jollet, I., Grimbert, P., Anglicheau, D., et al. (2019). Epitope load identifies kidney transplant recipients at risk of allosensitization following minimization of immunosuppression. Kidney Int *95*, 1471-1485. 10.1016/j.kint.2018.12.029.
42. Tambur, A.R., Kosmoliaptsis, V., Claas, F.H.J., Mannon, R.B., Nickerson, P., and Naesens, M. (2021). Significance of HLA-DQ in kidney transplantation: time to reevaluate human leukocyte antigen-matching priorities to improve transplant outcomes? An expert review and recommendations. Kidney Int *100*, 1012-1022. 10.1016/j.kint.2021.06.026.
43. Jackson, K.R., and Segev, D.L. (2022). Rethinking incompatibility in kidney transplantation. Am J Transplant *22*, 1031-1036. 10.1111/ajt.16826.
44. Tambur, A.R., Campbell, P., Chong, A.S., Feng, S., Ford, M.L., Gebel, H., Gill, R.G., Kelsoe, G., Kosmoliaptsis, V., Mannon, R.B., et al. (2020). Sensitization in transplantation: Assessment of risk (STAR) 2019 Working Group Meeting Report. Am J Transplant *20*, 2652-2668. 10.1111/ajt.15937.
45. National Kidney Registry. Finding the Best Kidney Transplant Match. https://www.kidneyregistry.org/for-patients/finding-the-best-kidney-match/.
46. Ellebedy, A.H., Jackson, K.J., Kissick, H.T., Nakaya, H.I., Davis, C.W., Roskin, K.M., McElroy, A.K., Oshansky, C.M., Elbein, R., Thomas, S., et al. (2016). Defining antigen-specific plasmablast and memory B cell subsets in human blood after viral infection or vaccination. Nat Immunol *17*, 1226-1234. 10.1038/ni.3533.
47. Turner, J.S., Zhou, J.Q., Han, J., Schmitz, A.J., Rizk, A.A., Alsoussi, W.B., Lei, T., Amor, M., McIntire, K.M., Meade, P., et al. (2020). Human germinal centres engage memory and naive B cells after influenza vaccination. Nature *586*, 127-132. 10.1038/s41586-020-2711-0.
48. Chang, A., Henderson, S.G., Brandt, D., Liu, N., Guttikonda, R., Hsieh, C., Kaverina, N., Utset, T.O., Meehan, S.M., Quigg, R.J., et al. (2011). In situ B cell-mediated immune responses and tubulointerstitial inflammation in human lupus nephritis. J Immunol *186*, 1849-1860. 10.4049/jimmunol.1001983.
49. Tipton, C.M., Fucile, C.F., Darce, J., Chida, A., Ichikawa, T., Gregoretti, I., Schieferl, S., Hom, J., Jenks, S., Feldman, R.J., et al. (2015). Diversity, cellular origin and autoreactivity of antibody-secreting cell population expansions in acute systemic lupus erythematosus. Nat Immunol *16*, 755-765. 10.1038/ni.3175.

50. Cheng, J., Torkamani, A., Grover, R.K., Jones, T.M., Ruiz, D.I., Schork, N.J., Quigley, M.M., Hall, F.W., Salomon, D.R., and Lerner, R.A. (2011). Ectopic B-cell clusters that infiltrate transplanted human kidneys are clonal. Proc Natl Acad Sci U S A *108*, 5560-5565. 10.1073/pnas.1101148108.
51. Tsai, E.W., Rianthavorn, P., Gjertson, D.W., Wallace, W.D., Reed, E.F., and Ettenger, R.B. (2006). CD20+ lymphocytes in renal allografts are associated with poor graft survival in pediatric patients. Transplantation *82*, 1769-1773. 10.1097/01.tp.0000250572.46679.45.
52. Hippen, B.E., DeMattos, A., Cook, W.J., Kew, C.E., 2nd, and Gaston, R.S. (2005). Association of CD20+ infiltrates with poorer clinical outcomes in acute cellular rejection of renal allografts. Am J Transplant *5*, 2248-2252. 10.1111/j.1600-6143.2005.01009.x.
53. Kim, W., Zhou, J.Q., Horvath, S.C., Schmitz, A.J., Sturtz, A.J., Lei, T., Liu, Z., Kalaidina, E., Thapa, M., Alsoussi, W.B., et al. (2022). Germinal centre-driven maturation of B cell response to mRNA vaccination. Nature *604*, 141-145. 10.1038/s41586-022-04527-1.
54. Lee, J.H., Sutton, H.J., Cottrell, C.A., Phung, I., Ozorowski, G., Sewall, L.M., Nedellec, R., Nakao, C., Silva, M., Richey, S.T., et al. (2022). Long-primed germinal centres with enduring affinity maturation and clonal migration. Nature *609*, 998-1004. 10.1038/s41586-022-05216-9.
55. Lavinder, J.J., Wine, Y., Giesecke, C., Ippolito, G.C., Horton, A.P., Lungu, O.I., Hoi, K.H., DeKosky, B.J., Murrin, E.M., Wirth, M.M., et al. (2014). Identification and characterization of the constituent human serum antibodies elicited by vaccination. Proc Natl Acad Sci U S A *111*, 2259-2264. 10.1073/pnas.1317793111.
56. Purtha, W.E., Tedder, T.F., Johnson, S., Bhattacharya, D., and Diamond, M.S. (2011). Memory B cells, but not long-lived plasma cells, possess antigen specificities for viral escape mutants. J Exp Med *208*, 2599-2606. 10.1084/jem.20110740.
57. Akbar, R., Robert, P.A., Pavlovic, M., Jeliazkov, J.R., Snapkov, I., Slabodkin, A., Weber, C.R., Scheffer, L., Miho, E., Haff, I.H., et al. (2021). A compact vocabulary of paratope-epitope interactions enables predictability of antibody-antigen binding. Cell Rep *34*, 108856. 10.1016/j.celrep.2021.108856.
58. MacRaild, C.A., Richards, J.S., Anders, R.F., and Norton, R.S. (2016). Antibody Recognition of Disordered Antigens. Structure *24*, 148-157. 10.1016/j.str.2015.10.028.
59. Kosmoliaptsis, V., Chaudhry, A.N., Sharples, L.D., Halsall, D.J., Dafforn, T.R., Bradley, J.A., and Taylor, C.J. (2009). Predicting HLA class I alloantigen immunogenicity from the number and physiochemical properties of amino acid polymorphisms. Transplantation *88*, 791-798. 10.1097/TP.0b013e3181b4a9ff.
60. Kosmoliaptsis, V., Sharples, L.D., Chaudhry, A.N., Halsall, D.J., Bradley, J.A., and Taylor, C.J. (2011). Predicting HLA class II alloantigen immunogenicity from the number and physiochemical properties of amino acid polymorphisms. Transplantation *91*, 183-190. 10.1097/TP.0b013e3181ffff99.
61. Duquesnoy, R.J., and Marrari, M. (2017). Usefulness of the ElliPro epitope predictor program in defining the repertoire of HLA-ABC eplets. Hum Immunol *78*, 481-488. 10.1016/j.humimm.2017.03.005.
62. Moyer, T.J., Kato, Y., Abraham, W., Chang, J.Y.H., Kulp, D.W., Watson, N., Turner, H.L., Menis, S., Abbott, R.K., Bhiman, J.N., et al. (2020). Engineered immunogen binding to alum adjuvant enhances humoral immunity. Nat Med *26*, 430-440. 10.1038/s41591-020-0753-3.
63. Bjorkman, P.J., and Parham, P. (1990). Structure, function, and diversity of class I major histocompatibility complex molecules. Annu Rev Biochem *59*, 253-288. 10.1146/annurev.bi.59.070190.001345.
64. Chen, J., Sawyer, N., and Regan, L. (2013). Protein-protein interactions: general trends in the relationship between binding affinity and interfacial buried surface area. Protein Sci *22*, 510-515. 10.1002/pro.2230.
65. Bezstarosti, S., Bakker, K.H., Kramer, C.S.M., de Fijter, J.W., Reinders, M.E.J., Mulder, A., Claas, F.H.J., and Heidt, S. (2021). A Comprehensive Evaluation of the Antibody-Verified Status of Eplets Listed in the HLA Epitope Registry. Front Immunol *12*, 800946. 10.3389/fimmu.2021.800946.
66. Xu, J.L., and Davis, M.M. (2000). Diversity in the CDR3 region of V(H) is sufficient for most antibody specificities. Immunity *13*, 37-45. 10.1016/s1074-7613(00)00006-6.
67. Duquesnoy, R.J., Marrari, M., Mulder, A., Sousa, L.C., da Silva, A.S., and do Monte, S.J. (2014). First report on the antibody verification of HLA-ABC epitopes recorded in the website-based HLA Epitope Registry. Tissue Antigens *83*, 391-400. 10.1111/tan.12341.
68. Krause, J.C., Tsibane, T., Tumpey, T.M., Huffman, C.J., Briney, B.S., Smith, S.A., Basler, C.F., and Crowe, J.E., Jr. (2011). Epitope-specific human influenza antibody repertoires diversify by B cell

intraclonal sequence divergence and interclonal convergence. J Immunol *187*, 3704-3711. 10.4049/jimmunol.1101823.
69. Mulder, A., Eijsink, C., Kardol, M.J., Franke-van Dijk, M.E., van der Burg, S.H., Kester, M., Doxiadis, II, and Claas, F.H. (2003). Identification, isolation, and culture of HLA-A2-specific B lymphocytes using MHC class I tetramers. J Immunol *171*, 6599-6603. 10.4049/jimmunol.171.12.6599.
70. Zhang, H., Cavazzoni, C.B., Hanson, B.L., Bechu, E.D., Podesta, M.A., Azzi, J., Blazar, B.R., Chong, A.S., Kreisel, D., Alessandrini, A., and Sage, P.T. (2023). Transcriptionally Distinct B Cells Infiltrate Allografts After Kidney Transplantation. Transplantation *107*, e47-e57. 10.1097/TP.0000000000004398.
71. Ferdman, J., Porcheray, F., Gao, B., Moore, C., DeVito, J., Dougherty, S., Thomas, M.V., Farkash, E.A., Elias, N., Kawai, T., et al. (2014). Expansion and somatic hypermutation of B-cell clones in rejected human kidney grafts. Transplantation *98*, 766-772. 10.1097/TP.0000000000000124.
72. Porcheray, F., DeVito, J., Helou, Y., Dargon, I., Fraser, J.W., Nobecourt, P., Ferdman, J., Germana, S., Girouard, T.C., Kawai, T., et al. (2012). Expansion of polyreactive B cells cross-reactive to HLA and self in the blood of a patient with kidney graft rejection. Am J Transplant *12*, 2088-2097. 10.1111/j.1600-6143.2012.04053.x.
73. Mazor, R.D., Nathan, N., Gilboa, A., Stoler-Barak, L., Moss, L., Solomonov, I., Hanuna, A., Divinsky, Y., Shmueli, M.D., Hezroni, H., et al. (2022). Tumor-reactive antibodies evolve from non-binding and autoreactive precursors. Cell *185*, 1208-1222 e1221. 10.1016/j.cell.2022.02.012.
74. Kueht, M., Jindra, P., Stevenson, H.L., Galvan, T.N., Murthy, B., Goss, J., Anton, J., Abbas, R., and Cusick, M.F. (2021). Intra-operative kinetics of anti-HLA antibody in simultaneous liver-kidney transplantation. Mol Genet Metab Rep *26*, 100705. 10.1016/j.ymgmr.2020.100705.
75. Wiebe, C., Pochinco, D., Blydt-Hansen, T.D., Ho, J., Birk, P.E., Karpinski, M., Goldberg, A., Storsley, L.J., Gibson, I.W., Rush, D.N., and Nickerson, P.W. (2013). Class II HLA epitope matching-A strategy to minimize de novo donor-specific antibody development and improve outcomes. Am J Transplant *13*, 3114-3122. 10.1111/ajt.12478.
76. Duquesnoy, R.J. (2016). Reflections on HLA Epitope-Based Matching for Transplantation. Front Immunol *7*, 469. 10.3389/fimmu.2016.00469.
77. Wiebe, C., Kosmoliaptsis, V., Pochinco, D., Gibson, I.W., Ho, J., Birk, P.E., Goldberg, A., Karpinski, M., Shaw, J., Rush, D.N., and Nickerson, P.W. (2019). HLA-DR/DQ molecular mismatch: A prognostic biomarker for primary alloimmunity. Am J Transplant *19*, 1708-1719. 10.1111/ajt.15177.
78. Sapir-Pichhadze, R., Tinckam, K., Quach, K., Logan, A.G., Laupacis, A., John, R., Beyene, J., and Kim, S.J. (2015). HLA-DR and -DQ eplet mismatches and transplant glomerulopathy: a nested case-control study. Am J Transplant *15*, 137-148. 10.1111/ajt.12968.
79. Wiebe, C., Kosmoliaptsis, V., Pochinco, D., Taylor, C.J., and Nickerson, P. (2018). A Comparison of HLA Molecular Mismatch Methods to Determine HLA Immunogenicity. Transplantation *102*, 1338-1343. 10.1097/TP.0000000000002117.
80. Stave, J.W., and Lindpaintner, K. (2013). Antibody and antigen contact residues define epitope and paratope size and structure. J Immunol *191*, 1428-1435. 10.4049/jimmunol.1203198.
81. Bekbolsynov, D., Mierzejewska, B., Borucka, J., Liwski, R.S., Greenshields, A.L., Breidenbach, J., Gehring, B., Leonard-Murali, S., Khuder, S.A., Rees, M., et al. (2020). Low Hydrophobic Mismatch Scores Calculated for HLA-A/B/DR/DQ Loci Improve Kidney Allograft Survival. Front Immunol *11*, 580752. 10.3389/fimmu.2020.580752.
82. Garboczi, D.N., Ghosh, P., Utz, U., Fan, Q.R., Biddison, W.E., and Wiley, D.C. (1996). Structure of the complex between human T-cell receptor, viral peptide and HLA-A2. Nature *384*, 134-141. 10.1038/384134a0.
83. Boyington, J.C., Motyka, S.A., Schuck, P., Brooks, A.G., and Sun, P.D. (2000). Crystal structure of an NK cell immunoglobulin-like receptor in complex with its class I MHC ligand. Nature *405*, 537-543. 10.1038/35014520.
84. McCarthy, K.R., Watanabe, A., Kuraoka, M., Do, K.T., McGee, C.E., Sempowski, G.D., Kepler, T.B., Schmidt, A.G., Kelsoe, G., and Harrison, S.C. (2018). Memory B Cells that Cross-React with Group 1 and Group 2 Influenza A Viruses Are Abundant in Adult Human Repertoires. Immunity *48*, 174-184 e179. 10.1016/j.immuni.2017.12.009.

85. Zhang, J., Jacobi, A.M., Wang, T., Berlin, R., Volpe, B.T., and Diamond, B. (2009). Polyreactive autoantibodies in systemic lupus erythematosus have pathogenic potential. J Autoimmun *33*, 270-274. 10.1016/j.jaut.2009.03.011.
86. Brown, J.H., Jardetzky, T.S., Gorga, J.C., Stern, L.J., Urban, R.G., Strominger, J.L., and Wiley, D.C. (1993). Three-dimensional structure of the human class II histocompatibility antigen HLA-DR1. Nature *364*, 33-39. 10.1038/364033a0.
87. Nellore, A., Zumaquero, E., Scharer, C.D., Fucile, C.F., Tipton, C.M., King, R.G., Mi, T., Mousseau, B., Bradley, J.E., Zhou, F., et al. (2023). A transcriptionally distinct subset of influenza-specific effector memory B cells predicts long-lived antibody responses to vaccination in humans. Immunity. 10.1016/j.immuni.2023.03.001.
88. Lefranc, M.P., Giudicelli, V., Duroux, P., Jabado-Michaloud, J., Folch, G., Aouinti, S., Carillon, E., Duvergey, H., Houles, A., Paysan-Lafosse, T., et al. (2015). IMGT(R), the international ImMunoGeneTics information system(R) 25 years on. Nucleic Acids Res *43*, D413-422. 10.1093/nar/gku1056.
89. Felsenstein, J. (1993). PHYLIP (phylogeny inference package), version 3.5 c (Joseph Felsenstein.).
90. Shannon, P., Markiel, A., Ozier, O., Baliga, N.S., Wang, J.T., Ramage, D., Amin, N., Schwikowski, B., and Ideker, T. (2003). Cytoscape: a software environment for integrated models of biomolecular interaction networks. Genome Res *13*, 2498-2504. 10.1101/gr.1239303.
91. Ludwig, M.R., Kojima, K., Bowersock, G.J., Chen, D., Jhala, N.C., Buchsbaum, D.J., Grizzle, W.E., Klug, C.A., and Mobley, J.A. (2016). Surveying the serologic proteome in a tissue-specific kras(G12D) knockin mouse model of pancreatic cancer. Proteomics *16*, 516-531. 10.1002/pmic.201500133.
92. Perez-Riverol, Y., Bai, J., Bandla, C., Garcia-Seisdedos, D., Hewapathirana, S., Kamatchinathan, S., Kundu, D.J., Prakash, A., Frericks-Zipper, A., Eisenacher, M., et al. (2022). The PRIDE database resources in 2022: a hub for mass spectrometry-based proteomics evidences. Nucleic Acids Res *50*, D543-D552. 10.1093/nar/gkab1038.
93. Roll, G.R., Lunow-Luke, T., Braun, H.J., Buenaventura, O., Mallari, M., Stock, P.G., and Rajalingam, R. (2021). COVID-19 does not impact HLA antibody profile in a series of waitlisted renal transplant candidates. Hum Immunol *82*, 568-573. 10.1016/j.humimm.2021.04.002.
94. Woodruff, M.C., Ramonell, R.P., Haddad, N.S., Anam, F.A., Rudolph, M.E., Walker, T.A., Truong, A.D., Dixit, A.N., Han, J.E., Cabrera-Mora, M., et al. (2022). Dysregulated naive B cells and de novo autoreactivity in severe COVID-19. Nature *611*, 139-147. 10.1038/s41586-022-05273-0.
95. Altman, J.D., and Davis, M.M. (2003). MHC-peptide tetramers to visualize antigen-specific T cells. Curr Protoc Immunol *Chapter 17*, Unit 17 13. 10.1002/0471142735.im1703s53.
96. Chatzileontiadou, D.S.M., Szeto, C., Jayasinghe, D., and Gras, S. (2021). Protein purification and crystallization of HLA-A *02:01 in complex with SARS-CoV-2 peptides. STAR Protoc *2*, 100635. 10.1016/j.xpro.2021.100635.
97. Garboczi, D.N., Hung, D.T., and Wiley, D.C. (1992). HLA-A2-peptide complexes: refolding and crystallization of molecules expressed in Escherichia coli and complexed with single antigenic peptides. Proc Natl Acad Sci U S A *89*, 3429-3433. 10.1073/pnas.89.8.3429.
98. Ogonek, J., Verma, K., Schultze-Florey, C., Varanasi, P., Luther, S., Schweier, P., Kuhnau, W., Gohring, G., Dammann, E., Stadler, M., et al. (2017). Characterization of High-Avidity Cytomegalovirus-Specific T Cells with Differential Tetramer Binding Coappearing after Allogeneic Stem Cell Transplantation. J Immunol *199*, 792-805. 10.4049/jimmunol.1601992.
99. Otwinowski, Z., and Minor, W. (1997). Processing of X-ray diffraction data collected in oscillation mode. Methods Enzymol *276*, 307-326. 10.1016/S0076-6879(97)76066-X.
100. McCoy, A.J., Grosse-Kunstleve, R.W., Adams, P.D., Winn, M.D., Storoni, L.C., and Read, R.J. (2007). Phaser crystallographic software. J Appl Crystallogr *40*, 658-674. 10.1107/S0021889807021206.
101. Toor, J.S., Rao, A.A., McShan, A.C., Yarmarkovich, M., Nerli, S., Yamaguchi, K., Madejska, A.A., Nguyen, S., Tripathi, S., Maris, J.M., et al. (2018). A Recurrent Mutation in Anaplastic Lymphoma Kinase with Distinct Neoepitope Conformations. Front Immunol *9*, 99. 10.3389/fimmu.2018.00099.
102. Zhu, X., Turner, H.L., Lang, S., McBride, R., Bangaru, S., Gilchuk, I.M., Yu, W., Paulson, J.C., Crowe, J.E., Jr., Ward, A.B., and Wilson, I.A. (2019). Structural Basis of Protection against H7N9 Influenza Virus by Human Anti-N9 Neuraminidase Antibodies. Cell Host Microbe *26*, 729-738 e724. 10.1016/j.chom.2019.10.002.

103. Schmidt, A.G., Xu, H., Khan, A.R., O'Donnell, T., Khurana, S., King, L.R., Manischewitz, J., Golding, H., Suphaphiphat, P., Carfi, A., et al. (2013). Preconfiguration of the antigen-binding site during affinity maturation of a broadly neutralizing influenza virus antibody. Proc Natl Acad Sci U S A *110*, 264-269. 10.1073/pnas.1218256109.
104. Scally, S.W., McLeod, B., Bosch, A., Miura, K., Liang, Q., Carroll, S., Reponen, S., Nguyen, N., Giladi, E., Ramisch, S., et al. (2017). Molecular definition of multiple sites of antibody inhibition of malaria transmission-blocking vaccine antigen Pfs25. Nat Commun *8*, 1568. 10.1038/s41467-017-01924-3.
105. Emsley, P., Lohkamp, B., Scott, W.G., and Cowtan, K. (2010). Features and development of Coot. Acta Crystallogr D Biol Crystallogr *66*, 486-501. 10.1107/S0907444910007493.
106. Adams, P.D., Afonine, P.V., Bunkoczi, G., Chen, V.B., Davis, I.W., Echols, N., Headd, J.J., Hung, L.W., Kapral, G.J., Grosse-Kunstleve, R.W., et al. (2010). PHENIX: a comprehensive Python-based system for macromolecular structure solution. Acta Crystallogr D Biol Crystallogr *66*, 213-221. 10.1107/S0907444909052925.
107. Tegunov, D., and Cramer, P. (2019). Real-time cryo-electron microscopy data preprocessing with Warp. Nat Methods *16*, 1146-1152. 10.1038/s41592-019-0580-y.
108. Punjani, A., Rubinstein, J.L., Fleet, D.J., and Brubaker, M.A. (2017). cryoSPARC: algorithms for rapid unsupervised cryo-EM structure determination. Nat Methods *14*, 290-296. 10.1038/nmeth.4169.
109. Bepler, T., Morin, A., Rapp, M., Brasch, J., Shapiro, L., Noble, A.J., and Berger, B. (2019). Positive-unlabeled convolutional neural networks for particle picking in cryo-electron micrographs. Nat Methods *16*, 1153-1160. 10.1038/s41592-019-0575-8.
110. Punjani, A., Zhang, H., and Fleet, D.J. (2020). Non-uniform refinement: adaptive regularization improves single-particle cryo-EM reconstruction. Nat Methods *17*, 1214-1221. 10.1038/s41592-020-00990-8.
111. Mirdita, M., Schutze, K., Moriwaki, Y., Heo, L., Ovchinnikov, S., and Steinegger, M. (2022). ColabFold: making protein folding accessible to all. Nat Methods *19*, 679-682. 10.1038/s41592-022-01488-1.
112. Pettersen, E.F., Goddard, T.D., Huang, C.C., Meng, E.C., Couch, G.S., Croll, T.I., Morris, J.H., and Ferrin, T.E. (2021). UCSF ChimeraX: Structure visualization for researchers, educators, and developers. Protein Sci *30*, 70-82. 10.1002/pro.3943.
113. Jumper, J., Evans, R., Pritzel, A., Green, T., Figurnov, M., Ronneberger, O., Tunyasuvunakool, K., Bates, R., Zidek, A., Potapenko, A., et al. (2021). Highly accurate protein structure prediction with AlphaFold. Nature *596*, 583-589. 10.1038/s41586-021-03819-2.
114. Afonine, P.V., Poon, B.K., Read, R.J., Sobolev, O.V., Terwilliger, T.C., Urzhumtsev, A., and Adams, P.D. (2018). Real-space refinement in PHENIX for cryo-EM and crystallography. Acta Crystallogr D Struct Biol *74*, 531-544. 10.1107/S2059798318006551.
115. Kumar, P., Vahedi-Faridi, A., Saenger, W., Ziegler, A., and Uchanska-Ziegler, B. (2009). Conformational changes within the HLA-A1:MAGE-A1 complex induced by binding of a recombinant antibody fragment with TCR-like specificity. Protein Sci *18*, 37-49. 10.1002/pro.4.
116. Krissinel, E., and Henrick, K. (2007). Inference of macromolecular assemblies from crystalline state. J Mol Biol *372*, 774-797. 10.1016/j.jmb.2007.05.022.
117. Ponomarenko, J., Bui, H.H., Li, W., Fusseder, N., Bourne, P.E., Sette, A., and Peters, B. (2008). ElliPro: a new structure-based tool for the prediction of antibody epitopes. BMC Bioinformatics *9*, 514. 10.1186/1471-2105-9-514.
118. Kirk, A.D., Baldwin, W.M., Cascalho, M.I., Chong, A.S., Sykes, M., and West, L.J. (2007). American society of transplantation symposium on B cells in transplantation: harnessing humoral immunity from rodent models to clinical practice. Am J Transplant *7*, 1464-1470. 10.1111/j.1600-6143.2007.01815.x.
119. Risler, J.L., Delorme, M.O., Delacroix, H., and Henaut, A. (1988). Amino acid substitutions in structurally related proteins. A pattern recognition approach. Determination of a new and efficient scoring matrix. J Mol Biol *204*, 1019-1029. 10.1016/0022-2836(88)90058-7.
120. R Development Core Team (2010). R: A language and environment for statistical computing (R Foundation for Statistical Computing).
121. Roufosse, C., Simmonds, N., Clahsen-van Groningen, M., Haas, M., Henriksen, K.J., Horsfield, C., Loupy, A., Mengel, M., Perkowska-Ptasinska, A., Rabant, M., et al. (2018). A 2018 Reference Guide to the Banff Classification of Renal Allograft Pathology. Transplantation *102*, 1795-1814. 10.1097/TP.0000000000002366.

Figure 1

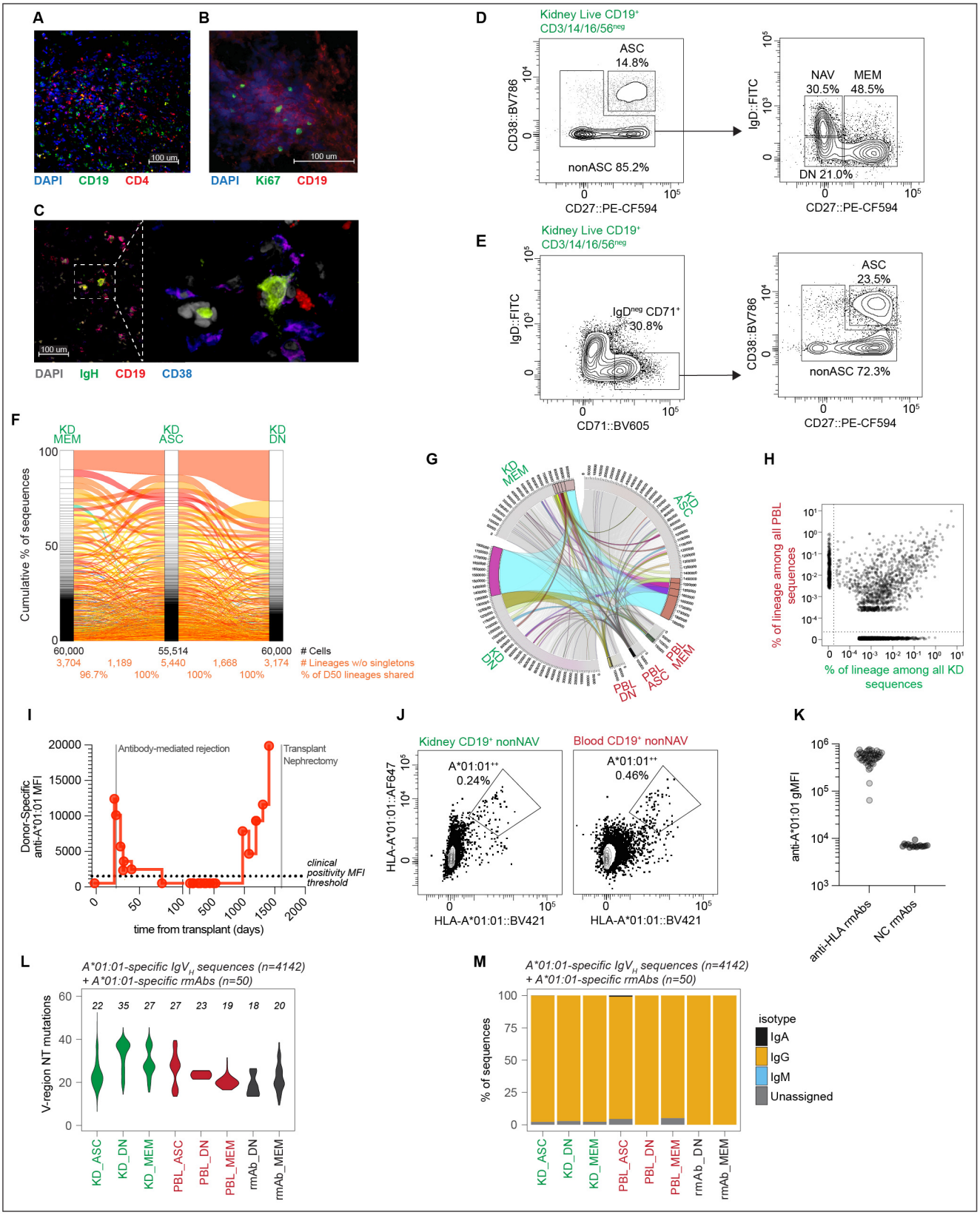
A
B
DAPI CD19 CD4
DAPI Ki67 CD19
100 um
C
DAPI IgH CD19 CD38
D
Kidney Live CD19+ CD3/14/16/56neg
ASC 14.8%
nonASC 85.2%
CD38::BV786
CD27::PE-CF594
NAV 30.5%
MEM 48.5%
DN 21.0%
IgD::FITC
E
Kidney Live CD19+ CD3/14/16/56neg
IgDneg CD71+ 30.8%
CD71::BV605
ASC 23.5%
nonASC 72.3%
F
KD MEM
KD ASC
KD DN
Cumulative % of seqeuences
60,000
55,514
60,000
Cells
3,704
1,189
5,440
1,668
3,174
Lineages w/o singletons
96.7%
100%
100%
100%
% of D50 lineages shared
G
H
% of lineage among all PBL sequences
% of lineage among all KD sequences
I
Antibody-mediated rejection
Transplant Nephrectomy
Donor-Specific anti-A*01:01 MFI
clinical positivity MFI threshold
time from transplant (days)
J
Kidney CD19+ nonNAV
Blood CD19+ nonNAV
A*01:01++ 0.24%
A*01:01++ 0.46%
HLA-A*01:01::AF647
HLA-A*01:01::BV421
K
anti-A*01:01 gMFI
anti-HLA rmAbs
NC rmAbs
L
A*01:01-specific IgVH sequences (n=4142)
+ A*01:01-specific rmAbs (n=50)
V-region NT mutations
22 35 27 27 23 19 18 20
KD_ASC
KD_DN
KD_MEM
PBL_ASC
PBL_DN
PBL_MEM
rmAb_DN
rmAb_MEM
M
A*01:01-specific IgVH sequences (n=4142)
+ A*01:01-specific rmAbs (n=50)
% of sequences
isotype
IgA
IgG
IgM
Unassigned

Figure 2

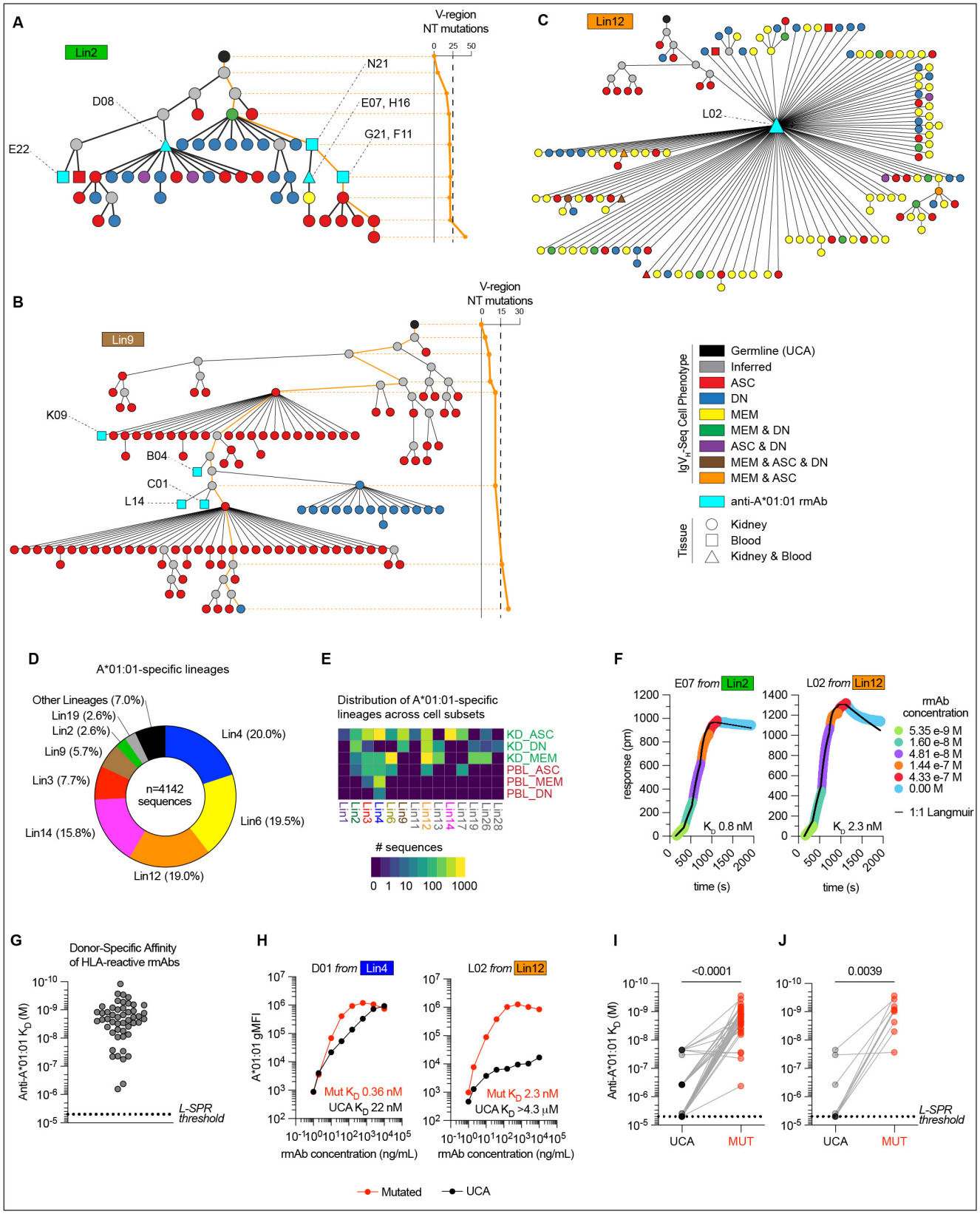
A
Lin2
V-region
NT mutations
0 25 50
N21
D08
E07, H16
G21, F11
E22
B
Lin9
V-region
NT mutations
0 15 30
K09
B04
C01
L14
C
Lin12
L02
Germline (UCA)
Inferred
ASC
DN
MEM
MEM & DN
ASC & DN
MEM & ASC & DN
MEM & ASC
IgV$_H$-Seq Cell Phenotype
anti-A*01:01 rmAb
Tissue
Kidney
Blood
Kidney & Blood
D
A*01:01-specific lineages
Other Lineages (7.0%)
Lin19 (2.6%)
Lin2 (2.6%)
Lin9 (5.7%)
Lin3 (7.7%)
Lin14 (15.8%)
Lin12 (19.0%)
Lin6 (19.5%)
Lin4 (20.0%)
n=4142
sequences
E
Distribution of A*01:01-specific
lineages across cell subsets
KD_ASC
KD_DN
KD_MEM
PBL_ASC
PBL_MEM
PBL_DN
Lin1 Lin2 Lin3 Lin4 Lin6 Lin9 Lin11 Lin12 Lin13 Lin14 Lin17 Lin19 Lin26 Lin28
sequences
0 1 10 100 1000
F
E07 from Lin2
L02 from Lin12
response (pm)
time (s)
K$_D$ 0.8 nM
K$_D$ 2.3 nM
rmAb
concentration
5.35 e-9 M
1.60 e-8 M
4.81 e-8 M
1.44 e-7 M
4.33 e-7 M
0.00 M
1:1 Langmuir
G
Donor-Specific Affinity
of HLA-reactive rmAbs
Anti-A*01:01 K$_D$ (M)
L-SPR
threshold
H
D01 from Lin4
L02 from Lin12
A*01:01 gMFI
Mut K$_D$ 0.36 nM
UCA K$_D$ 22 nM
Mut K$_D$ 2.3 nM
UCA K$_D$ >4.3 μM
rmAb concentration (ng/mL)
Mutated
UCA
I
<0.0001
Anti-A*01:01 K$_D$ (M)
UCA
MUT
J
0.0039
L-SPR
threshold
UCA
MUT

Figure 3

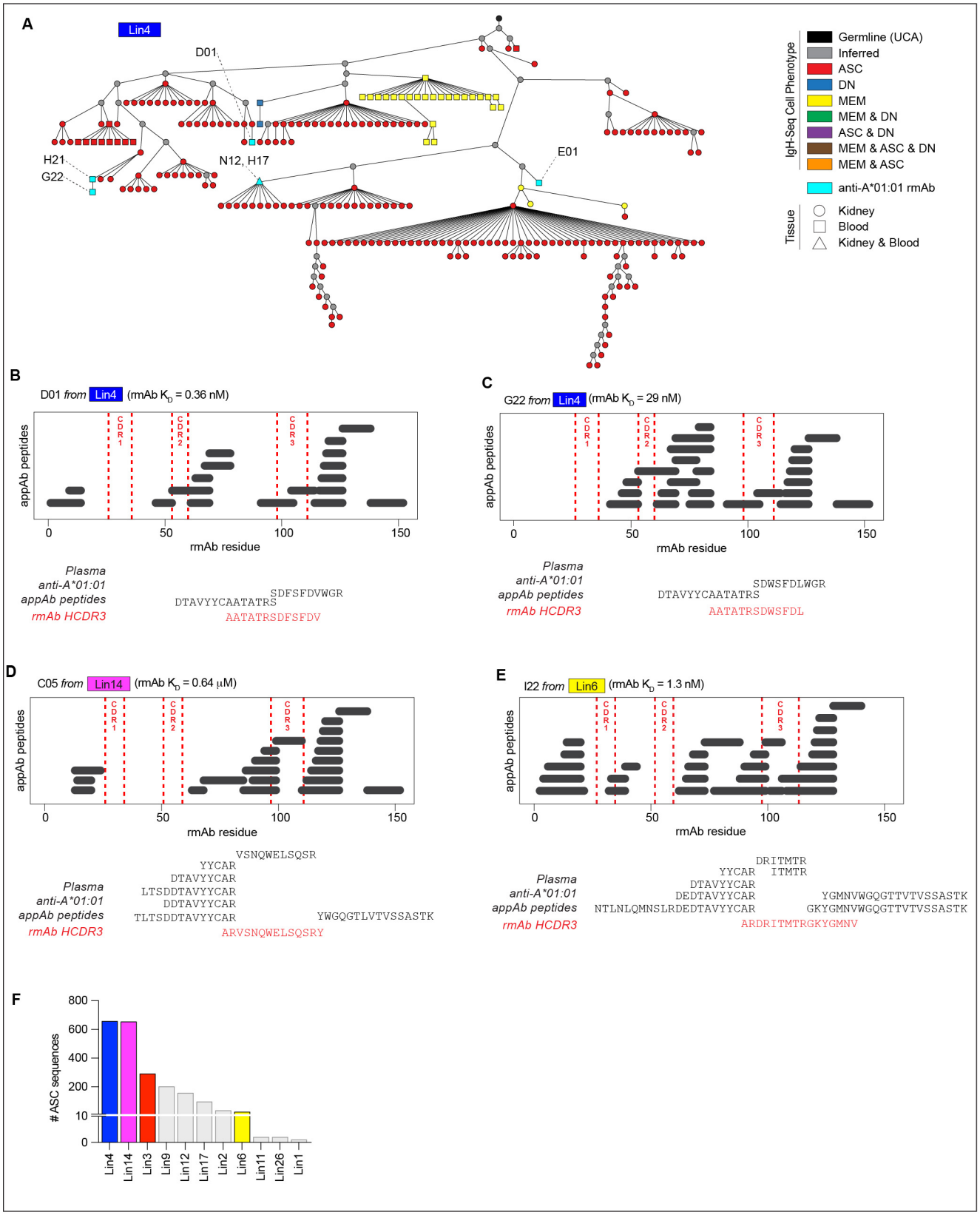
A
Lin4
D01
H21
G22
N12, H17
E01
IgH-Seq Cell Phenotype
Germline (UCA)
Inferred
ASC
DN
MEM
MEM & DN
ASC & DN
MEM & ASC & DN
MEM & ASC
anti-A*01:01 rmAb
Tissue
Kidney
Blood
Kidney & Blood
B
D01 from Lin4 (rmAb K_D = 0.36 nM)
appAb peptides
CDR1
CDR2
CDR3
rmAb residue
0
50
100
150
Plasma anti-A*01:01 appAb peptides
SDFSFDVWGR
DTAVYYCAATATRS
rmAb HCDR3
AATATRSDFSFDV
C
G22 from Lin4 (rmAb K_D = 29 nM)
appAb peptides
rmAb residue
Plasma anti-A*01:01 appAb peptides
SDWSFDLWGR
DTAVYYCAATATRS
rmAb HCDR3
AATATRSDWSFDL
D
C05 from Lin14 (rmAb K_D = 0.64 μM)
appAb peptides
rmAb residue
VSNQWELSQSR
YYCAR
DTAVYYCAR
LTSDDTAVYYCAR
DDTAVYYCAR
TLTSDDTAVYYCAR
YWGQGTLVTVSSASTK
Plasma anti-A*01:01 appAb peptides
rmAb HCDR3
ARVSNQWELSQSRY
E
I22 from Lin6 (rmAb K_D = 1.3 nM)
appAb peptides
rmAb residue
DRITMTR
YYCAR ITMTR
DTAVYYCAR
DEDTAVYYCAR
YGMNVWGQGTTVTVSSASTK
NTLNLQMNSLRDEDTAVYYCAR
GKYGMNVWGQGTTVTVSSASTK
Plasma anti-A*01:01 appAb peptides
rmAb HCDR3
ARDRITMTRGKYGMNV
F
ASC sequences
800
600
400
200
10
0
Lin4
Lin14
Lin3
Lin9
Lin12
Lin17
Lin2
Lin6
Lin11
Lin26
Lin1

Figure 4

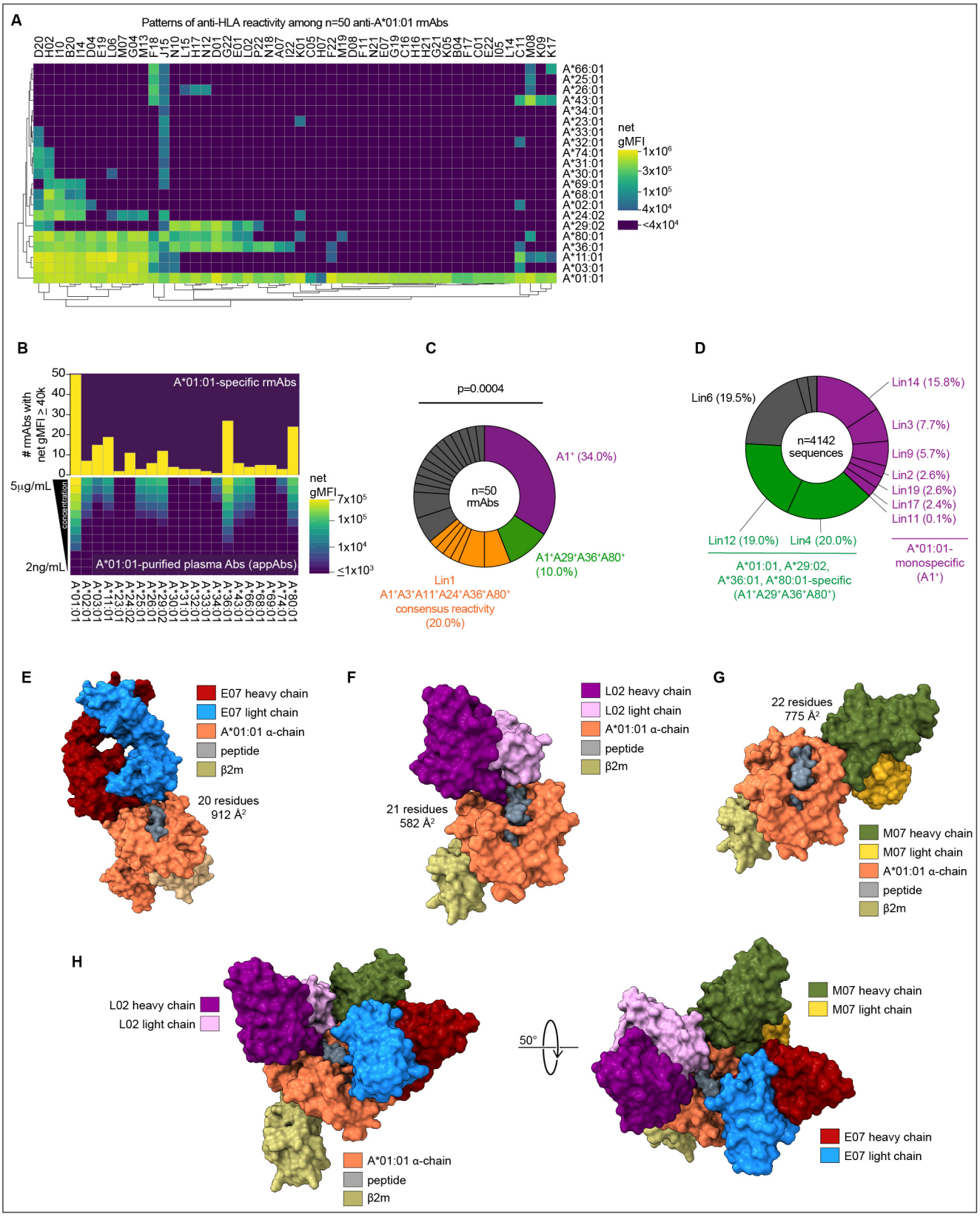
A
Patterns of anti-HLA reactivity among n=50 anti-A*01:01 rmAbs
D20 H02 I10 B20 I14 D04 E19 L06 M07 G04 M13 F18 J15 N10 L15 H17 N12 D01 G22 E01 D02 R22 N18 A07 I22 K01 C05 H07 F22 M19 D08 F11 N21 E07 G19 C16 H16 H21 G21 K05 B04 F17 C01 E22 I05 L14 C11 M08 K09 K17
A*66:01 A*25:01 A*26:01 A*43:01 A*34:01 A*23:01 A*33:01 A*32:01 A*74:01 A*31:01 A*30:01 A*69:01 A*68:01 A*02:01 A*24:02 A*29:02 A*80:01 A*36:01 A*11:01 A*03:01 A*01:01
net gMFI
1x10^6
3x10^5
1x10^5
4x10^4
<4x10^4
B
rmAbs with net gMFI ≥ 40k
A*01:01-specific rmAbs
5μg/mL
concentration
2ng/mL
A*01:01-purified plasma Abs (appAbs)
net gMFI
7x10^5
1x10^5
1x10^4
≤1x10^3
A*01:01 A*02:01 A*03:01 A*11:01 A*23:01 A*24:02 A*26:01 A*25:01 A*29:02 A*30:01 A*31:01 A*32:01 A*33:01 A*34:01 A*36:01 A*43:01 A*66:01 A*68:01 A*69:01 A*74:01 A*80:01
C
p=0.0004
n=50 rmAbs
A1+ (34.0%)
A1+A29+A36+A80+ (10.0%)
Lin1
A1+A3+A11+A24+A36+A80+ consensus reactivity (20.0%)
D
n=4142 sequences
Lin6 (19.5%)
Lin14 (15.8%)
Lin3 (7.7%)
Lin9 (5.7%)
Lin2 (2.6%)
Lin19 (2.6%)
Lin17 (2.4%)
Lin11 (0.1%)
Lin12 (19.0%)
Lin4 (20.0%)
A*01:01, A*29:02, A*36:01, A*80:01-specific (A1+A29+A36+A80+)
A*01:01-monospecific (A1+)
E
E07 heavy chain
E07 light chain
A*01:01 α-chain
peptide
β2m
20 residues 912 Å2
F
L02 heavy chain
L02 light chain
A*01:01 α-chain
peptide
β2m
21 residues 582 Å2
G
22 residues 775 Å2
M07 heavy chain
M07 light chain
A*01:01 α-chain
peptide
β2m
H
L02 heavy chain
L02 light chain
A*01:01 α-chain
peptide
β2m
50°
M07 heavy chain
M07 light chain
E07 heavy chain
E07 light chain

Figure 5

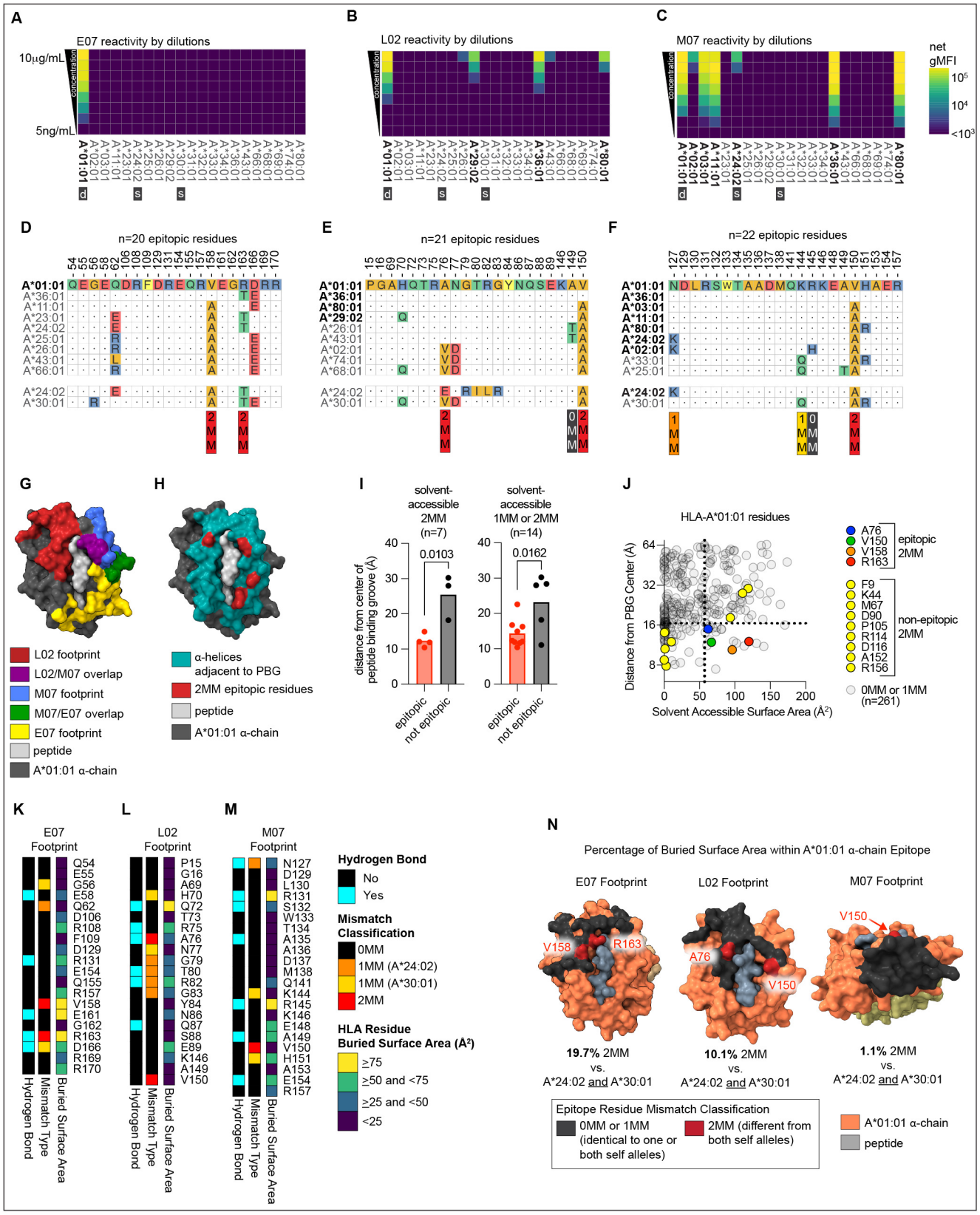
A
E07 reactivity by dilutions
10μg/mL
5ng/mL
concentration
B
L02 reactivity by dilutions
C
M07 reactivity by dilutions
net gMFI
D
n=20 epitopic residues
E
n=21 epitopic residues
F
n=22 epitopic residues
G
H
L02 footprint
L02/M07 overlap
M07 footprint
M07/E07 overlap
E07 footprint
peptide
A*01:01 α-chain
α-helices adjacent to PBG
2MM epitopic residues
I
solvent-accessible 2MM (n=7)
solvent-accessible 1MM or 2MM (n=14)
0.0103
0.0162
distance from center of peptide binding groove (Å)
epitopic
not epitopic
J
HLA-A*01:01 residues
Distance from PBG Center (Å)
Solvent Accessible Surface Area (Å²)
epitopic 2MM
non-epitopic 2MM
0MM or 1MM (n=261)
K
E07 Footprint
L
L02 Footprint
M
M07 Footprint
Hydrogen Bond
Mismatch Type
Buried Surface Area
Hydrogen Bond
No
Yes
Mismatch Classification
0MM
1MM (A*24:02)
1MM (A*30:01)
2MM
HLA Residue Buried Surface Area (Å²)
≥75
≥50 and <75
≥25 and <50
<25
N
Percentage of Buried Surface Area within A*01:01 α-chain Epitope
E07 Footprint
L02 Footprint
M07 Footprint
19.7% 2MM vs. A*24:02 and A*30:01
10.1% 2MM vs. A*24:02 and A*30:01
1.1% 2MM vs. A*24:02 and A*30:01
Epitope Residue Mismatch Classification
0MM or 1MM (identical to one or both self alleles)
2MM (different from both self alleles)
A*01:01 α-chain
peptide

Figure 6

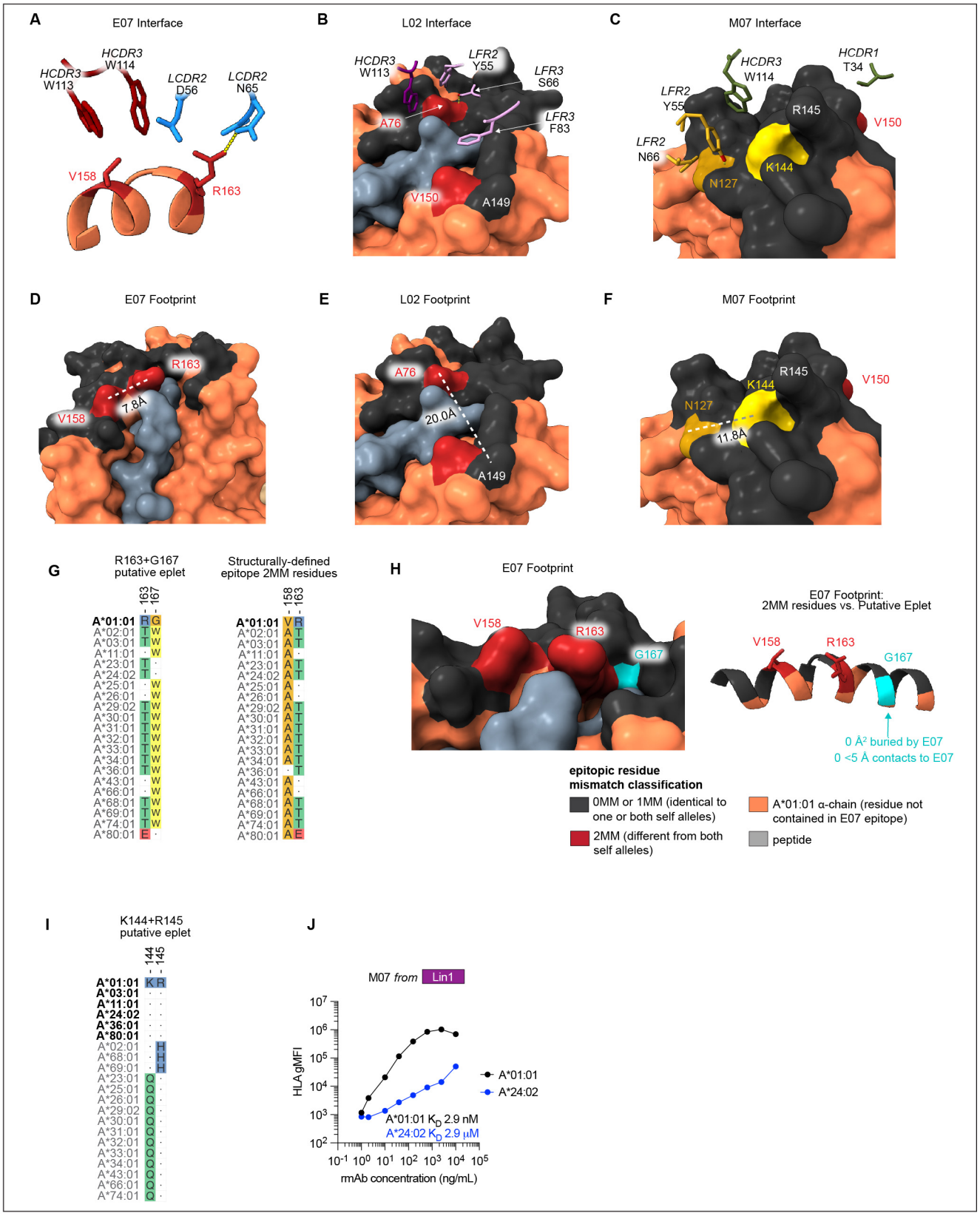
A
E07 Interface
HCDR3 W113
HCDR3 W114
LCDR2 D56
LCDR2 N65
V158
R163
B
L02 Interface
HCDR3 W113
LFR2 Y55
LFR3 S66
A76
LFR3 F83
V150
A149
C
M07 Interface
HCDR3 W114
HCDR1 T34
LFR2 Y55
R145
V150
LFR2 N66
K144
N127
D
E07 Footprint
R163
V158
7.8Å
E
L02 Footprint
A76
20.0Å
A149
F
M07 Footprint
R145
K144
V150
N127
11.8Å
G
R163+G167 putative eplet
Structurally-defined epitope 2MM residues
H
E07 Footprint
V158
R163
G167
E07 Footprint: 2MM residues vs. Putative Eplet
0 Å² buried by E07
0 <5 Å contacts to E07
epitopic residue mismatch classification
0MM or 1MM (identical to one or both self alleles)
2MM (different from both self alleles)
A*01:01 α-chain (residue not contained in E07 epitope)
peptide
I
K144+R145 putative eplet
J
M07 from Lin1
HLA gMFI
A*01:01
A*24:02
A*01:01 K_D 2.9 nM
A*24:02 K_D 2.9 μM
rmAb concentration (ng/mL)

Figure 7

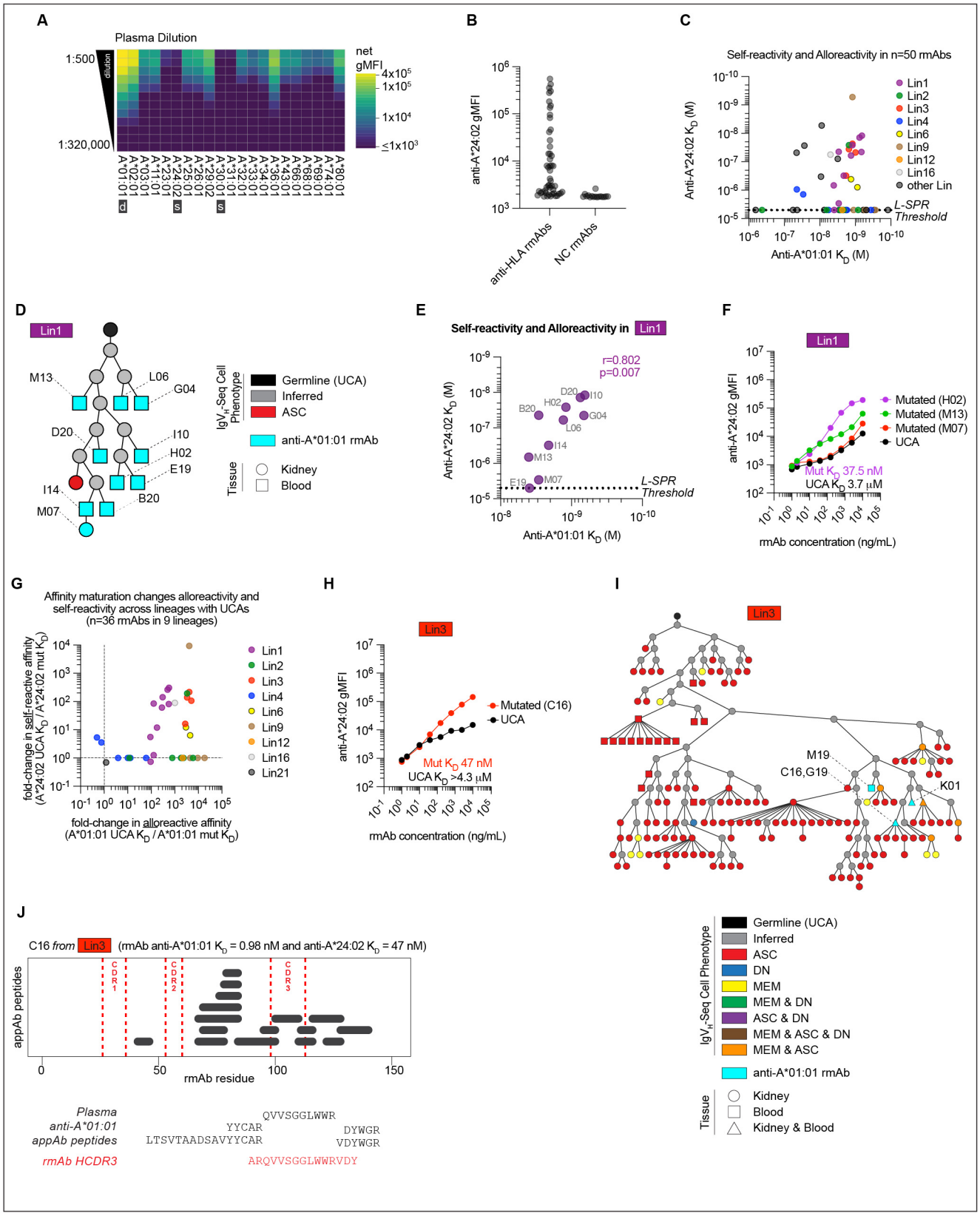
A
Plasma Dilution
1:500
1:320,000
dilution
net gMFI
4x10^5
1x10^5
1x10^4
≤1x10^3
A*01:01
A*02:01
A*03:01
A*11:01
A*23:01
A*24:02
A*25:01
A*26:01
A*29:02
A*30:01
A*31:01
A*32:01
A*33:01
A*34:01
A*36:01
A*43:01
A*66:01
A*68:01
A*69:01
A*74:01
A*80:01
d
s
s
B
anti-A*24:02 gMFI
anti-HLA rmAbs
NC rmAbs
C
Self-reactivity and Alloreactivity in n=50 rmAbs
Anti-A*24:02 K_D (M)
Anti-A*01:01 K_D (M)
Lin1
Lin2
Lin3
Lin4
Lin6
Lin9
Lin12
Lin16
other Lin
L-SPR Threshold
D
Lin1
M13
L06
G04
D20
I10
H02
E19
I14
B20
M07
IgV_H-Seq Cell Phenotype
Germline (UCA)
Inferred
ASC
anti-A*01:01 rmAb
Tissue
Kidney
Blood
E
Self-reactivity and Alloreactivity in Lin1
r=0.802
p=0.007
D20
I10
B20
H02
G04
L06
I14
M13
E19
M07
L-SPR Threshold
Anti-A*24:02 K_D (M)
Anti-A*01:01 K_D (M)
F
Lin1
anti-A*24:02 gMFI
Mutated (H02)
Mutated (M13)
Mutated (M07)
UCA
Mut K_D 37.5 nM
UCA K_D 3.7 μM
rmAb concentration (ng/mL)
G
Affinity maturation changes alloreactivity and self-reactivity across lineages with UCAs
(n=36 rmAbs in 9 lineages)
fold-change in self-reactive affinity (A*24:02 UCA K_D / A*24:02 mut K_D)
fold-change in alloreactive affinity (A*01:01 UCA K_D / A*01:01 mut K_D)
Lin1
Lin2
Lin3
Lin4
Lin6
Lin9
Lin12
Lin16
Lin21
H
Lin3
anti-A*24:02 gMFI
Mutated (C16)
UCA
Mut K_D 47 nM
UCA K_D >4.3 μM
rmAb concentration (ng/mL)
I
Lin3
M19
C16,G19
K01
J
C16 from Lin3 (rmAb anti-A*01:01 K_D = 0.98 nM and anti-A*24:02 K_D = 47 nM)
appAb peptides
CDR1
CDR2
CDR3
rmAb residue
Plasma
anti-A*01:01
appAb peptides
QVVSGGLWWR
YYCAR
DYWGR
LTSVTAADSAVYYCAR
VDYWGR
rmAb HCDR3
ARQVVSGGLWWRVDY
IgV_H-Seq Cell Phenotype
Germline (UCA)
Inferred
ASC
DN
MEM
MEM & DN
ASC & DN
MEM & ASC & DN
MEM & ASC
anti-A*01:01 rmAb
Tissue
Kidney
Blood
Kidney & Blood

Figure S1

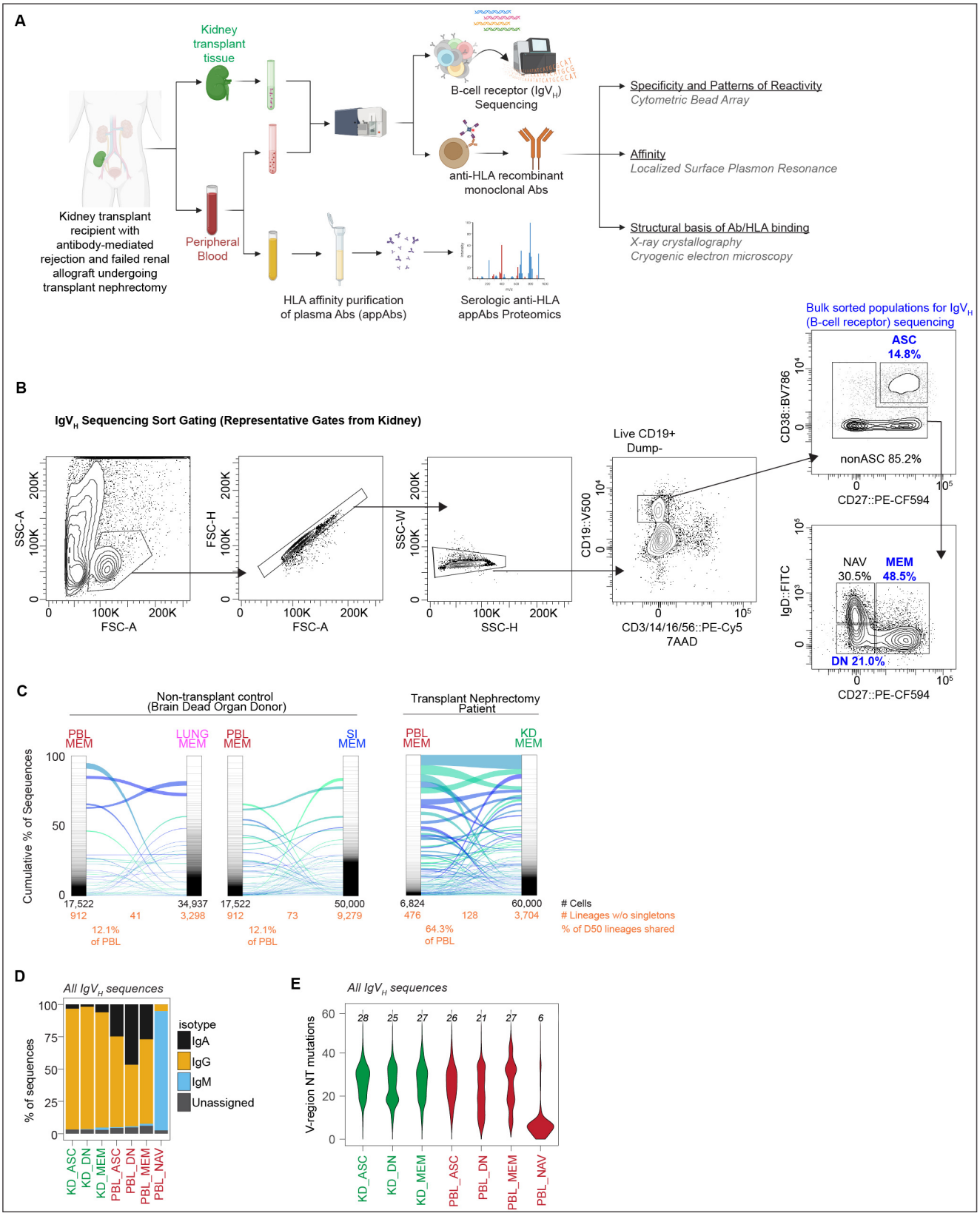
A
Kidney transplant tissue
Kidney transplant recipient with antibody-mediated rejection and failed renal allograft undergoing transplant nephrectomy
Peripheral Blood
B-cell receptor (IgV$_H$) Sequencing
anti-HLA recombinant monoclonal Abs
HLA affinity purification of plasma Abs (appAbs)
Serologic anti-HLA appAbs Proteomics
Specificity and Patterns of Reactivity
Cytometric Bead Array
Affinity
Localized Surface Plasmon Resonance
Structural basis of Ab/HLA binding
X-ray crystallography
Cryogenic electron microscopy
B
IgV$_H$ Sequencing Sort Gating (Representative Gates from Kidney)
SSC-A
FSC-A
FSC-H
SSC-W
SSC-H
Live CD19+ Dump-
CD19::V500
CD3/14/16/56::PE-Cy5 7AAD
Bulk sorted populations for IgV$_H$ (B-cell receptor) sequencing
CD38::BV786
ASC 14.8%
nonASC 85.2%
CD27::PE-CF594
IgD::FITC
NAV 30.5%
MEM 48.5%
DN 21.0%
C
Non-transplant control (Brain Dead Organ Donor)
Transplant Nephrectomy Patient
PBL MEM
LUNG MEM
SI MEM
KD MEM
Cumulative % of Seqeuences
17,522
34,937
912
41
3,298
12.1% of PBL
50,000
9,279
73
6,824
60,000
476
128
3,704
64.3% of PBL
Cells
Lineages w/o singletons
% of D50 lineages shared
D
All IgV$_H$ sequences
% of sequences
isotype
IgA
IgG
IgM
Unassigned
KD_ASC
KD_DN
KD_MEM
PBL_ASC
PBL_DN
PBL_MEM
PBL_NAV
E
All IgV$_H$ sequences
V-region NT mutations
28
25
27
26
21
27
6

Figure S2

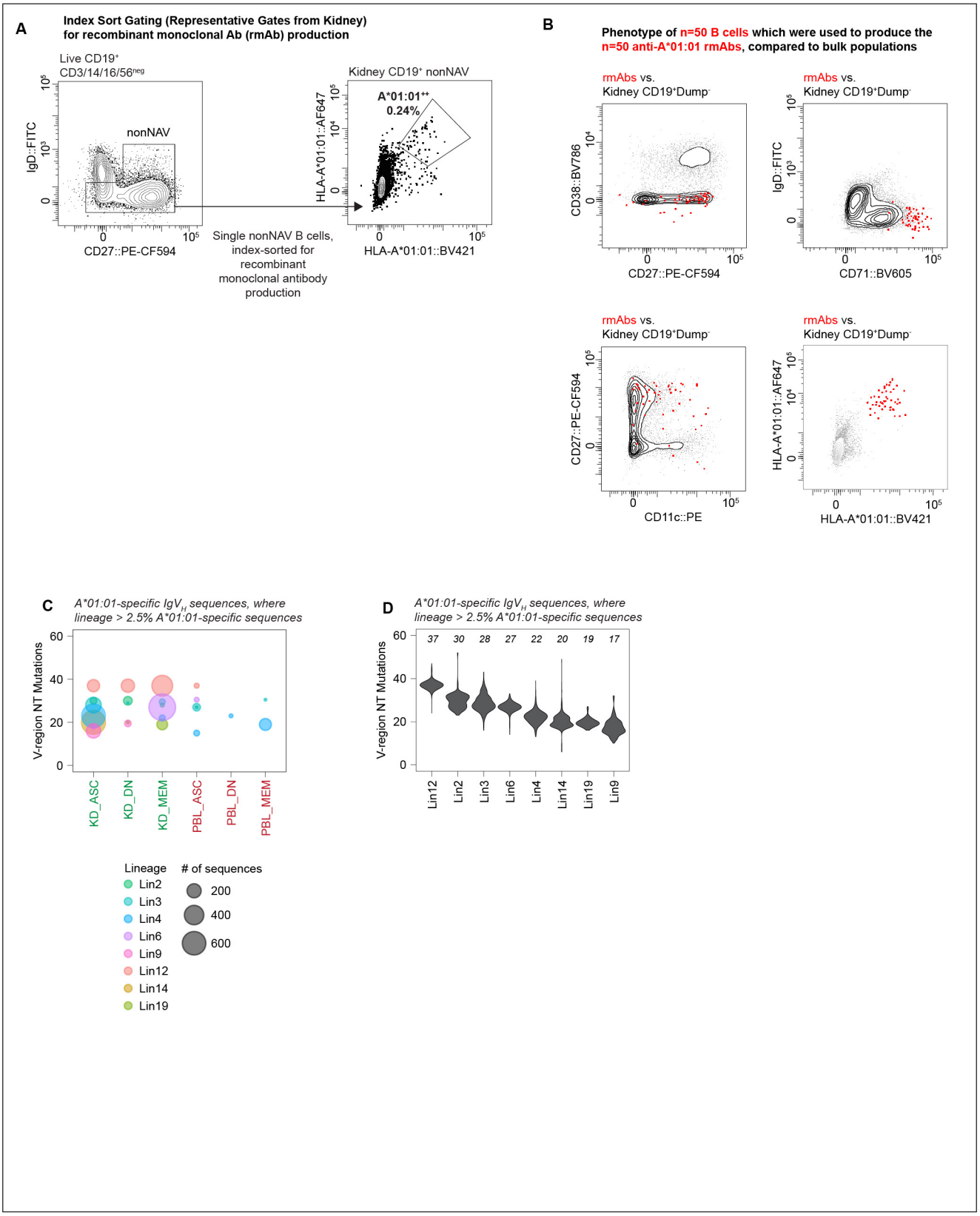
A
Index Sort Gating (Representative Gates from Kidney) for recombinant monoclonal Ab (rmAb) production
Live CD19+ CD3/14/16/56neg
nonNAV
IgD::FITC
CD27::PE-CF594
Kidney CD19+ nonNAV
A*01:01++ 0.24%
HLA-A*01:01::AF647
HLA-A*01:01::BV421
Single nonNAV B cells, index-sorted for recombinant monoclonal antibody production
B
Phenotype of n=50 B cells which were used to produce the n=50 anti-A*01:01 rmAbs, compared to bulk populations
rmAbs vs. Kidney CD19+Dump-
CD38::BV786
CD27::PE-CF594
IgD::FITC
CD71::BV605
CD27::PE-CF594
CD11c::PE
HLA-A*01:01::AF647
HLA-A*01:01::BV421
C
A*01:01-specific IgVH sequences, where lineage > 2.5% A*01:01-specific sequences
V-region NT Mutations
KD_ASC
KD_DN
KD_MEM
PBL_ASC
PBL_DN
PBL_MEM
Lineage
Lin2
Lin3
Lin4
Lin6
Lin9
Lin12
Lin14
Lin19
# of sequences
200
400
600
D
A*01:01-specific IgVH sequences, where lineage > 2.5% A*01:01-specific sequences
37 30 28 27 22 20 19 17
V-region NT Mutations
Lin12
Lin2
Lin3
Lin6
Lin4
Lin14
Lin19
Lin9

Figure S3

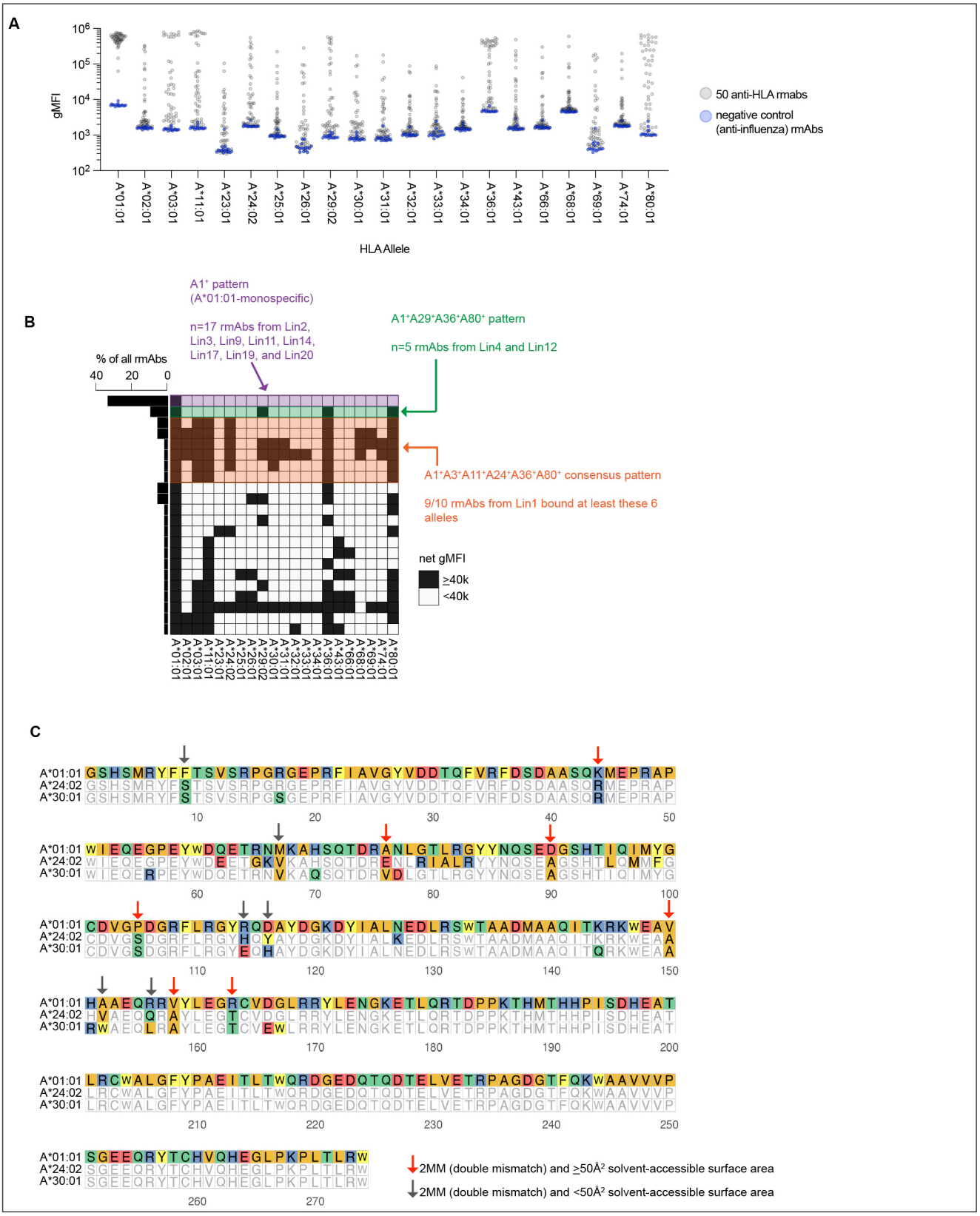
A
gMFI
HLA Allele
50 anti-HLA rmabs
negative control (anti-influenza) rmAbs
B
A1⁺ pattern (A*01:01-monospecific)
n=17 rmAbs from Lin2, Lin3, Lin9, Lin11, Lin14, Lin17, Lin19, and Lin20
A1⁺A29⁺A36⁺A80⁺ pattern
n=5 rmAbs from Lin4 and Lin12
% of all rmAbs
A1⁺A3⁺A11⁺A24⁺A36⁺A80⁺ consensus pattern
9/10 rmAbs from Lin1 bound at least these 6 alleles
net gMFI
≥40k
<40k
C
A*01:01
A*24:02
A*30:01
2MM (double mismatch) and ≥50Å² solvent-accessible surface area
2MM (double mismatch) and <50Å² solvent-accessible surface area

Figure S4

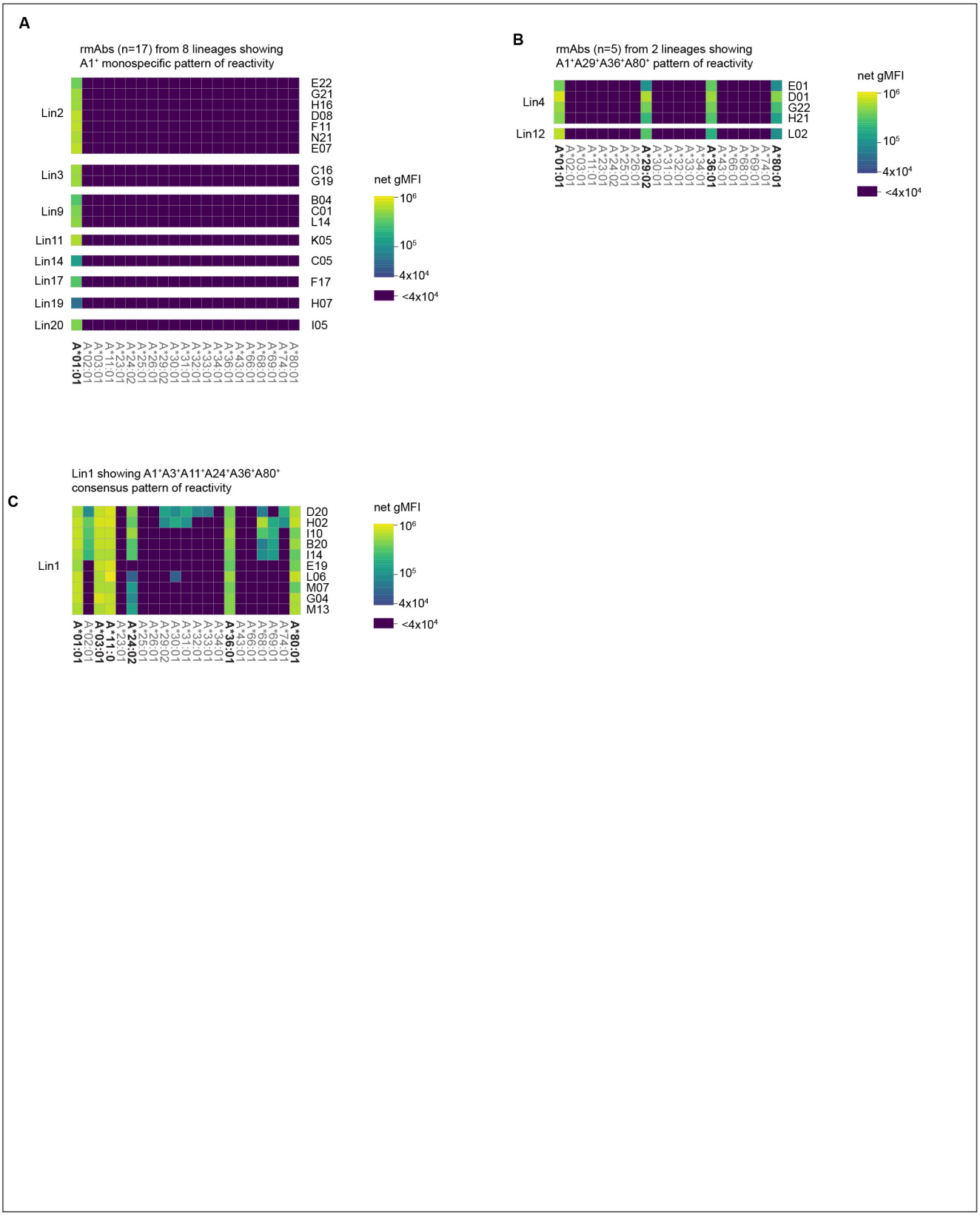
A
rmAbs (n=17) from 8 lineages showing
A1+ monospecific pattern of reactivity
Lin2
Lin3
Lin9
Lin11
Lin14
Lin17
Lin19
Lin20
E22
G21
H16
D08
F11
N21
E07
C16
G19
B04
C01
L14
K05
C05
F17
H07
I05
A*01:01
A*02:01
A*03:01
A*11:01
A*23:01
A*24:02
A*25:01
A*26:01
A*29:02
A*30:01
A*31:01
A*32:01
A*33:01
A*34:01
A*36:01
A*43:01
A*66:01
A*68:01
A*69:01
A*74:01
A*80:01
net gMFI
10^6
10^5
4x10^4
<4x10^4
B
rmAbs (n=5) from 2 lineages showing
A1+A29+A36+A80+ pattern of reactivity
Lin4
Lin12
E01
D01
G22
H21
L02
A*01:01
A*02:01
A*03:01
A*11:01
A*23:01
A*24:02
A*25:01
A*26:01
A*29:02
A*30:01
A*31:01
A*32:01
A*33:01
A*34:01
A*36:01
A*43:01
A*66:01
A*68:01
A*69:01
A*74:01
A*80:01
net gMFI
10^6
10^5
4x10^4
<4x10^4
C
Lin1 showing A1+A3+A11+A24+A36+A80+
consensus pattern of reactivity
Lin1
D20
H02
I10
B20
I14
E19
L06
M07
G04
M13
A*01:01
A*02:01
A*03:01
A*11:0
A*23:01
A*24:02
A*25:01
A*26:01
A*29:02
A*30:01
A*31:01
A*32:01
A*33:01
A*34:01
A*36:01
A*43:01
A*66:01
A*68:01
A*69:01
A*74:01
A*80:01
net gMFI
10^6
10^5
4x10^4
<4x10^4

Figure S5

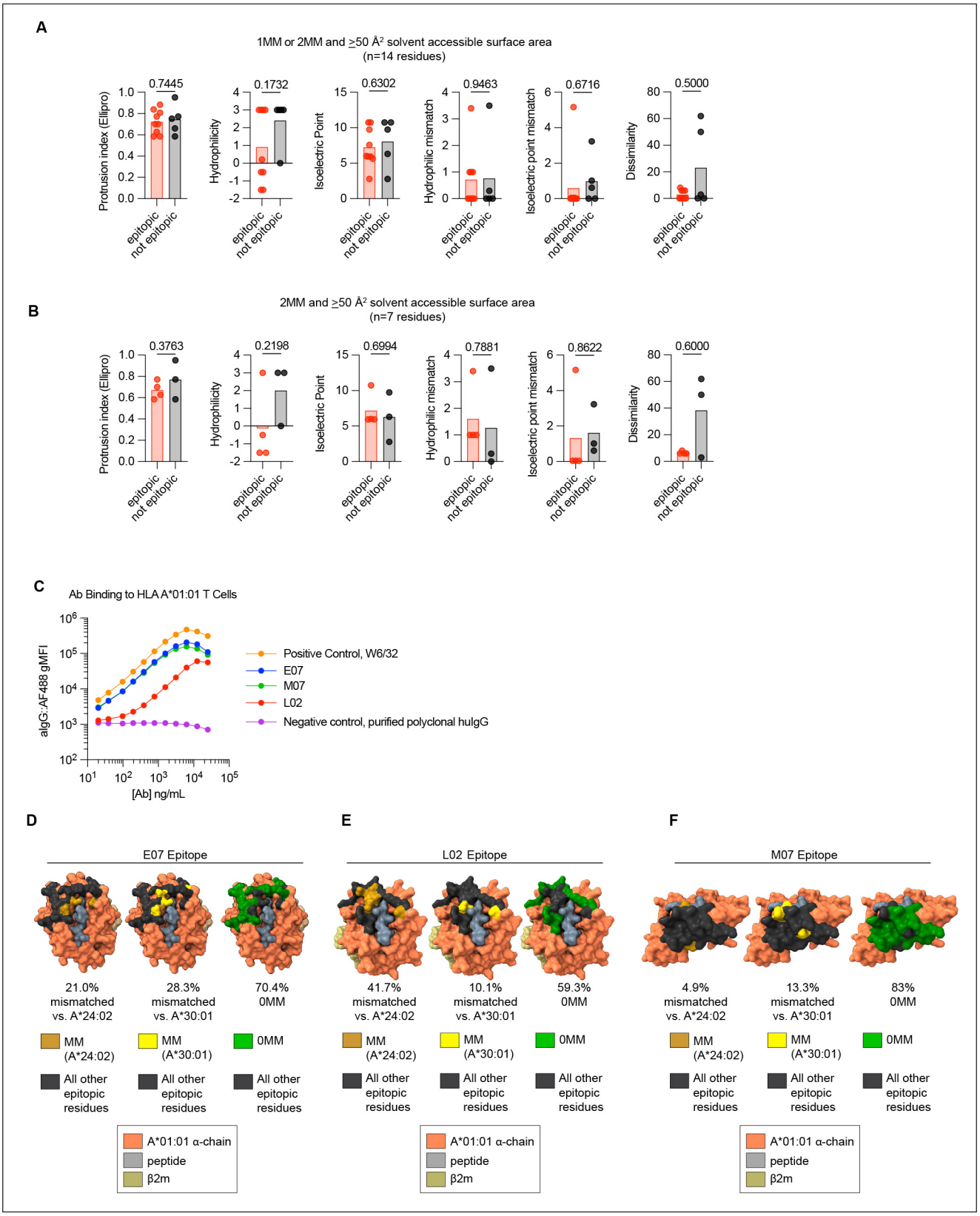
A
1MM or 2MM and ≥50 Å² solvent accessible surface area
(n=14 residues)
Protrusion index (Ellipro)
0.7445
Hydrophilicity
0.1732
Isoelectric Point
0.6302
Hydrophilic mismatch
0.9463
Isoelectric point mismatch
0.6716
Dissimilarity
0.5000
epitopic
not epitopic
B
2MM and ≥50 Å² solvent accessible surface area
(n=7 residues)
0.3763
0.2198
0.6994
0.7881
0.8622
0.6000
C
Ab Binding to HLA A*01:01 T Cells
algG::AF488 gMFI
[Ab] ng/mL
Positive Control, W6/32
E07
M07
L02
Negative control, purified polyclonal hulgG
D
E07 Epitope
21.0% mismatched vs. A*24:02
28.3% mismatched vs. A*30:01
70.4% 0MM
E
L02 Epitope
41.7% mismatched vs. A*24:02
10.1% mismatched vs. A*30:01
59.3% 0MM
F
M07 Epitope
4.9% mismatched vs. A*24:02
13.3% mismatched vs. A*30:01
83% 0MM
MM (A*24:02)
MM (A*30:01)
0MM
All other epitopic residues
A*01:01 α-chain
peptide
β2m

Figure S6

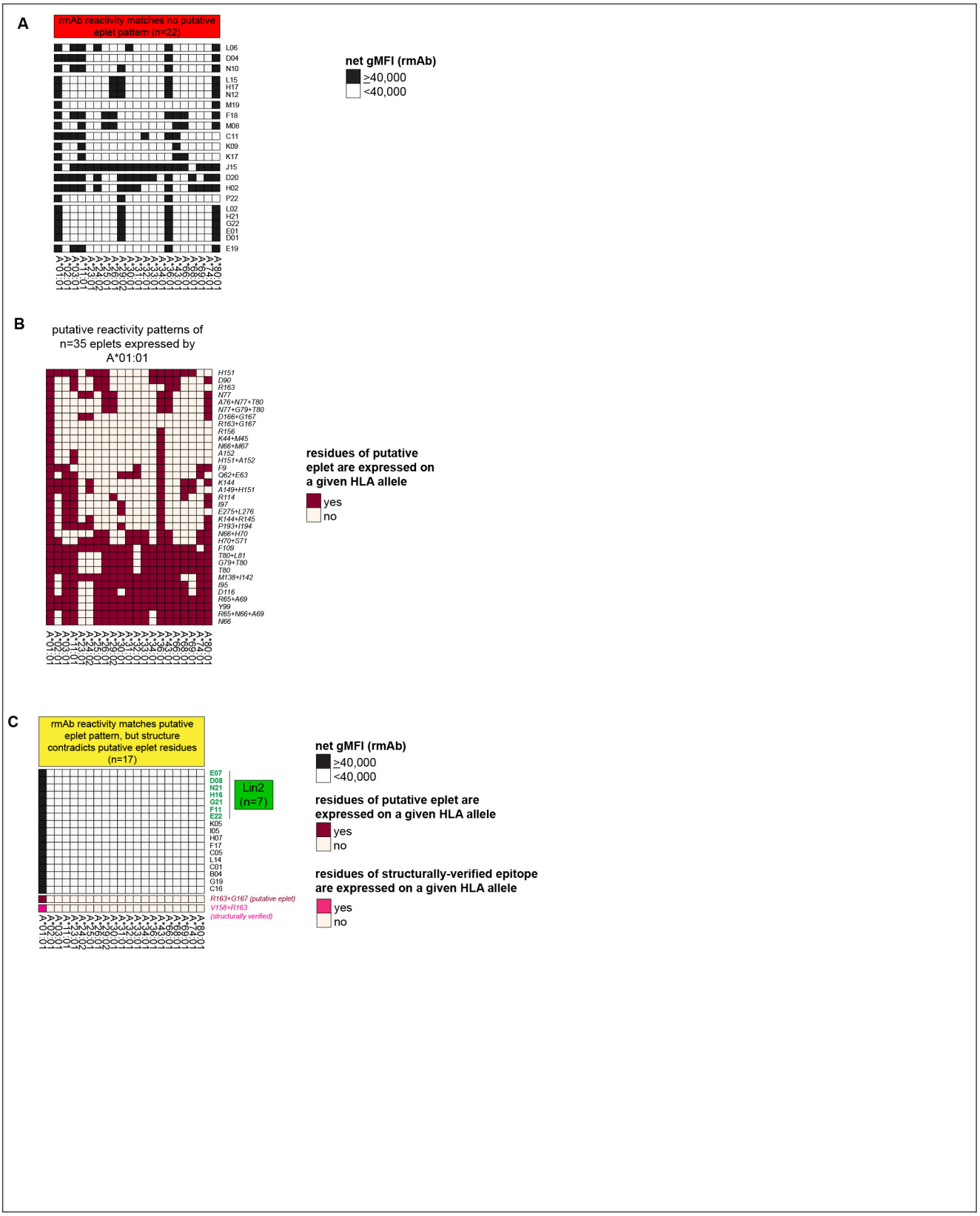
A
rmAb reactivity matches no putative eplet pattern (n=22)
L06
D04
N10
L15
H17
N12
M19
F18
M08
C11
K09
K17
J15
D20
H02
P22
L02
H21
G22
E01
D01
E19
A*01:01
A*02:01
A*03:01
A*11:01
A*23:01
A*24:02
A*25:01
A*26:01
A*29:02
A*30:01
A*31:01
A*32:01
A*33:01
A*34:01
A*36:01
A*43:01
A*66:01
A*68:01
A*69:01
A*74:01
A*80:01
net gMFI (rmAb)
≥40,000
<40,000
B
putative reactivity patterns of n=35 eplets expressed by A*01:01
H151
D90
R163
N77
A76+N77+T80
N77+G79+T80
D166+G167
R163+G167
R156
K44+M45
N66+M67
A152
H151+A152
F9
Q62+E63
K144
A149+H151
R114
I97
E275+L276
K144+R145
P193+I194
N66+H70
H70+S71
F109
T80+L81
G79+T80
T80
M138+I142
I95
D116
R65+A69
Y99
R65+N66+A69
N66
residues of putative eplet are expressed on a given HLA allele
yes
no
C
rmAb reactivity matches putative eplet pattern, but structure contradicts putative eplet residues (n=17)
E07
D08
N21
H16
G21
F11
E22
Lin2 (n=7)
K05
I05
H07
F17
C05
L14
C01
B04
G19
C16
R163+G167 (putative eplet)
V158+R163 (structurally verified)
net gMFI (rmAb)
≥40,000
<40,000
residues of putative eplet are expressed on a given HLA allele
yes
no
residues of structurally-verified epitope are expressed on a given HLA allele
yes
no

Figure S7

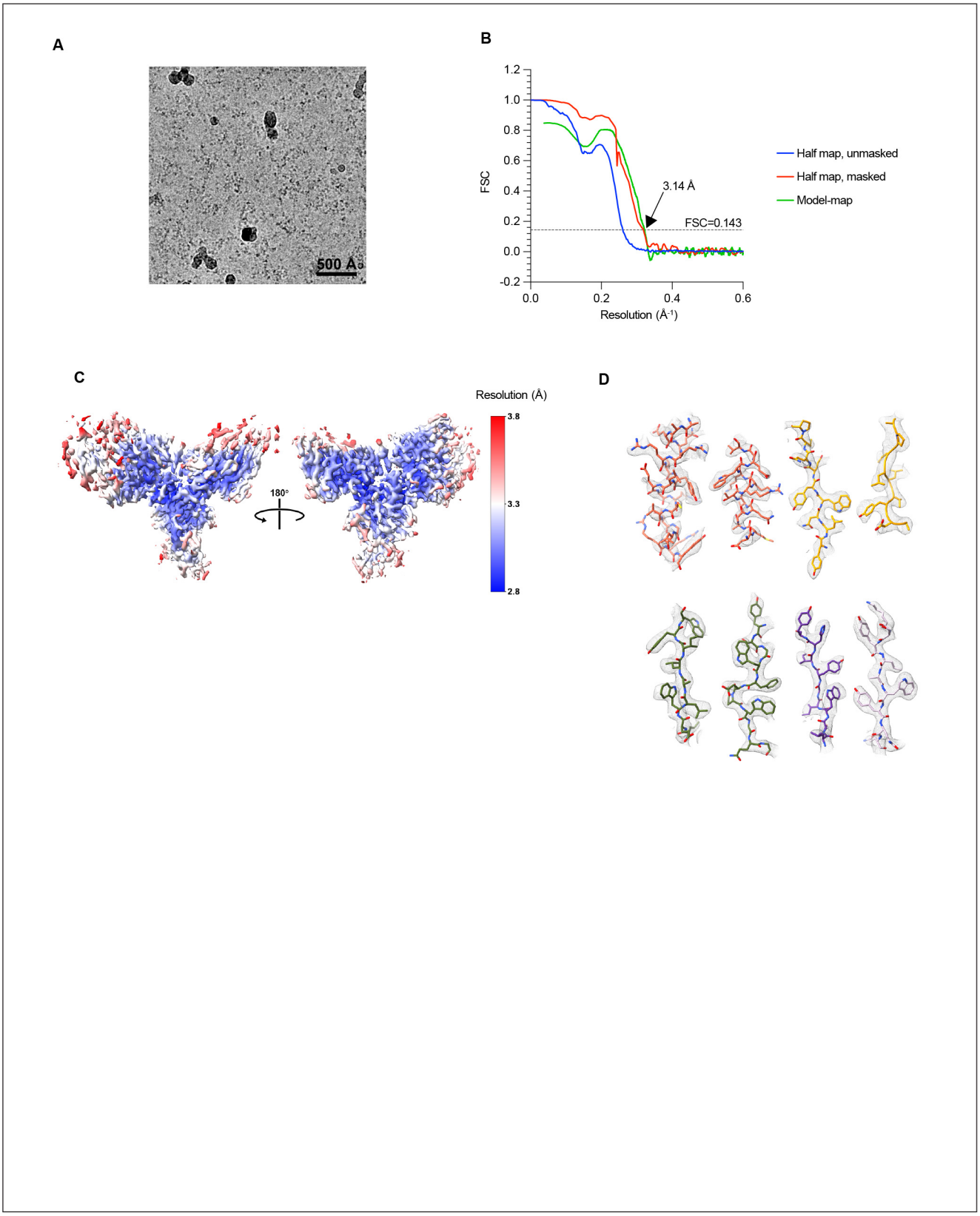
A
500 Å
B
FSC
Resolution (Å⁻¹)
3.14 Å
FSC=0.143
Half map, unmasked
Half map, masked
Model-map
C
Resolution (Å)
3.8
3.3
2.8
180°
D